NOTICE: When government or other drawings, specifications or other data are used for any purpose other than in connection with a definitely related government procurement operation, the U. S. Cover ent thereby incurs no responsibility, nor any ol gation whatsoever; and the fact that the Govern- may have formulated, furnished, or in any way plied the said drawings, specifications, or other a is not to be regarded by implication or otherwise as in any manner licensing the holder or any other person or corporation, or conveying any rights or permission to manufacture, use or sell any patented invention that may in any way be related thereto.

ARPA ORDER NO. 347-62
PROJECT CODE NO. 7400

GENERAL MOTORS CORPORATION

REPORT ON

INSTRUMENTATION, CALIBRATION, AND DATA REDUCTION METHODS

CONTRACT NO. DA-04-495-ORD-3567
HYPERVELOCITY RANGE RESEARCH PROGRAM

DEFENSE RESEARCH LABORATORIES
SANTA BARBARA, CALIFORNIA

AEROSPACE OPERATIONS DEPARTMENT

TR62-213

DECEMBER 1962

ARPA ORDER NO. 347-62
PROJECT CODE NO. 7400

Copy No 28

GENERAL MOTORS CORPORATION

REPORT ON

INSTRUMENTATION, CALIBRATION, AND DATA REDUCTION METHODS

COMPILED BY W. L. KOCH

CONTRACT NO. DA-04-495-ORD-3567
HYPERVELOCITY RANGE RESEARCH PROGRAM

DEFENSE RESEARCH LABORATORIES
SANTA BARBARA, CALIFORNIA

AEROSPACE OPERATIONS DEPARTMENT

TR62-213

DECEMBER 1962

FOREWORD

This Instrumentation Report has been prepared with several purposes in mind. First, a thorough description of the Flight Physics Range instrumentation is necessary because the majority of data are in the form of photographic records made with spark illumination of the model or taken directly from oscilloscope traces. Thus, in order to interpret these photographic records, a thorough understanding of the apparatus is required. The second purpose is to establish a basis for the reduction of raw photographic data as presented in our data reports, Volumes I – VI. This reduction requires a presentation of mathematical methods as well as the constants needed for the computations. Finally, calibration methods of the various instruments and of the entire flight trajectory need to be presented in order to establish the accuracy and reliability of the data.

For these reasons, this report should be considered a handbook, covering such fields as flight kinematics, optical radiation, microwave phase shift and attenuation, and doppler radar return. It is written as a series of descriptions by investigators who are experts in their respective fields.

It is hoped that the material presented in this report will prove a valuable tool in reducing specific data from the accompanying reports.*

---

* This research is part of Project DEFENDER, sponsored by the Advanced Research Projects Agency, Department of Defense.

TABLE OF CONTENTS

TABLE OF CONTENTS (cont)

LIST OF ILLUSTRATIONS

LIST OF ILLUSTRATIONS (cont)

LIST OF ILLUSTRATIONS (cont)

LIST OF ILLUSTRATIONS (cont)

LIST OF ILLUSTRATIONS (cont)

SECTION I
INTRODUCTION

The Physics Range at General Motors Defense Research Laboratories is an advanced facility for supporting research in the physics of hypervelocity flight. This facility is capable of simulating to a high degree the actual flight conditions associated with ICBM and space vehicles under controlled laboratory test conditions. Since observations are made of models in free flight, real phenomena can be studied without interference effects or uncertainties concerning flow conditions.

The principal parts of the range are the hypervelocity launcher (a light-gas gun), the flight test chamber, and the radar chamber. The test model is fired by the gun into the flight test and radar chambers where observations are made while the model is in free flight. The pressure of the gas in the chambers can be varied so that flight at various altitudes can be simulated. In addition, the composition of the gas can be controlled so that flight through gases other than air can be studied.

A schematic drawing of the Flight Physics Range is presented in Fig. 1-1. The flight test chamber is a tube 0.61 meter in diameter and 10.4 meters long, segmented to provide flexibility in the positioning of the instrumentation stations along the flight path. The individual sections are evident in Figs. 1-2 and 1-3 which show the arrangement of range instrumentation along the flight chamber during the period of this report.

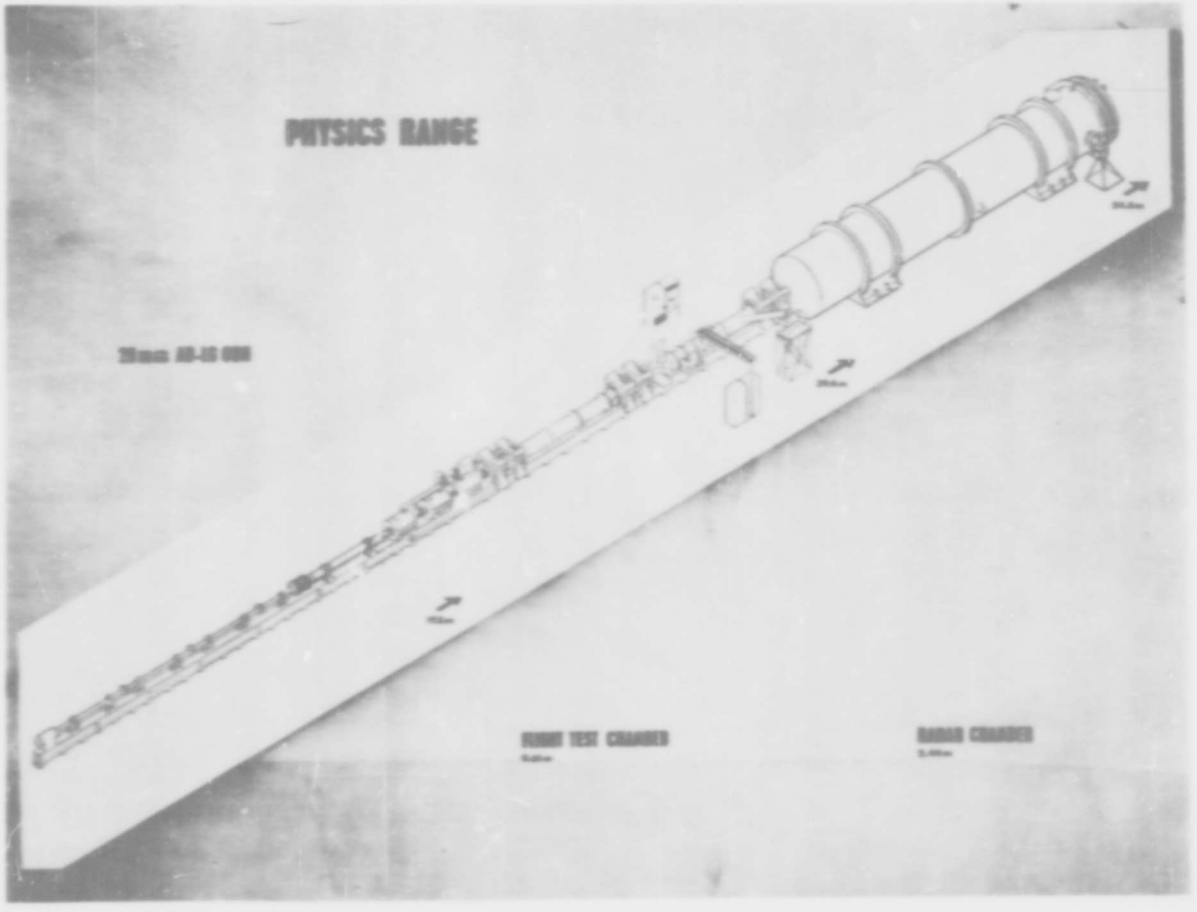

Fig. 1-1 Schematic, Physics Range

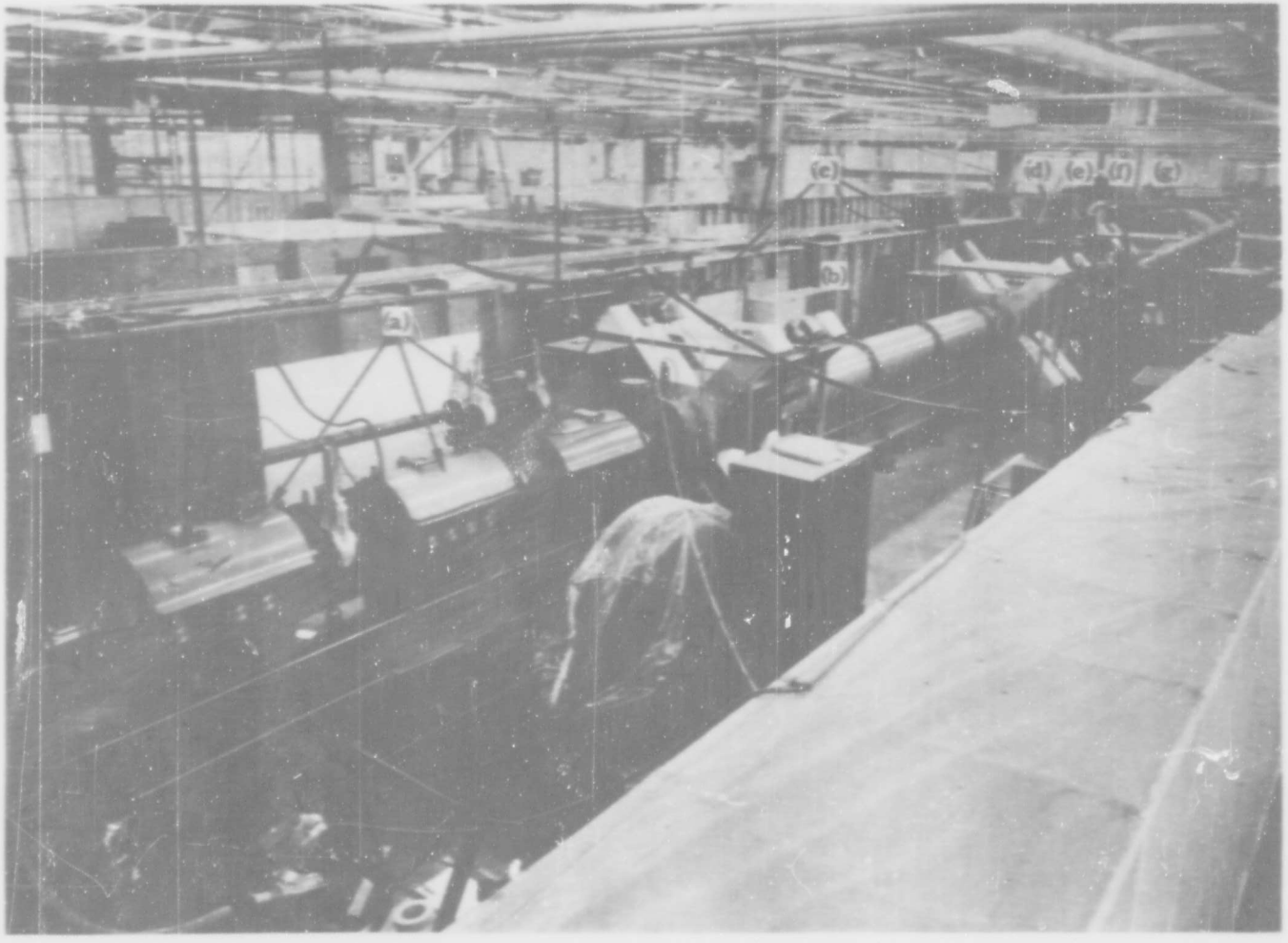

Fig. 1-2 View of Physics Range at Launcher End

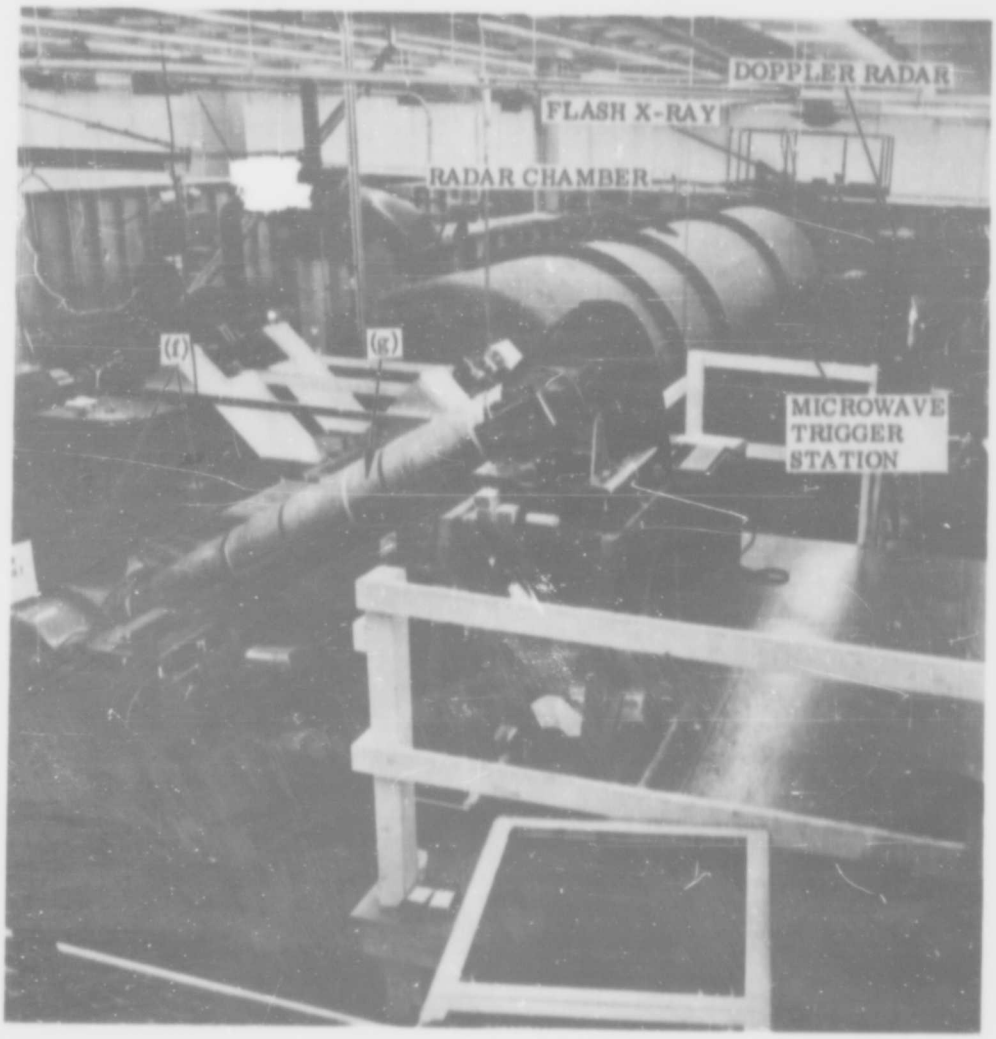

Fig. 1-3 View of Physics Range at Radar Chamber

The radar chamber (Fig. 1-3) is a tank 2.44 meters in diameter and 15.2 meters long. The tank was designed for use with the head-on doppler radar, and the interior of the tank is free of obstruction to prevent spurious reflection.

The muzzle of the light-gas-gun launcher is shown at the left of Fig. 1-2. It fires the model from left to right through the range. The blast tanks allow expansion of the gun gases and lessen their contamination potential in the free-flight section of the range.

A discussion of the light-gas-gun launcher (Fig. 1-4) is included in a later section of this report.

To protect some of the models from contact with the launch tube during the firing sequence, they are completely supported in a sabot. The sabot fits the bore of the gun and is formed from several pieces which must separate from the model before physical measurements can be made of the model in flight. The separation process has been accomplished aerodynamically in the tests to date (December 1962). Since separation forces are small, a distance of approximately 10.6 meters is covered before the sabot sections spread over a radial distance sufficient to permit interception in a sabot separation chamber. The sabot pieces impact around a tube through which the model passes on the range axis. Further discussion of the saboting technique will be presented in a subsequent section of this report.

The free-flight instrumentation sections are indicated in Figs. 1-2 and 1-3. Shown are: (a) blast chambers, (b) flight-test chambers, (c) spark photography stations to record the model integrity, flight attitude and position at a given time during the model's flight, (d) the

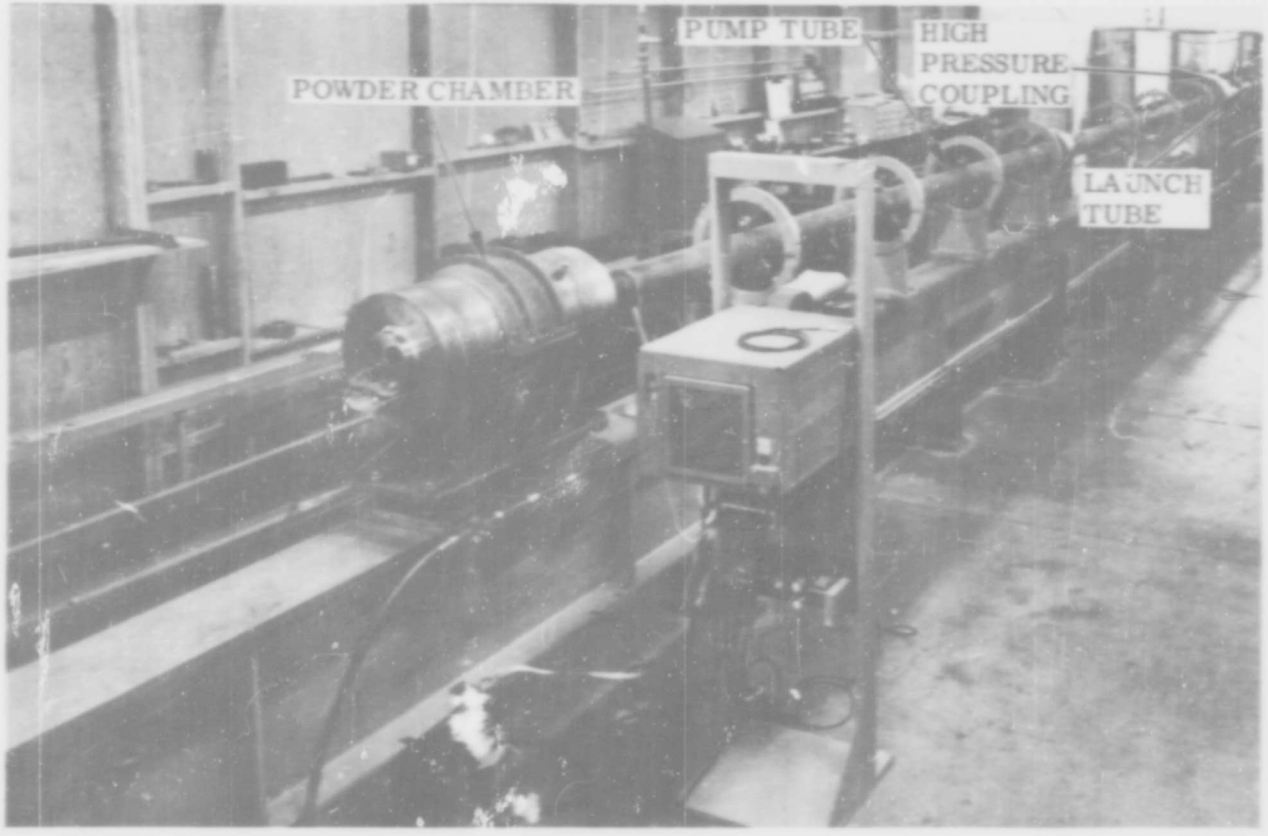

Fig. 1-4 Light-Gas-Gun Launcher, Physics Range

transverse microwave probes for detailed records of the ionization in the flow field around the model and in its wake, (e) an infrared radiation detection station, (f) an ultraviolet infrared (visible) radiation detection station, and (g) a spark schlieren station for recording photographically the flow field around the model and in the wake.

Indicated on Fig. 1-3 are: a microwave trigger station for the timing of doppler radar measurements, a flash X-ray station to provide final information on model integrity, flight attitude and position with time, and the doppler radar station. This instrumentation will be discussed in detail in subsequent sections of this report.

The pumps for evacuating the flight test and radar chambers consist of two roughing pumps and an oil diffusion booster pump which can evacuate the chambers to an equivalent pressure altitude of 350,000 ft. The high-capacity pumps can evacuate the tank to a pressure of 1 micron of mercury in about 1 hour. The seals around doors, ports, and other openings are hermetically tight, and the leak-rate of the system is on the order of 0.1 micron of mercury (increase in pressure) per minute at pressures of the order of a few microns.

The development of new techniques for range operation is in progress, and changes in gas valving, instrumentation placement and operational procedures may be made from time to time; consequently, it should be expected that the range facility, as described, will be modified and improved as programs and technological progress dictate.

SECTION II
DESCRIPTION OF GUN AND MODELS

PHYSICS RANGE GUN

The primary gun used on the Flight Physics Range is an accelerated-reservoir light-gas (ARLG) gun with a launch-tube bore diameter of 20 millimeters. This type of gun was selected because of its ability to maintain a reasonably constant pressure at the base of the projectile during the launching run. Since the maximum velocity will be attained if the base pressure and acceleration are held constant during the launching run, this type of gun is a logical choice when launching fragile models at a hypervelocity aerodynamics research facility.

The ARLG gun is a special type of piston compressor light-gas gun (Fig. 2-1). It is a two-stage gun which uses a nitrocellulose propellant in the first stage, and hydrogen in the second. The hydrogen is compressed by the firing of the first stage, and the projectile is accelerated by the firing of the second stage.

The principal parts of the gun are labeled in the sketch. The first stage is, in effect, a pump consisting of a powder chamber, a piston, and a pump tube. The second stage is the gun barrel. The two stages are joined by a unit called a high-pressure coupling, and the port from the pump into the barrel is closed by a special valve called a breek valve. The diameter of the pump is constant throughout its length but tapers with a relatively gentle angle (about 9 degrees included angle) in the high-pressure coupling from pump bore diameter to barrel bore diameter. The piston is composite, constructed of a

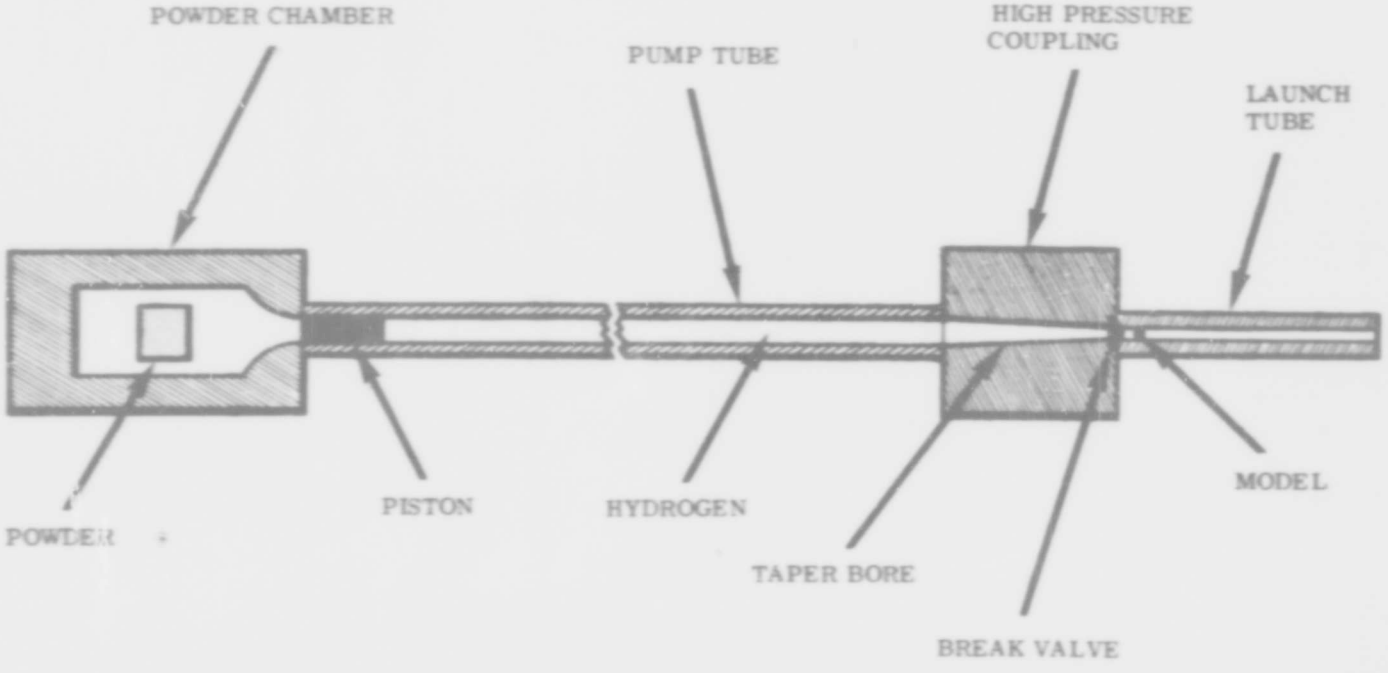

Fig. 2-1 Accelerated Reservoir Light-Gas Gun

plastic front portion, a lead slurry center portion, and a plastic base. When the gun is loaded for firing, gunpowder is placed in the powder chamber and the pump tube is filled with hydrogen. The actual gun with the principal parts labeled can be seen in Fig. 1-4.

The steps in the firing sequence are illustrated by the sketches in Fig. 2-2. Sketch A shows the gun loaded and ready for firing. In sketch B, the powder has been fired and the powder gases are driving the piston down the pump tube, compressing the hydrogen. In sketch C, the piston has reached the beginning of the tapered section in the high-pressure coupling. The initial pressure in the hydrogen has been adjusted, so that when the piston is near this point, the hydrogen has beencompressed to a pressure equal to the base pressure desired to accelerate the projectile. With the opening of the valve, the firing run of the projectile begins.

Although the piston is actually a deformable plastic, the forces acting upon it as it enters the taper (Fig. 2-2D) are large compared to its strength, and it behaves, in part, like an incompressible viscous fluid. Inertia keeps the main mass of the piston moving forward at a nearly constant velocity. As a result, the front face of the piston starts thrusting rapidly forward with increasing velocity. The piston closes the volume in the taper so rapidly that the pressure of the hydrogen at this point rises rapidly, even though it is flowing into the barrel. If the gun is operated correctly, the rise in pressure of the hydrogen at the breech just compensates the fall in pressure from breech to projectile base, and the projectile is accelerated with constant force.

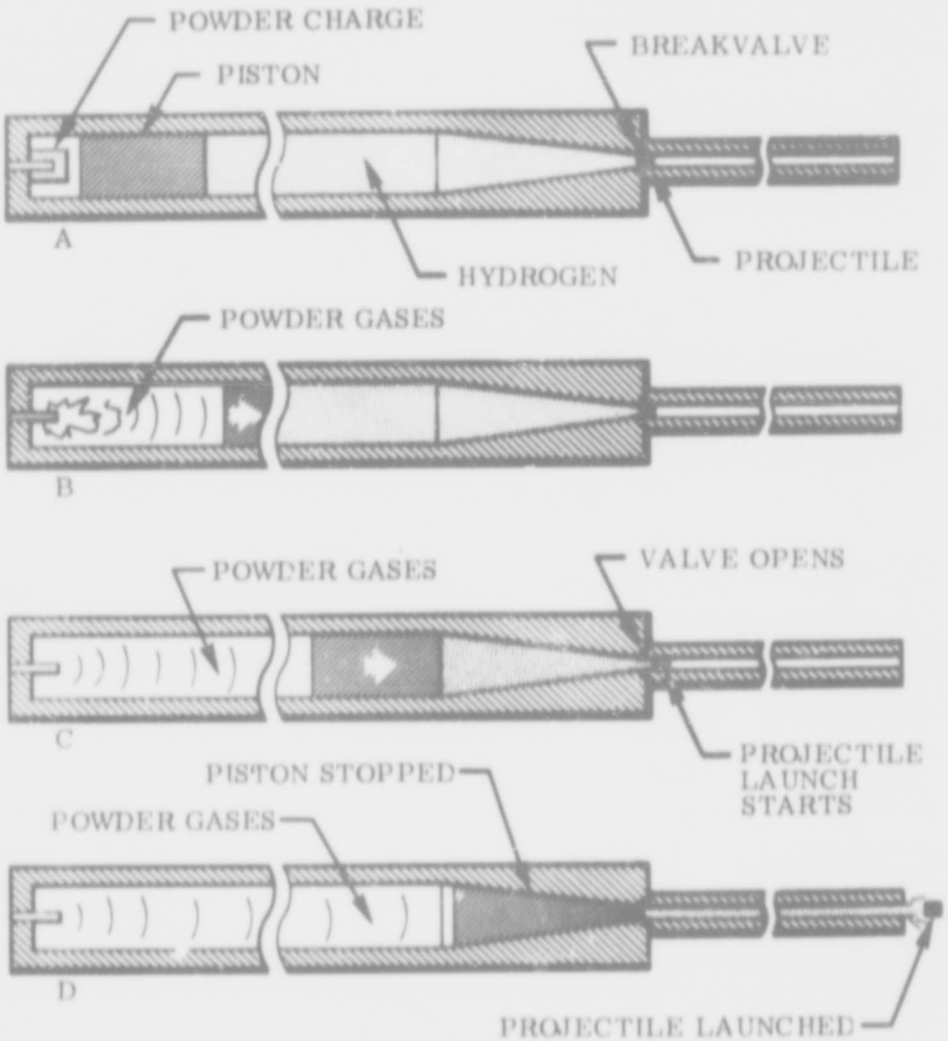

Fig. 2-2 Accelerated Reservoir Light-Gas Gun Operating Sequence

MODELS

Two types of models have been used in the Flight Physics Range – ablative and non-ablative (Fig. 2-3). The non-ablative models have a copper surface in the stagnation region, while the ablative models are plastics of various types. The front portion of all projectiles is spherical. The radius of curvature of the spherical surface is 7.5 mm for the copper-coated spheres and 13 mm for the standard model. The copper-coated spheres are constructed by electroplating copper to a thickness of 0.020 in. on a Zelux-Type-M core. The copper is placed on the standard model by crimping a cap on a plastic base (Fig. 2-3b). Two configurations of standard models have been used: the standard model has a bore-size cylindrical afterbody (Fig. 2-3a); the standard "Y" model (Fig. 2-3c) which is fired with a pusher sabot to insure stability in the gun has a very short bore-size cylindrical afterbody with a conical tail.

Ablating models are constructed of various plastics, such as high-density polyethylene, Zelux-Type-M., or Teflon, in either the standard or standard "Y" configuration. The standard ablating model is shown in Fig. 2-3a and the standard "Y" ablator is seen in Fig. 2-3c.

Sub-caliber models, such as the 15-mm spheres, must be supported in a sabot during the launch. Figure 2-3d shows the construction of a sabot and the placement of the sphere in the sabot. The sabot is formed of four pieces, and aerodynamic forces cause the sabot pieces to separate from the model after the projectile leaves the gun. When the sabot pieces have separated sufficiently from the model, they are stopped by a sabot catcher, leaving the model to proceed down the range alone.

Fig. 2-4 gives the dimensions of these types of models.

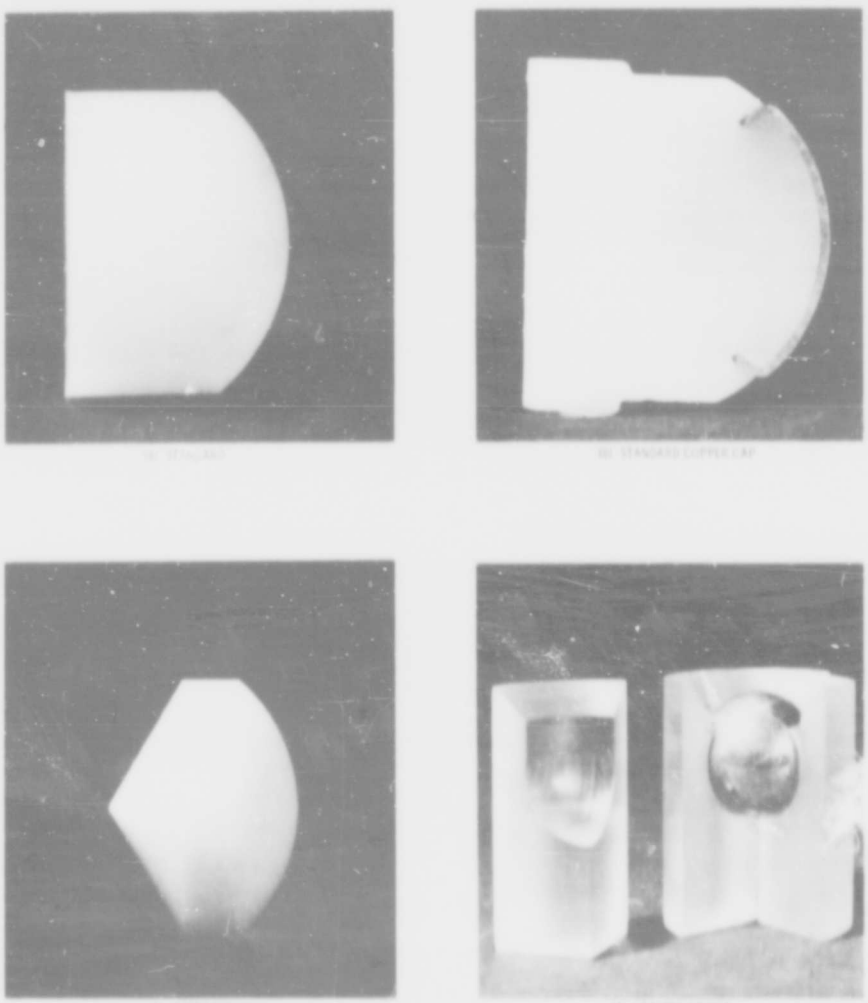

Fig. 2-3 Types of Models Used

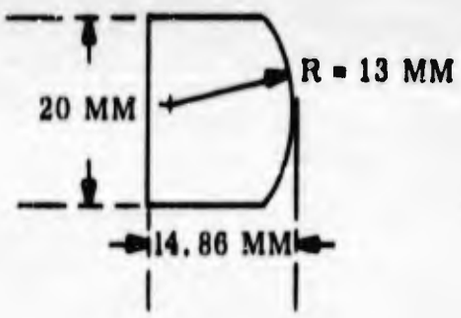

STANDARD

COPPER CAP STANDARD

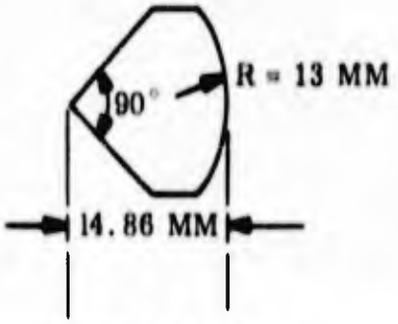

STANDARD "Y"

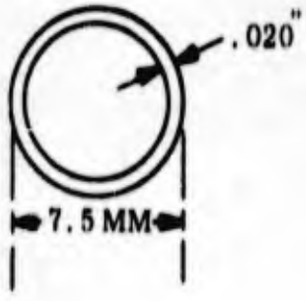

COPPER-COATED SPHERE

Fig. 2-4 Dimensions of Models

CLEANING MODELS

It was considered that any contaminants on the surface of a model would have an effect on the in-flight observables. In particular, the effect could be most significant in the case of low-ablating models in which thicknesses of less than 10^{-2} mm are ablated during the total flight time. For this reason, the following cleaning procedure is used.

Each model is cleaned in methyl ethyl keytone and then dipped in a solution of Oakite 33 (1 part) and tap water (15 parts) preheated to 140^{0}F. Finally the model is rinsed in distilled water and dried. During the whole operation the model is handled only by clean forceps.

REFERENCES

1. Curtis, John S., "An Accelerated Reservoir-Light Gas Gun," NASA TN D-1144, February 1962

2. Charters, A.C. & Curtis, John S., "High Velocity Guns for Free Flight Ranges", DRL TM62-207, Apr 1962

3. Bioletti, Carlton & Cunningham, Bernard E., "A High-Velocity Gun Employing a Shock-Compressed Light Gas", NASA TN D-307, February 1960

SECTION III
SPARK PHOTOGRAPHY APPARATUS

GENERAL

The position, attitude, and condition of the model during its flight through the instrumented flight chamber are recorded by spark shadowgraph photographs. Three spark shadowgraph instrumentation chambers are located along the flight axis of the range, and orthogonal shadowgraphs are taken at two locations in each of the shadowgraph chambers. A total of six shadowgraph stations are thus provided along the flight axis, and each of these furnishes orthogonal photographs of the model in flight. The optical axis of each station is located in a plane perpendicular to the range axis, and the orthogonal axes are at an angle of 45° from a vertical axis, allowing each station to record longitudinal, lateral, and vertical direction as well as the model's attitude about the pitch and yaw axes. Figure 3-1 indicates the geometric arrangement of the shadowgraph stations used on the range, while Fig. 3-2 is a photograph of one of the shadowgraph chambers.

The physics range is oriented in such a way that the flight axis is generally north to south; so the optical planes for the shadowgraph stations are east to west. The shadowgraph recording cameras lie 45° from the vertical on opposite sides of the range and are accordingly labeled East and West cameras. The six East shadowgraph photographs and the six West shadowgraph photographs comprise a portion of the data required for flight characteristics determination.

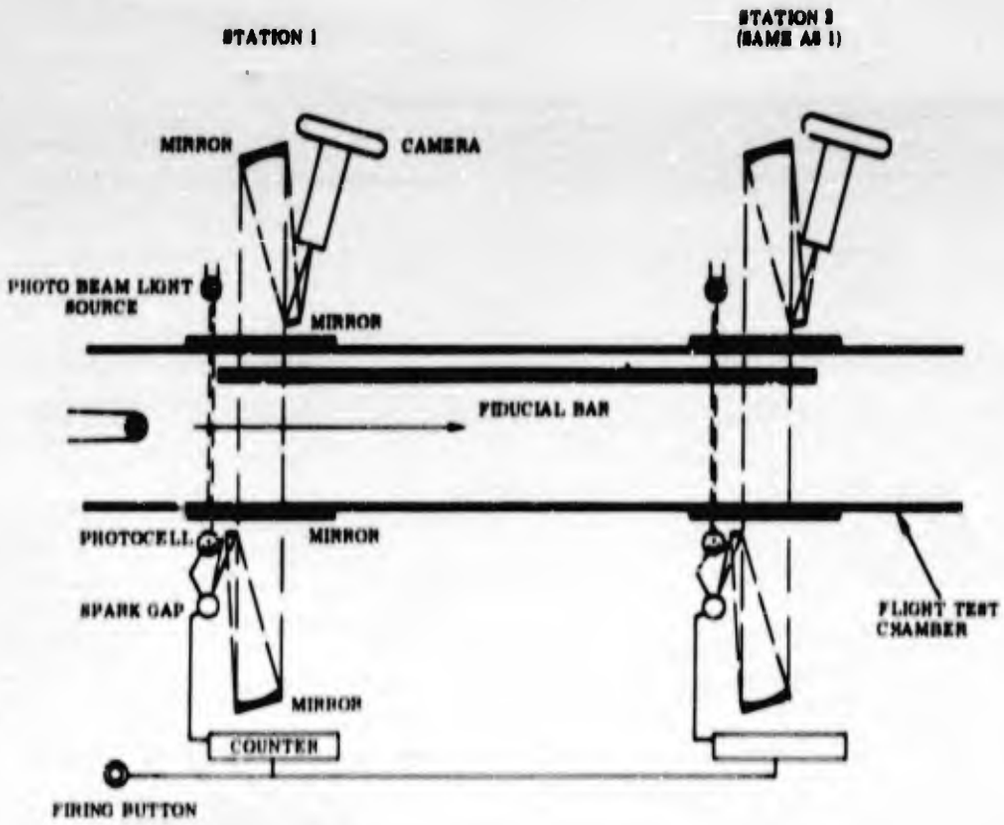

Fig. 3-1 Schematic of Physics Range Velocity Station Instrumentation

Shadowgraph photographs are taken by means of spark-gap light sources triggered by the passage of the model. As the model travels downrange, it intercepts a light beam across the flight path at the shadowgraph station. The light beam intensity is attenuated by the model and this change is detected by a photocell and used to trigger the spark-gap light sources for the station (East and West). The distance along the flight path is indicated by reference fiducial marks at each of the camera stations. The condition, attitude about the pitch and yaw axes, and the position in space of the model can thus be determined at each station by reference to the orthogonal photographs.

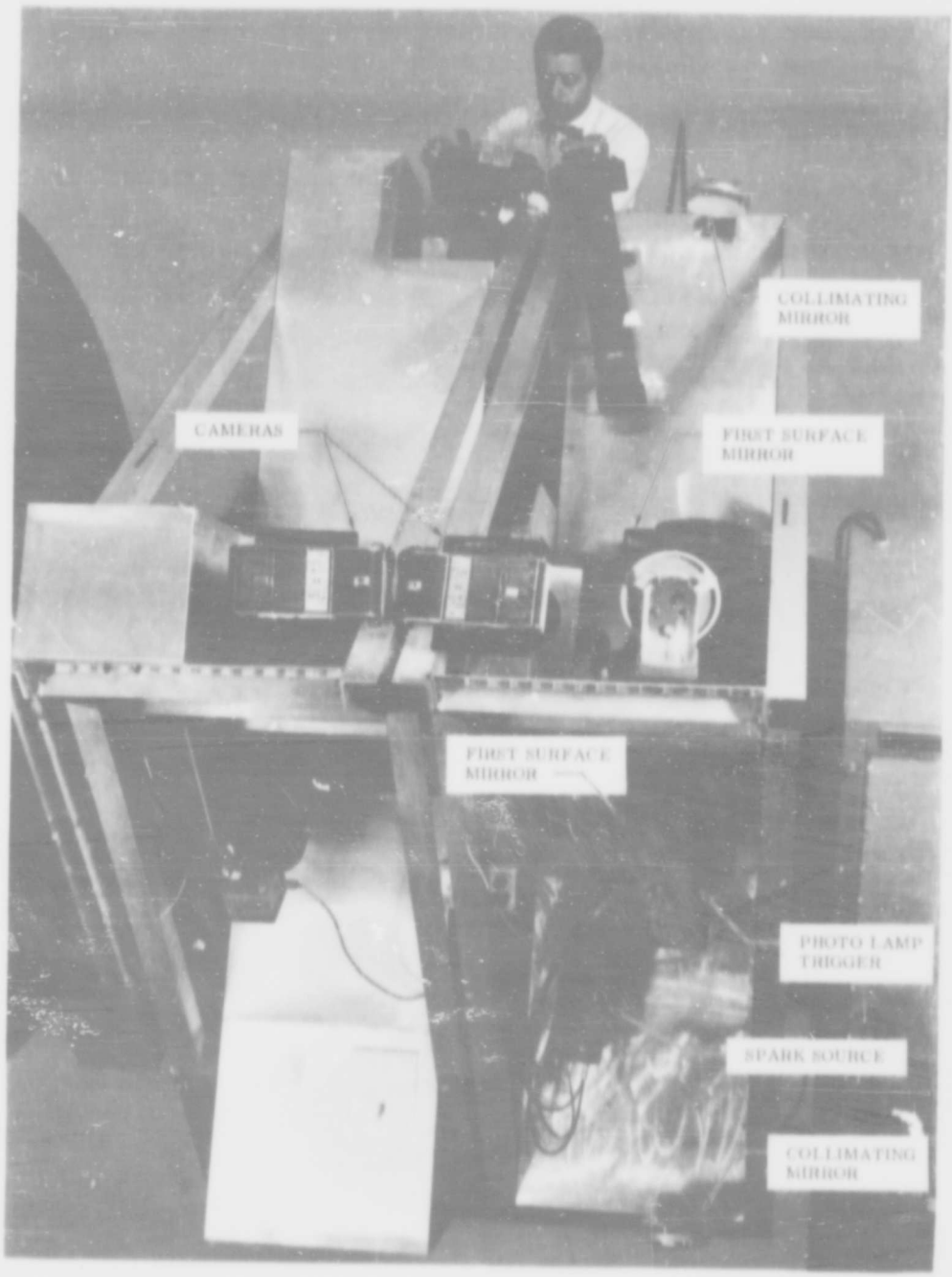

Fig. 3-2 Shadowgraph and Velocity Stations, Physics Range

A relative time-history of the model's flight is determined by use of electronic counters. A 10-megacycle electronic counter comprises a basic part of each of the shadowgraph systems. The counters for all of the shadowgraph systems are started by the firing pulse of the gun launching the model. Each counter is stopped individually by the current discharge of the spark-gap light source. Thus, the counters are started at the same instant and stopped individually by the light source for the photograph of the model. In this way an absolute relative time- and position-history of each flight is recorded, and the velocity of the model can be computed by time and distance differences.

Details of the instrumentation, accuracy of measurements, and the methods employed in the determination of flight characteristics follow in later sections of this report.

DESCRIPTION OF EQUIPMENT

Optics of Shadowgraph Instrumentation

A schematic representation of the shadowgraph station as used on the physics range is shown in Fig. 3-1. As indicated in the figure, the system is folded for compactness and rigidity. The collimated light beam across the range is about 6 in. in diameter and determines the field of view of the camera. The light source for each photograph is a spark-gap discharge limited to a diameter of 0.015 in. (0.0381 cm). The telecentric stop in the camera tube is 0.1 in. (0.254 cm) diameter. The focal length of the collimating and de-collimating mirrors is 48 in. (122 cm) and the distance from telecentric stop to camera plate is about 24 in. (61 cm). The picture thus recorded is about half-size. Mirror surfaces are true within 1/4 wavelength (Na).

Geometry of Shadowgraph Instrumentation

Orthogonal shadowgraph systems are located at each shadowgraph station along the range. There are a total of six such stations for flight characteristic determinations, with a pair of stations located in each of three shadowgraph chambers. For reference position on the shadowgraph photograph, each shadowgraph chamber contains a fiducial bar consisting of a single length of carbon steel with the reference edge suitably notched for the determination of axial position. The notches are visible in the spark photograph and are spaced 36 in. (nominal) apart. The edge of the bar has been ground to a knife-edge at the section of the reference notches, and this edge is used to determine the axis of the flight range. A spatial calibration of the range at 70^{0}F has been made. Axial and lateral position of the stations can be determined to within 0.01 in. (.0254 cm) with temperature correction as necessary.

The planes of the shadowgraph systems are perpendicular to the flight axis to within $\pm 1^{0}$. The shadowgraph systems for each station are within $\pm 1^{0}$ of 90^{0} to each other and $\pm 1^{0}$ of 45^{0} from the vertical.

Shadowgraph Light Source

The source of light for the shadowgraph photographs is created by the discharge through a spark gap of about three joules of energy. The total time duration of the spark is on the order of 0.3 microsecond, and the characteristic of the discharge is such that the ratio of light intensity to maximum light intensity is 1 to 3 during a time of 0.2 microsecond (see "High Power Short Duration Spark Discharge", Kovasznay - Vol. 20, No. 9, 696-697, Sep 1949, The Review of Scientific Instruments). A trigger electrode is used to break down an air gap of

0.015 in. diameter and start the arc discharge from the capacitive storage.

Shadowgraph Cameras

Shadowgraph cameras are a part of the shadowgraph system previously described. Polaroid Type 47, 3000-speed film is normally used for data recording, but provision has been made to use cut film. The resulting picture is about one-half the normal size; i.e., sizes and distances on the photograph must be multiplied by a scale factor of about 2.0 in order to correct to full scale (each shadowgraph system has been calibrated individually and the exact correction factor established. The actual correction factors range from 1.5 to 1.9).

Shadowgraph Light-Source Trigger

At each of the shadowgraph stations during its flight downrange, the model passes through a collimated horizontal light beam which is perpendicular to the axis of the range and about 5 in. (12.7 cm) in height and 3/4 in. (1.9 cm) in width. The light source is a six-volt, projector-type incandescent lamp and the beam is focused on an RCA Type 6570 phototube. When the model passes through the light beam, the phototube current change is amplified by a circuit employing a thyratron trigger; this provides a voltage to the trigger electrode in the spark-gap light-source unit, and the resulting discharge of the capacitance through the air gap provides the pulse to stop an electronic counter which has been started by the gun-firing circuit. Since the counter is stopped by the discharge of the capacitors providing the light source, it records the exact time in the sequence at which the photograph is made.

Since one light-source trigger circuit is provided for each shadowgraph station, there are a total of six trigger circuits for shadowgraph photography on the physics range.

Electronic Counters

The electronic counters and frequency sources employed in the shadowgraph photography systems are Beckman Types 7270 and 7070, digital counter chronographs operated at 10 megacycles per second. The 7270 counter serves as the clock-pulse generator for all counter units to insure counting at a common rate. The 7270 oscillator unit is rated to have a maximum time stability of 3 parts to 10^7 per week. The counters have an accuracy in time count of ± one count or ± 1/10 of a microsecond.

One counter is used for each of the shadowgraph systems so that each station has an east and west time count. The use of the time count in conjunction with the shadowgraph photographs for flight characteristics is fully described in another section of this report.

SECTION IV
FLIGHT KINEMATICS

COORDINATES OF THE MODEL ALONG ITS FLIGHT PATH

The fields of view of all recording instruments are positioned with respect to a common set of coordinate axes which have been accurately surveyed throughout the range. Defined as an orthogonal system, the positive x-axis points downrange and coincides with the surveyed centerline of the range, the positive y-axis is the horizontal axis pointing to the right when looking downrange, the positive z-axis points vertically downward. This arrangement, therefore, corresponds to a right-hand coordinate system.

The survey of the range was made by establishing crosshairs at each fiducial plane along the range and accurately measuring the x-distance of these planes by means of a steel tape from a reference point. Corrections were then made for the tension applied to the tape during the measuring operation and for the expansion of the tape due to elevated temperature of the ambient air.

At each station the distances of the fiducial bar from the range survey axis were then established in the east and west shadowgraph planes by accurately placing a calibrated ball on the survey axis and measuring its distance to the fiducial bar. Coordinates of the model's trajectory are determined from the spark photography records (refer to Fig. 3-1).

After the model emerges from the launch tube, it describes a flight path which deviates somewhat from the survey axis of the range. In order to locate the model with respect to this survey axis at any distance downrange or at any time t, accurate marks have been placed on the fiducial bar, installed along the upper portion of the range.

On the shadowgraphs, taken at Stations 1 — 6 downrange, the distances of the model from the fiducial bar can be measured. The problem is to determine the x, y, z coordinates of the model from the coordinates of the fiducial bar and the measurements of the spark photographs.

Since these photos are taken in planes inclined at 45° from the horizontal and vertical, a rotation of these coordinates into the horizontal y-axis and the vertical z-axis is necessary to determine the actual y and z coordinates of the model; the x coordinate is not affected by the rotation. The following paragraphs describe the derivation of the transformation formulas.

The shadowgraphs are taken in two planes -- the east plane and the west plane — which include an angle of 90° between them and which are inclined at 45° from the horizontal (Fig. 4-1). The shadowgraph pictures show the distances y_s and z_s of the model from the fixed fiducial bar. These distances can be measured directly from the pictures. The distances of the fiducial bar from the range survey axis p in the east plane and q in the west plane are known for each station.

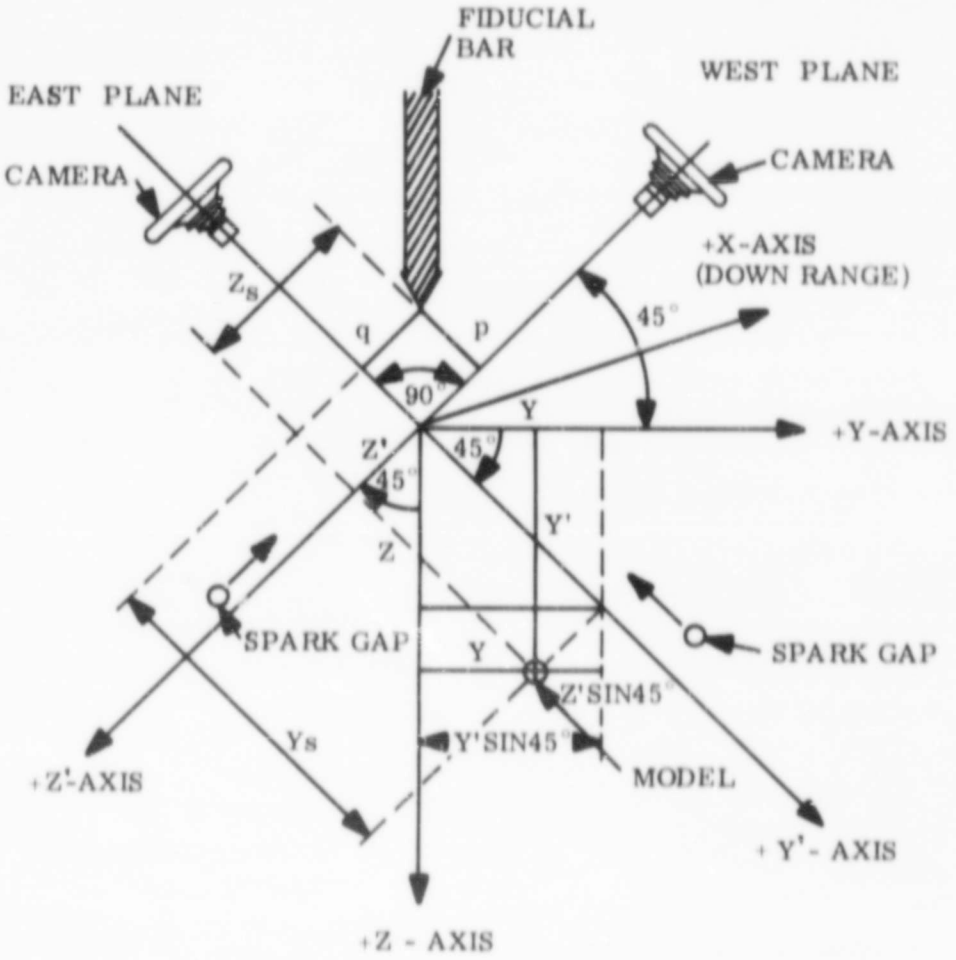

Fig. 4-1 Transformation of Model Coordinates

Thus:

$$y_s = y' + p$$

$$z_s = z' + q$$

or

$$y' = y_s - p$$

$$z' = z_s - q$$

The distances y' and z' denote the location of the model with respect to the survey axis, or true x-axis, of the range measured in the inclined planes of the spark station optical system. In order to obtain the location of the model in the y, z coordinate system, apply the following conversion formulas which are apparent from the geometry.

$$y = y' \sin 45^\circ - z' \sin 45^\circ = 0.70711\ (y_s - z_s + q - p)$$

$$z = y' \sin 45^\circ + z' \sin 45^\circ = 0.70711\ (y_s + z_s - p - q)$$

Coordinates y and z establish horizontal and vertical distances of the model from the true x-axis of the range and provide the inputs into the equation furnishing the flight trajectory of the model to permit a determination of the location of the model at any time t or at any downrange station x.

DETERMINATION OF VELOCITY AND LOCATION OF THE MODEL

The observables are recorded by the instruments along the flight test and radar chambers as the model traverses their fields of view. From these records must be determined the variations in the observables around the model and following in its wake; that is, the variations along the flight path measured with respect to a fixed point on the model. Distance therefore, is the independent variable.

Actually, the observables are recorded by the instruments as functions of time, so that time, rather than distance, is the operating independent variable. First, there is the time at which the instrument begins to record – the start time of the oscilloscope sweep. This is recorded by a cycle counter chronograph which as been started with all other counters by common timing signal (from the gun-firing circuit) and is stopped by the same signal from the instrument's trigger that starts the CRO sweep. Second, there is the time along the CRO trace which is determined by the sweep rate.

The problem in determining the variation in the observable with respect to the model is to establish the relation between time and distance. An example of the information desired is shown in Fig. 4-2. Here the problem is to relate the peaks of the amplitude record (from the transverse focused microwave probe) to the flow field geometry shown in the schlieren record.

In order to solve this problem, the position of a reference point fixed in the model must be known as a function of time. Specifically, the time at which the reference point crosses the center of the field of view of the recording instrument and the velocity of the model at this time must be known. Knowing this, the model's reference point can be placed precisely on the CRO trace of the recording instrument; and taking advantage of the fact that the velocity varies slowly along the trajectory in a majority of the tests, the relation between time and distance is then

$$\Delta x = v \Delta t$$

where the differentials are measured from the center of the field of view. Thus, the first task in reducing the flight data is to determine

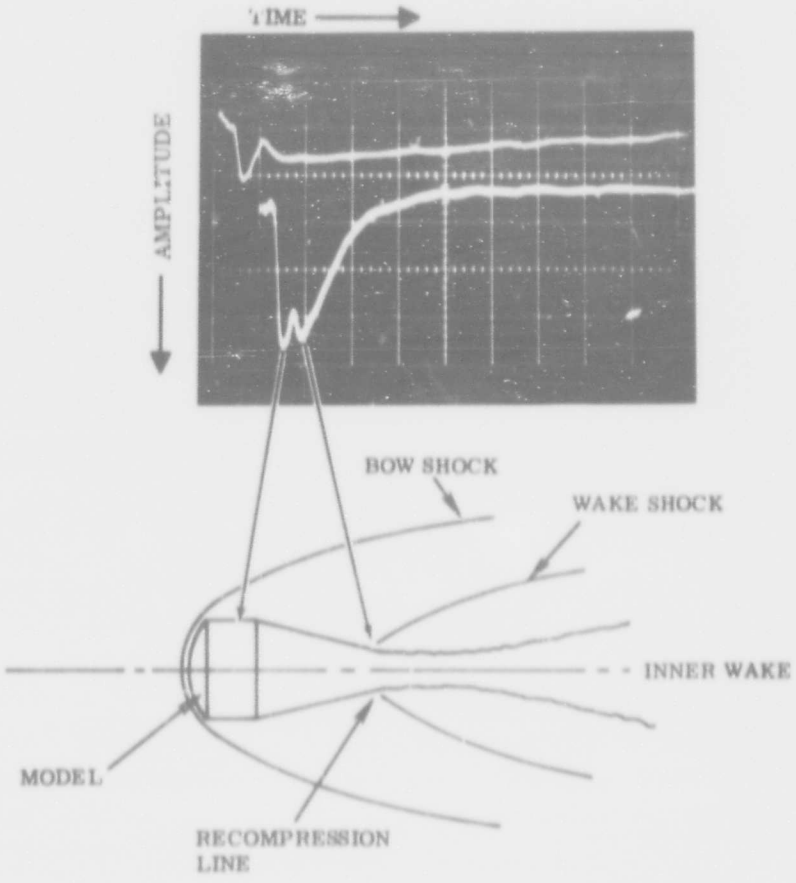

Fig. 4-2 Typical Microwave Oscilloscope Trace

the kinematics of the model's flight. The records basic to the kinematics come from the spark photography stations and the cycle counter chronograph. Each station records x, y, z and t, and the attitude of the model — the angles of pitch and yaw (plus roll in special tests). Establishing the flight kinematics begins with the derivation of the equations of motion, so the problem is to determine the constants in the equations of motion from the discrete values of x, y, z and t measured at the spark stations. The procedure for making this reduction is described subsequently, following the derivation of the equation of motion.

In order to find the analytical relationships between v and t, or between x and t, use is made of the fact that the sum of the inertia forces and external forces acting on the model is zero:

where m = mass of the model [kg mass]
v = velocity of the model [km/s]
t = time [seconds]
D = Drag force [kg force]

Drag D may be expressed by the term:

$$D = C_D \frac{\rho v^2}{2} A$$

where C_D = drag coefficient [dimensionless]
ρ = density of gas $\frac{kg}{m^3}$
A = model reference area $[cm^2]$

Thus, $$m \frac{dv}{dt} = - C_D \frac{\rho v^2}{2} A$$

or $$\frac{1}{v^2} \frac{dv}{dt} = - \frac{C_D \rho A}{2m}$$

Letting $$\frac{C_D \rho A}{2m} = K$$

and separating the variables,

$$\frac{dv}{v^2} = - K \, dt \ .$$

This equation can be easily integrated provided C_D or K is a constant. This condition is usually met for blunt bodies and short trajectories.

Upon integration, a relationship between v and t is obtained:

$$- \frac{1}{v} \Big]_{v_0}^{v} = - Kt \Big]_{t_0}^{t}$$

or $$\frac{1}{v} = \frac{1}{v_0} + K(t - t_0) \ .$$

In order to determine the value of K, a plot of $\frac{1}{v}$ versus t can be made from known values of these variables. This plot usually results in a straight line where K represents the constant slope. Figure 4-3 shows a typical example of such a plot. Thus, the velocity v of the model can be found for any given time t if the constant K is known together with the initial conditions v_0 and t_0.

The graph from which K is obtained is plotted in the following way: two or more values of the velocity are calculated for a given test with the corresponding values of time. If small enough intervals are taken over the range, the velocities in these intervals can be considered constant.

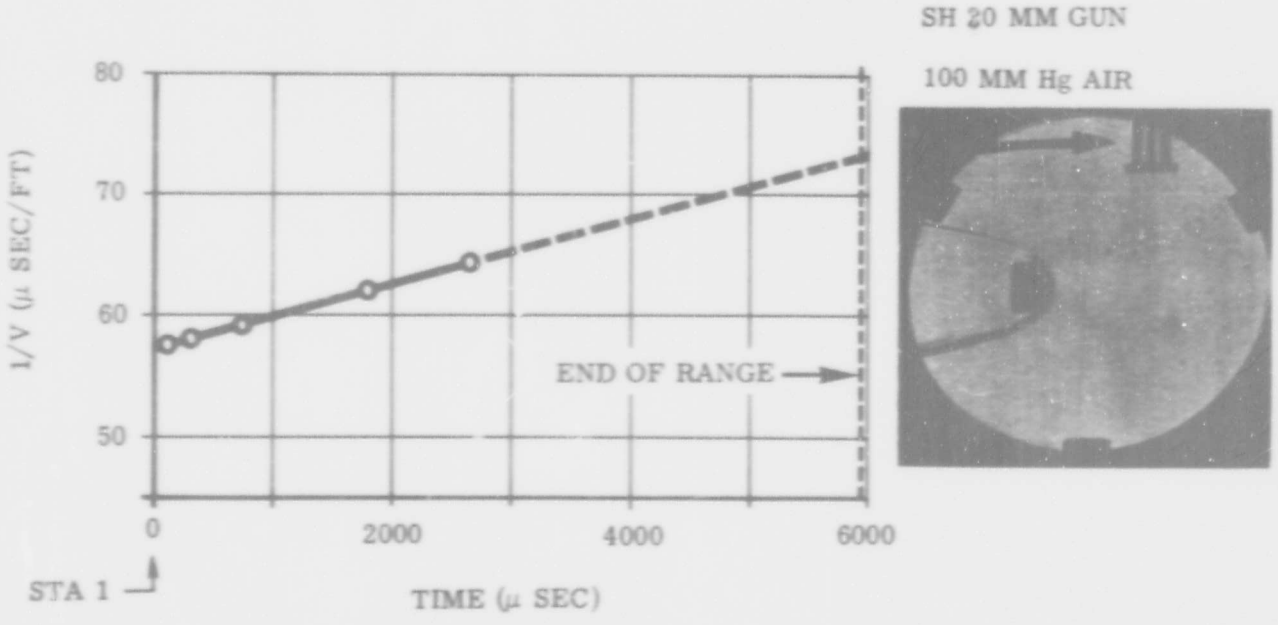

Fig. 4-3 Measurement of Velocity

The large range (B-range) of the Flight Physics Laboratory has six shadowgraph stations where time measurements are taken concurrently with spark shadowgraphs of the model. In addition, time counts are taken at the various instrumentation stations. (See Fig. 4-4.)

Velocities between pairs of stations can be calculated from the known model distances and the time counts at these distances. For example:

$$V_{3,4} = \frac{x_4 - x_3}{t_4 - t_3} \quad \text{etc.}$$

The corresponding mean values of time are similarly calculated for these intervals:

$$t_{3,4} = \frac{t_3 - t_4}{2} \quad \text{etc.}$$

A plot of the values of $\frac{1}{V}$ and t yields the slope K.

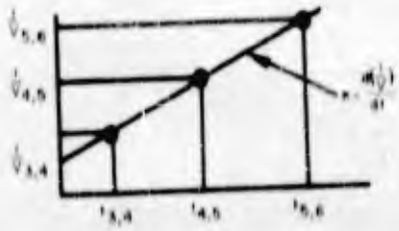

One is reminded here that K is constant only if the drag coefficient, C_D, remains constant as stated before, if the model does not oscillate, and if the mass, m, of the model remains constant. However, even if ablation takes place, the decrease in mass is negligible in most cases.

The above method of determining K permits calculation of the drag coefficient of the model, since, from Eq. (1),

$$C_D = \frac{2m}{\rho A} K .$$

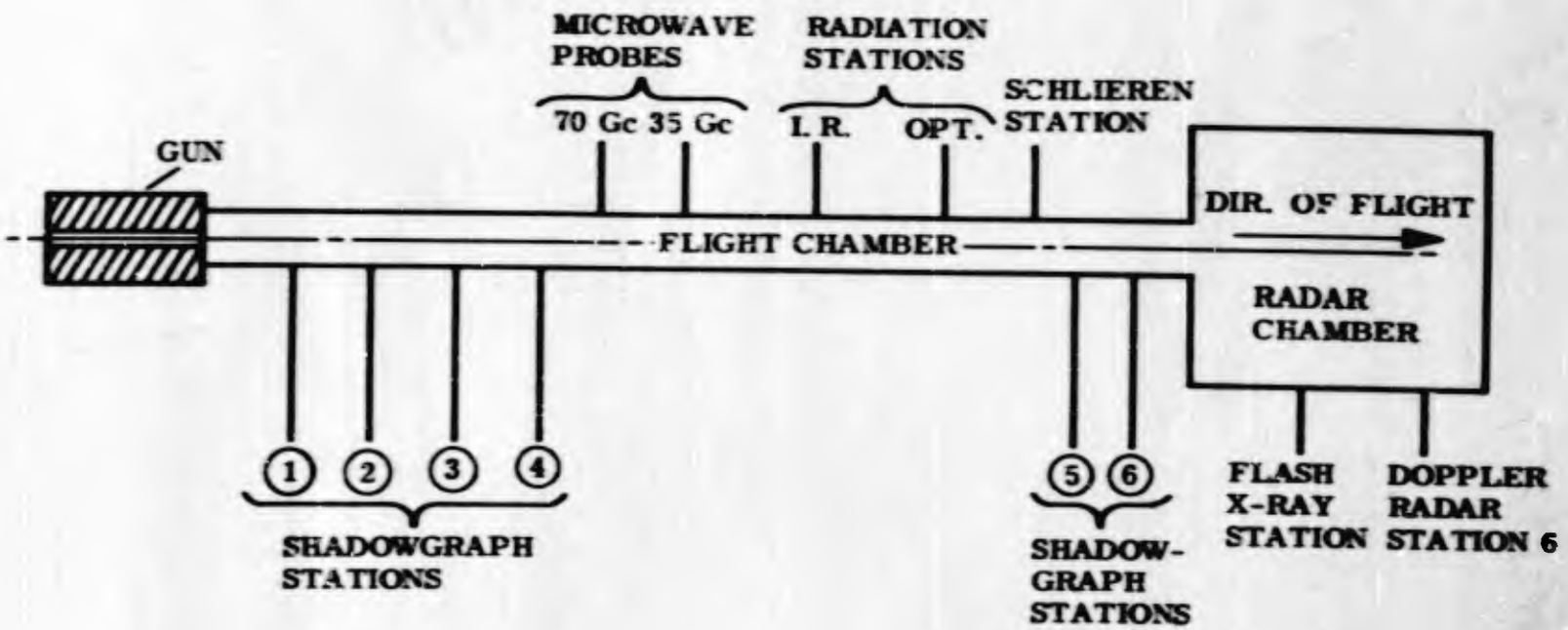

Fig. 4-4 Schematic of Timer Stations

In calculating the reciprocals of the velocities $\frac{1}{v}$ for the determination of K, the actual locations of the model on the x-axis rarely coincide with the fiducial mark. Usually the nose of the model, which is used as the reference point, is photographed fractions of a cm ahead of or behind the fiducial plane. These small corrections, Δx, are measured directly off the spark photographs of the model at each station. For this purpose the shadowgraphs are equipped with accurate hairline grids which permit direct measurement of the distance Δx of the model reference point (nose contour) from the fiducial plane.

Illustrative Example

To illustrate the method of obtaining a numerical expression for the velocity equation

$$\frac{1}{v} = \frac{1}{v_0} + K(t - t_0)$$

two sketches of typical spark photographs of a blunt-nosed model at Stations 1 and 2 are shown in Fig. 4-5.

The velocity $v_{1,2}$, is found from the equation:

$$v_{1,2} = \frac{(914.4 + \Delta x_2 - \Delta x_1)}{(t_2 - t_1)} \quad \text{mm/}\mu\text{sec (km/sec)}$$

where Δx and t are in mm and microseconds, respectively.

Using typical numerical values,

$x_1 = +17.78$ mm $\qquad x_2 = +8.89$ mm

$t_1 = 713069\ \mu$ sec $\qquad t_2 = 715656\ \mu$ sec

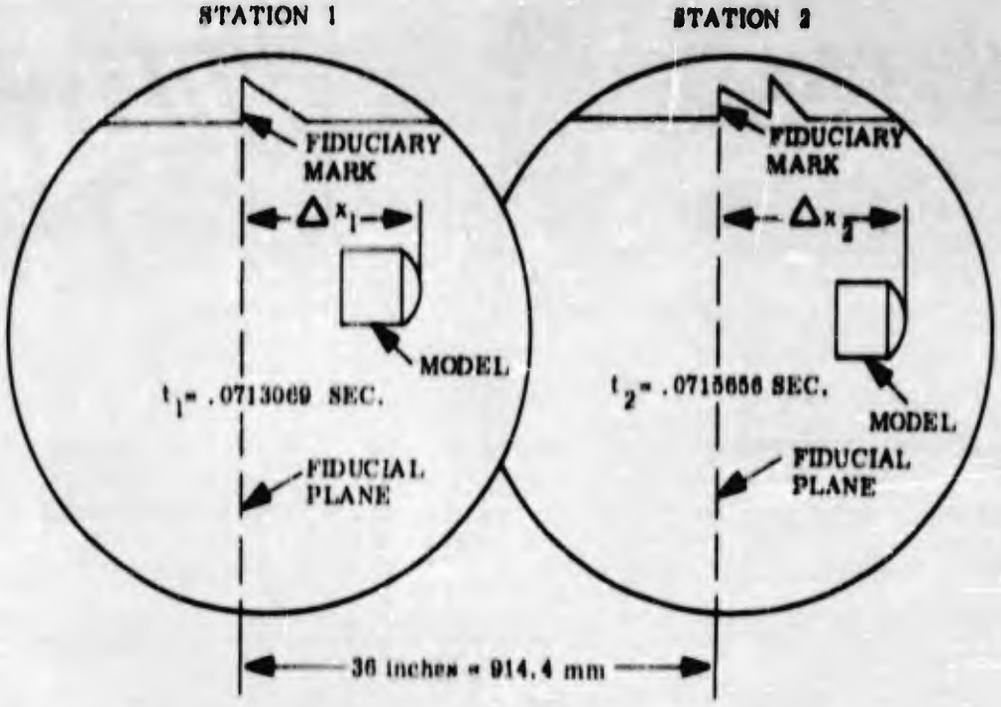

SKETCHES OF TYPICAL SPARK PHOTOGRAPHS OF BLUNT-NOSED MODEL

Fig. 4-5 Sketches of Typical Spark Photographs of Blunt-Nosed Model

we find the velocity to be

$$v_0 = \frac{914.40 + 8.89 - 17.78}{71565.6 - 71306.0} = 3.502 \text{ mm}/\mu\text{sec (km/sec)}$$

In the same fashion, $v_{3,4}$ and $v_{5,6}$ can be found between Stations 3 — 4 and 5 — 6, respectively. Plotting the reciprocals of these velocities versus the corresponding times t, K can be found from the constant slope of the resulting straight line.

With the values of the initial conditions v_0, t_0 and K, Eq. (2) can be solved for any given value of t. Together with the downrange distance x as a function of time, accurate location of the model (as well as location of points along the body of the model and along the wake) is now possible.

The location x of the model during flight at any time t, or the location of a point at a fixed distance from the model can now be found from the relationship

$$x = f(t) \ .$$

This equation is determined by integration of Eq. (2). Rewriting this equation,

$$\frac{1}{dx/dt} = Kt - Kt_0 + \frac{1}{v_0}$$

or

$$\frac{dt}{(t - t_0 + 1/Kv_0)} = Kdx \ .$$

Integration yields the equation

$$\ln (t - t_0 + \frac{1}{Kv_0}) \Big]_{t_0}^{t} = Kx \Big]_{x_0}^{x}$$

which, upon substitution of the limits and solving for $(x - x_0)$, takes on the final form of

$$(x - x_0) = \frac{1}{K} \ln Kv_0 (t - t_0 + \frac{1}{Kv_0}) \text{ or}$$

$$x = x_0 + \frac{1}{K} \ln \left[Kv_0 (t - t_0) + 1\right]$$

where K, t_o, x_o and v_o are constants. If the initial value x_o is taken at the origin, then

$$x_o = 0$$

and the equation simplifies to

$$x = \frac{10^3}{K} \ln \left[K v_o (t - t_o) + 1 \right] \quad . \tag{3}$$

where x is in meters and the constant K in Km^{-1} units.

If it is desired to find the velocity at any station of the range, then a convenient equation relating v to x is

$$v = f(x)$$

To start, the equation

$$\frac{1}{v^2} \quad \frac{dv}{dt} = -K$$

can be rewritten as

$$\frac{1}{v^2} \; v \; \frac{dv}{dx} = -K$$

or

$$\frac{1}{v} \; dv = -K dx \quad .$$

Upon integrating,

$$\ln v \Big]_{v_o}^{v} = -Kx \Big]_{x_o}^{x}$$

and by substituting the limits, the equation

$$\ln v - \ln v_o = -K (x - x_o)$$

is obtained. If the initial value of x is conveniently taken as

$$x_0 = 0$$

the final equation is

$$\ln\left(\frac{v}{v_0}\right) = -xK \tag{4}$$

Equations (2), (3) and (4) express the basic kinematics of the range. They are so programmed for computer calculations, that, for any one of the variables x, t and v, the other two can be obtained as a readout.

SECTION V
COMPUTATION OF CONSTANTS AND ANALYSIS OF ERROR IN EQUATIONS OF MOTION

In order to arrive at exact numerical values for the velocity of the model at each station at each given time, certain measured times and distances must be known. These are the x distances of the model from the reference station, Station 3, and the times t corresponding to these distances (Fig. 5-1). In the case of the physics range, downrange distances are computed from shadowgraph pictures in two planes — the East plane and the West plane. There is a small difference in time counts (and, therefore, in x distances) in these two planes. The computation consists in a simple addition of the known distance of the fiducial plane from the reference point x and the incremental distance of the model from the fiducial plane x, as measured on the shadowgraph picture.

Although shadowgraphs are available for Stations 1 and 2, in the future these pictures will not be utilized for velocity analysis. The reason is that at these stations the model is still accompanied by the sabot pieces which are not removed from the model until it reaches the sabot deflector plate ahead of Stations 2 and 3. Moreover, a check valve will be placed between Stations 2 and 3 so that the model may fly in two different atmospheres upstream and downstream of this valve. Thus, Station 3 will be the first point downrange at which the model can be considered to be in undisturbed flight. *

*For the first 222 rounds of the Hypervelocity Range Research Program, the check valve was not in use, and Stations 1 and 2 may be used as measuring points for time and distance.

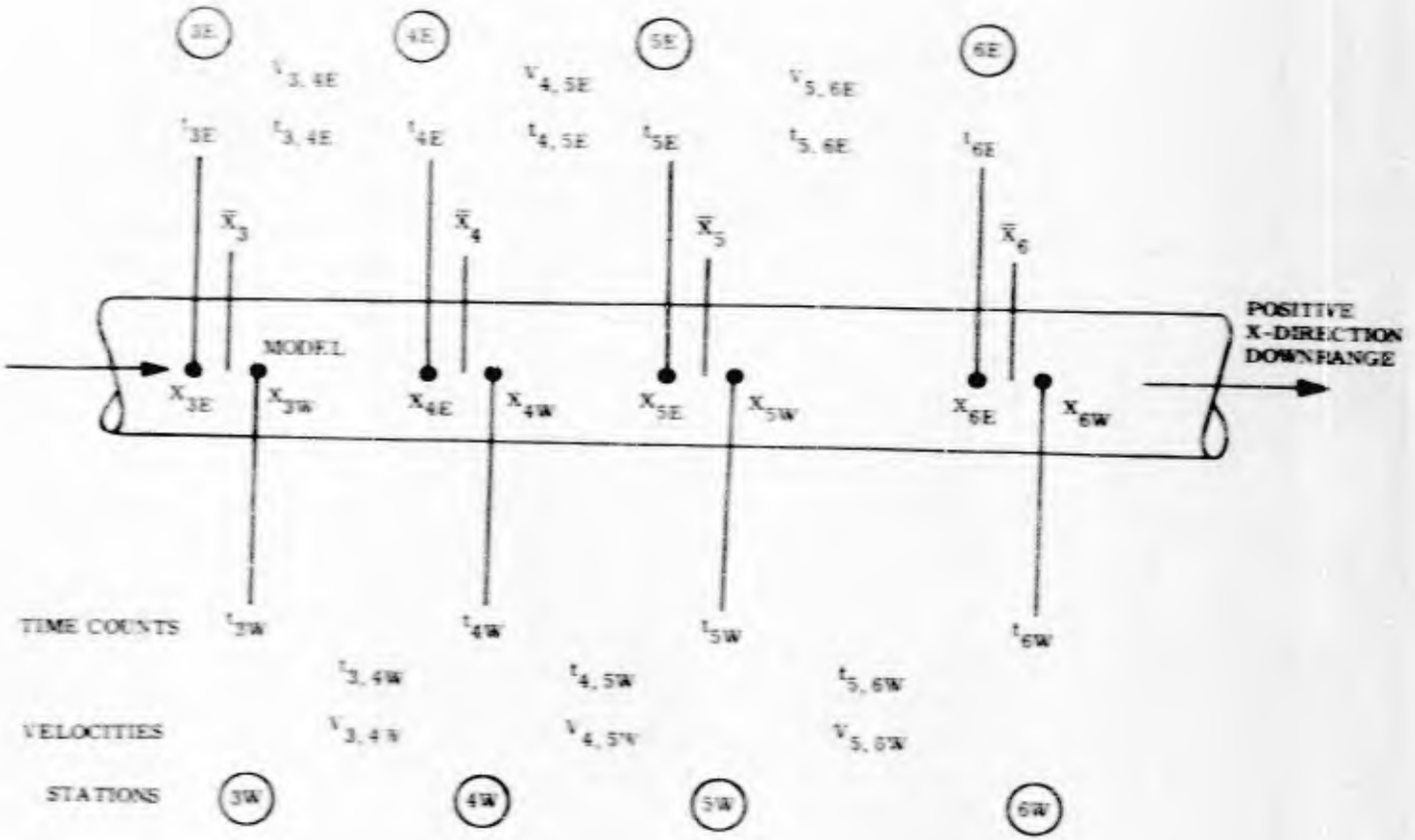

Fig. 5-1 Diagram of Downrange Distances and Time Counts

At a given downrange station, the fiduciary plane marks the distance x which is the same for both East and West shadowgraphs. However, model distances x from the fiducial plane differ; and since each East and West station has its own circuit delay, the time values for each pair of planes also differ slightly.

Thus, it is necessary to record two x distances for each downrange station and two time counts. In addition, the X-ray photography station carries its own time counter, and the time count and model distance x for this station are similarly recorded, so that the total input of data consists of the following tabulated items:

DISTANCES		TIME COUNTS	
x_{3E}	x_{3W}	t_{3E}	t_{3W}
x_{4E}	x_{4W}	t_{4E}	t_{4W}
x_{5E}	x_{5W}	t_{5E}	t_{5W}
x_{6E}	x_{6W}	t_{6E}	t_{6W}
$x_{X\text{-ray}}$		$t_{X\text{-ray}}$	

The next step, then, consists in determining the mean velocities between Stations 3 and 4, 4 and 5, 5 and 6, and between Station 6 and the X-ray Station in both the east and west planes.

These velocities are computed from the following simple equations:

$$v_{3,4W} = \frac{x_{4W} - x_{3W}}{t_{4W} - t_{3W}} \qquad v_{4,5W} = \frac{x_{5W} - x_{4W}}{t_{5W} - t_{4W}}$$

etc.

$$v_{3,4E} = \frac{x_{4E} - x_{3E}}{t_{4E} - t_{3E}} \qquad v_{4,5E} = \frac{x_{5E} - x_{4E}}{t_{5E} - t_{4E}}$$

Altogether seven velocities are obtained, namely:

$v_{3,4E}$	$v_{5,6E}$
$v_{3,4W}$	$v_{5,6W}$
$v_{4,5E}$	$v_{6,\ X\text{-ray}}$
$v_{4,5W}$	

Similarly, the average time counts which correspond to these velocities can be computed:

$$t_{3,4W} = \frac{t_{3W} + t_{4W}}{2} \quad , \qquad t_{4,5W} = \frac{t_{4W} + t_{5W}}{2} \qquad \text{etc.}$$

The last velocity, that between Station 6 and the flash X-ray plane $v_{6,\ X\text{-ray}}$, requires a slightly modified equation since the X-ray station has neither an East nor West plane. Thus, first the average values of x and t between the East and West planes of Station 6 must be computed before the velocity can be found. Accordingly,

$$\bar{x}_6 = \frac{x_{6E} + x_{6W}}{2} \quad , \qquad \bar{t}_6 = \frac{t_{6E} + t_{6W}}{2}$$

and

$$v_{6,X\text{-ray}} = \frac{x_{X\text{-ray}} - \bar{x}_6}{t_{X\text{-ray}} - \bar{t}_6} \quad .$$

With these given values of velocities and the corresponding time counts, Eq. (2), where $\frac{1}{v}$ is expressed as a function of time, is used.

If all of these corresponding points were plotted, a theoretically straight line would result as seen in Fig. 4-3. However, in actuality, the points corresponding to the measured velocities do not necessarily fall on a

straight line, so the computer, by the method of least squares, will have to find the line with the best fit for the given points. From such a line then, the slope K can be determined, resulting in a linear equation of the form $\frac{1}{v} = a + bt$ where the constant b equals $b = K$ and the constant a equals $a = (\frac{1}{v_o^*} - Kt_o)$ corresponding to

$$\frac{1}{v} = \frac{1}{v_o^*} - Kt_o + Kt = a + bt$$

The constants a and b can be computed from the curve of best fit to the given values of v and t.

The two initial values v_o^* and t_o can now be obtained by specifying a given time t_o and computing the first approximation of the initial value of the velocity, v_o^* from the relation:

$$v_o^* = \frac{1}{a + Kt_o}$$

The time constant t_o is derived from the time counts at Station 3, the reference station of the range. It is the average between time values at the east and west planes, thus

$$t_o = \frac{(t_o)_{3W} + (t_o)_{3E}}{2} .$$

These time values $(t_o)_{3W}$ and $(t_o)_{3E}$ correspond to the fixed location of the fiducial plane on the shadowgraphs at Station 3. The actual time counts of the model at Station 3, t_{3W} and t_{3E}, must, therefore, be corrected for the distance between the model and the fiducial plane.

Thus, $(t_o)_{3W} = (t_{3W} + \Delta t_{3W})$ and $(t_o)_{3E} = (t_{3E} + \Delta t_{3E})$ where

$$\Delta t_{3W} = \frac{\Delta x_{3W}}{v_{3,4W}} \text{ and } \Delta t_{3E} = \frac{\Delta x_{3E}}{v_{3,4E}} .$$

With the initial value t_o established, v_o^* can now be computed. This velocity satisfies the equation and so constitutes a point on the curve which corresponds to the abscissa t_o. A correction to this velocity v_o^* can be made by stipulating that the equation should, in addition, satisfy the condition of matching a given downrange distance x with the corresponding time count t at that station, say, Station 6 or the station of the X-ray flash unit. For this purpose, Eq. (3) can be modified by substituting for v_o the term

$$v_o' = v_o^* + \delta v_o$$

Thus, the equation reads:

$$x = \frac{10^3}{K} \ln \left[(v_o^* + \delta v_o) K (t - t_o) + 1 \right]$$

Solving for the velocity correction term the equation becomes:

$$\delta v_o = \frac{e^{(10^{-3} \times K)} - \left[v_o^* K (t - t_o) + 1 \right]}{K(t - t_o)}$$

By substituting the values for x and t at either Station 6 or at the flash X-ray unit, a numerical value for δv_o is obtained from which the corrected value of the initial velocity v'_o can be found.

This corrected velocity now permits the computation of the downrange distances x at the various stations as functions of the measured times t. From a range survey, the actual station distances have been determined to a high degree of accuracy. A comparison of these measured points x_{meas} with computed values x_{comp} permits an examination of the accuracy of the method of velocity determination. These residuals, δ, which may be found from

$$\delta = x_{meas} - x_{comp}$$

define the mean error, or the root mean square e_x by application of the well known formula:

$$e_x = \sqrt{\frac{\sum_{1}^{n} \delta 2}{(n-1)}} \quad .$$

For each round fired, the error e_x is found from a computer program and listed as one of the characteristics of the round in the data report.

SECTION VI
MODEL IMPACT ON REFLECTOR PLANE

A reflector for the doppler radar beam is placed at the downrange end of the radar chamber. The model perforates the reflector prior to striking the impact area, and the perforation provides a record of the y and z coordinate at the end of the flight. The reflector consists of a thin sheet of aluminum located in a vertical plane and inclined at a 45^0 angle to the range axis (see Fig. 6-1).

In order to establish the coordinates of the model impact point on the reflector, use is made of the known distances of the reflector reference point in the x, y, z coordinate system. These are

$x_{\mathbb{C}_L}$ Reflector

$y_{\mathbb{C}_L}$ Reflector

$z_{\mathbb{C}_L}$ Reflector

The distances of the model impact point from the reference point $\mathbb{C}_L$ projected on the reflector are measured in the plane of the reflector. The actual x and y distances of the impact point with respect to this range axis must be taken as the projection of the horizontal distance in the reflector plane.

The impact coordinates, therefore, are computed from the following relationships:

$$x_{impact} = y_{impact}$$

$$y_{impact} = \left(y_{\mathbb{C}_L\ Refl} + \delta y \cos 45^\circ\right)$$

$$z_{impact} = z_{\mathbb{C}_L} + \delta z.$$

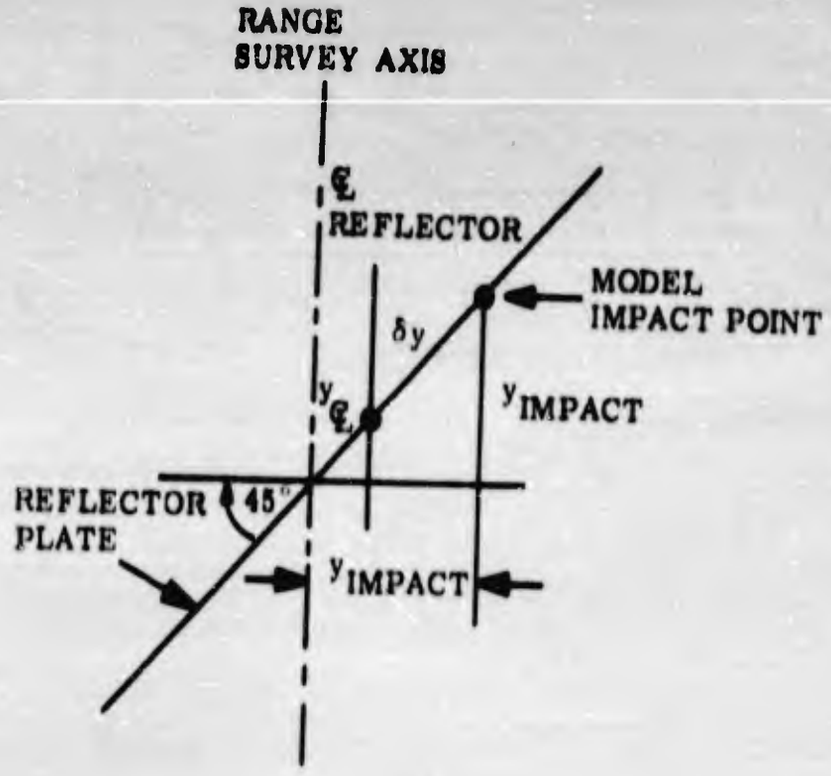

Fig. 6-1 Coordinates of Model Impact on Reflector Plane

SECTION VII
FLASH X-RAY PHOTOGRAPHY

Flash radiography techniques are being used on the physics range to study the behavior of the in-flight projectile. Fractional, microsecond-pulsed radiographic techniques permit the observation of the projectile in flight, thus determining the integrity of the projectile subsequent to launch. A knowledge of the integrity of the projectile is of utmost importance, since a model damaged in flight usually renders the radiation and radar data useless.

A typical flash radiograph obtained for the case of a copper-capped plastic model at 14,000 ft/sec in an atmosphere of 10 mm Hg of air is shown in Fig. 7-1. Here the copper cap is clearly distinguishable from the plastic body, showing the integrity of the model. Because of the intense G-loading at launch, it is possible to have the metal cap separate from the plastic body. Since this separation may amount to no more than a few thousandths of an inch, it cannot be observed with the spark photography techniques used at the six velocity stations. Flash radiographs, however, offer a clear, well-defined shadowgraph of the model in flight and can differentiate, by virtue of the varying absorption properties of different materials, between the elements of the model.

The flash X-ray equipment is mounted approximately 1 ft upstream of the radar deflector in the radar tank at the end of the range. In this position, the equipment photographs the model at the end of its flight path with good precision, eliminating any conjecture as to whether the model may have broken up after passing the velocity spark photograph stations while still undamaged. A single-channel, pulsed, flash X-ray

unit is employed. The equipment operates at 100,000 volts, 1400 amperes, and has an exposure time of 0.07 microsecond. The short duration of the pulsed radiation obviates any motion of the projectile during exposure and furnishes the definition and resolution required for these tests.

Fig. 7-1 Flash X-ray Photograph of Copper-Capped Plastic Model, V = 14,000 ft/sec, p = 10 mm Hg, Air

SECTION VIII
SCHLIEREN SYSTEM

In order to produce photographs of the model's shock-wave pattern and wake, a high sensitivity schlieren system of the double-pass coincident type is used. The major elements are shown in Fig. 8-1.

The light source is a spark gap with a 0.015 in. diameter aperture. Discharge time is 0.1 – 0.2 microsecond, triggered from a photobeam. The windows are Cenco #44341-2 cover glasses, selected for parallelism by examining the fringes under monochromatic light. A front-surfaced-prism mirror which divides the entering and emerging beams can be adjusted for a minimum beam separation of 0.025 in. The spherical mirror, 11.5 in. in diameter with a 5-ft. focal length, is located inside the flight chamber a few inches off the trajectory in order to obtain maximum resolution. Optical tolerance on both the spherical and the prism mirror is 1/10 wavelength of sodium light. The knife edge is a blackened, single-edged razor blade of the injector type. Both the knife edge and the spark light source are suspended from three-dimensional micropositioners and can be adjusted to better than 0.001 in.

Either a 24- or a 40-in. Aero-Ektar lens may be used with the Brand 17 Universal camera. The Graphloc camera back will take either Polaroid roll film or 4 by 5 cut film. In actual practice, Polaroid Type 47 film is used to make the final adjustments, and the data picture is taken on a 4 by 5 Royal-X-Pan which is developed for maximum contrast.

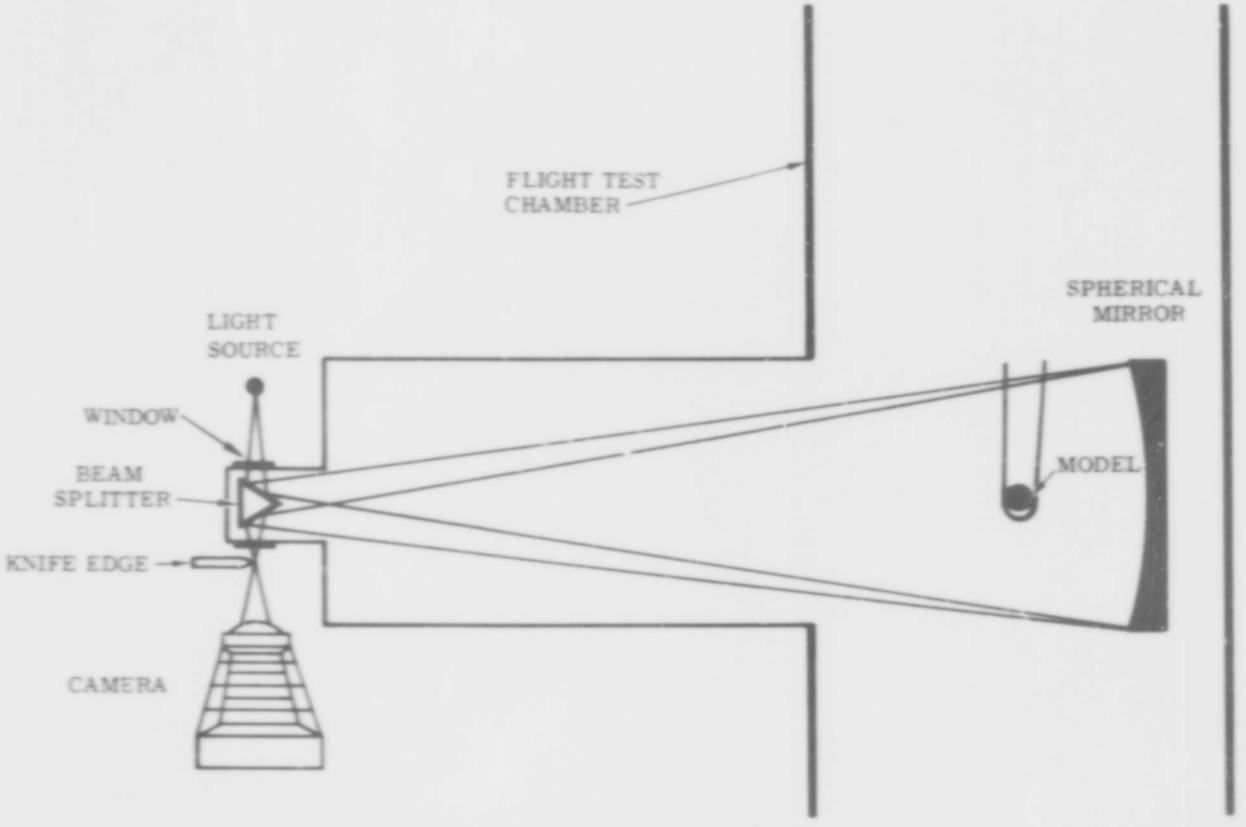

Fig. 8-1 Schematic of High Sensitivity Schlieren System, Double-Pass Coincident Type

The light-source trigger may be delayed to take pictures of the wake as far behind the model as it is visible. One such schlieren camera is in use on the range and another can be added at short notice. It is estimated that the lower limit of the ability of the schlieren system to resolve the wake is of the order of 10 mm of Hg pressure. Figure 8-2 shows a typical schlieren photograph taken with the system.

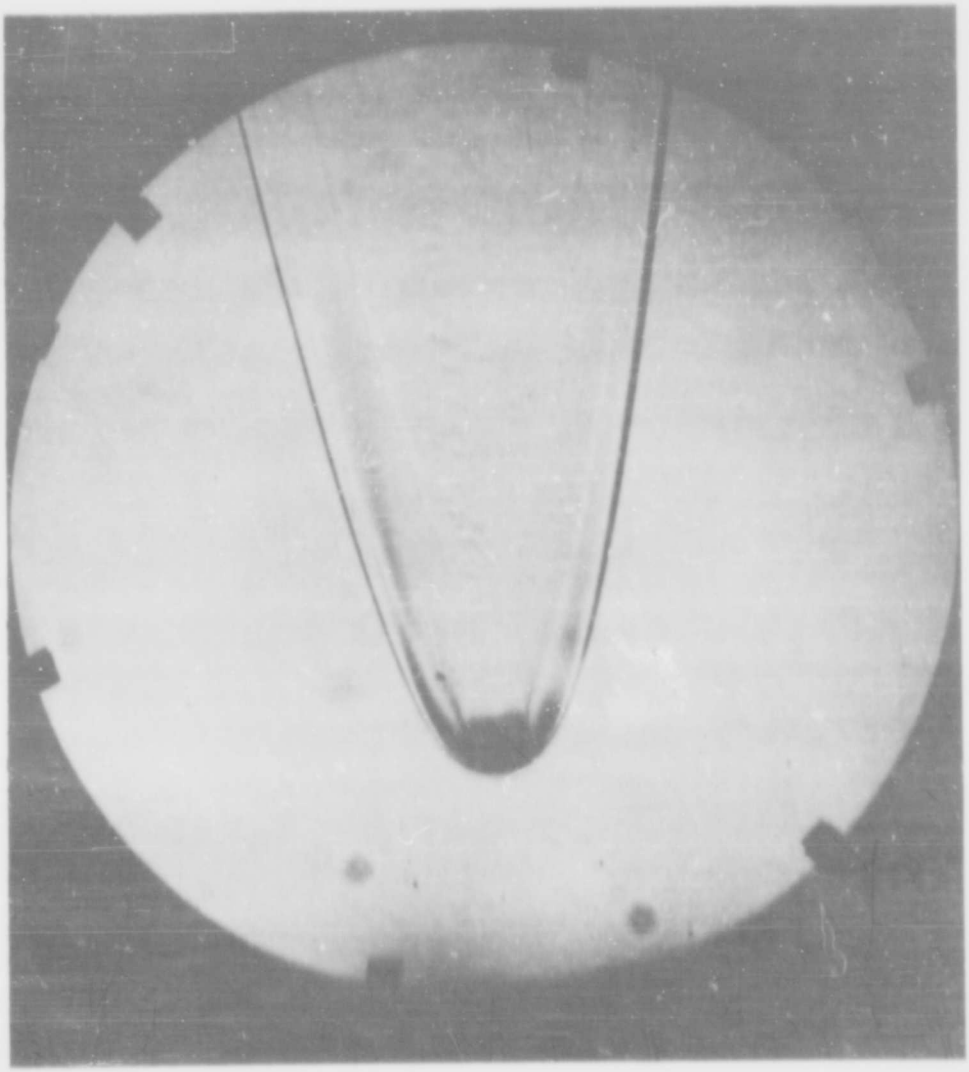

Fig. 8-2 Typical Schlieren Photograph

SECTION IX
OPTICAL RADIATION MEASUREMENTS (ULTRAVIOLET, VISIBLE, NEAR INFRARED)

Range station A consists of two sets of multiple-viewing ports placed around the trajectory (Fig. 9-1). Multiplier phototubes are mounted over these ports to measure the intensity of the radiation from the near flow field and from the wake of the model. A single sh..dowgraph system provides a picture of the condition and attitude of the model, and measurements are initiated by a photobeam trigger.

The geometry of the recording apparatus and two typical records are shown in Fig. 9-2. Collimating slits placed between the model and the photomultipliers limit the field of view to 0.3 in. along the trajectory and 6 in. normal to it. The window, of Corning #7940 fused silica, U-V grade, transmits radiation down to about 1,800 Angstrom units, (0.18 μ).

Three standard Dumont multiplier phototubes cover the spectral range from 2,000 – 10,000 Angstrom units: type 7664 is responsive from 2,000 – 5,500 Angstrom units; type 6292 from 3,500 – 5,500 Angstrom units; and type 6911 for the infrared region from 3,500 – 10,000 Angstrom units.

The signals are measured by a Tektronix Type-535 oscilloscope using Type H preamplifiers and are recorded on Polaroid film. A Universal Telereader transfers the data to punched cards for automatic processing.

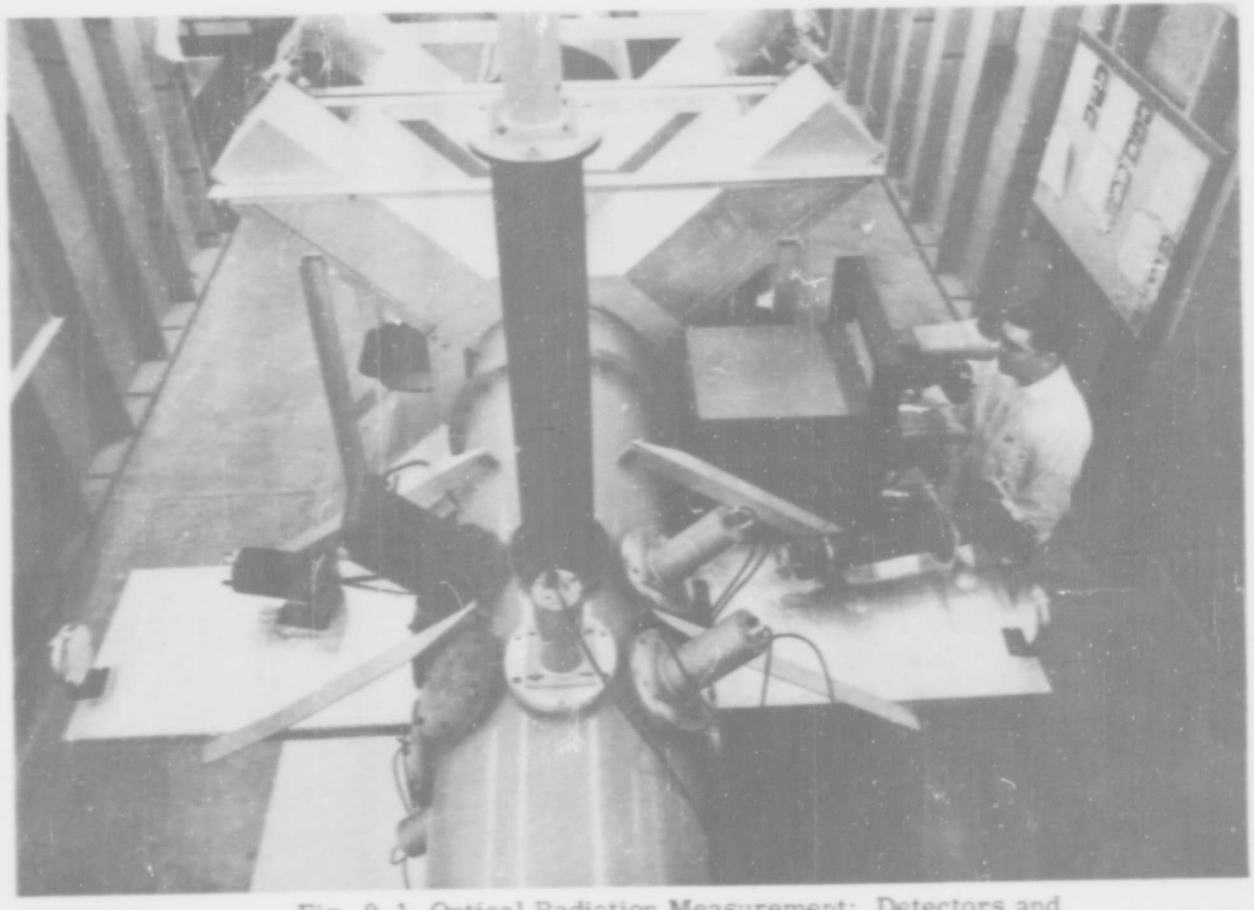

Fig. 9-1 Optical Radiation Measurement: Detectors and Schlieren Photographic Station

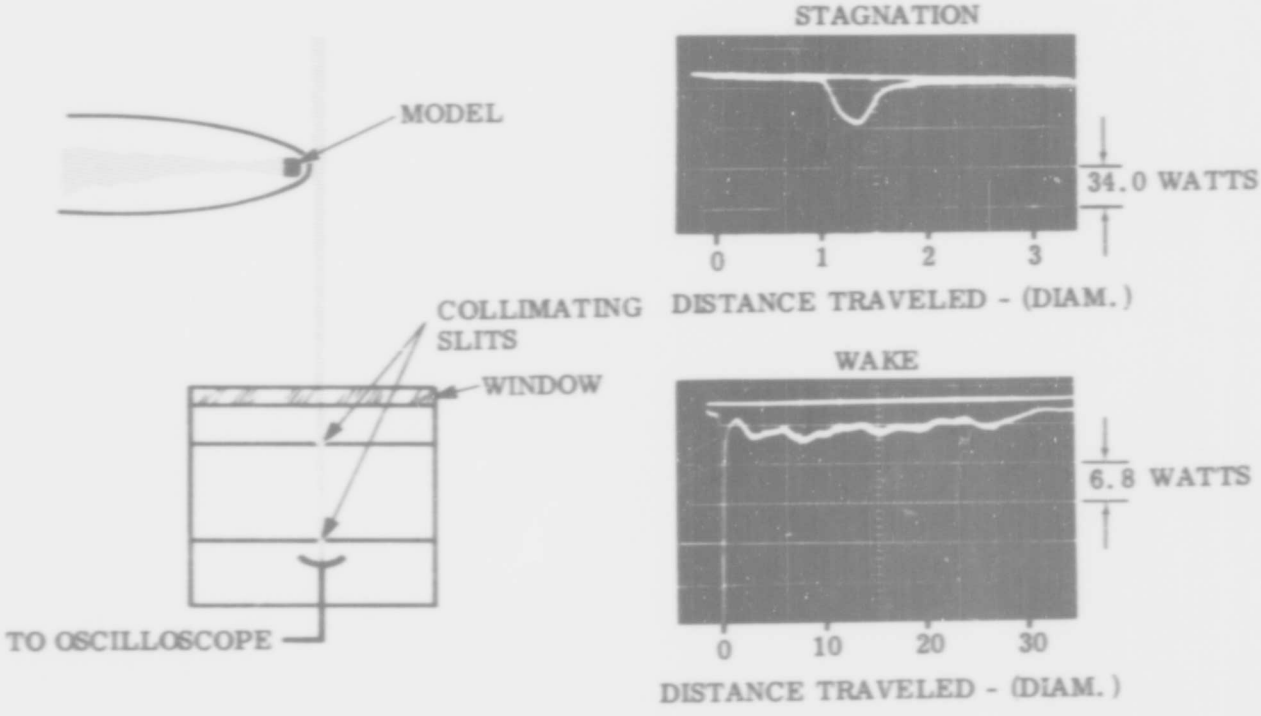

Fig. 9-2 Optical Radiation Measurement: Schematic and Typical Records (V = 25,000 ft/sec; p = 20 mm Hg; Air; 2,000 A < λ < 5500 Å; 5,500 A; Polyethylene Standard Model)

CALIBRATION AND DATA REDUCTION METHODS

The multiplier phototubes are calibrated by measuring their output when illuminated by a known radiant energy flow from an NBS tungsten-ribbon-filament lamp. The lamp is operated on 0.5 percent regulated AC and is allowed to stabilize before use. An aperture with cross section A is used to mask the filament so that the level of radiation does not saturate the photomultiplier, and so that edge effects of the filament are eliminated. The photomultiplier, placed a known distance d from the tungsten filament, is also masked with an aperture of cross section A_2.

The spectral radiance of the standard source $S(\lambda)$ is given in microwatts per (sterad - mm^2 filament area - millimicron of spectrum) as a function of the wavelength λ for several different filament current values. The intensity which reaches the phototube in the wavelength interval $d\lambda$ is

$$dI = S(\lambda) \frac{A_1 A_2}{d^2} d\lambda \qquad (1)$$

This function is multiplied by the spectral response function of the photomultiplier $f(\lambda)$ and integrated over the entire spectrum to get the total effective intensity of light seen by the detector.

$$I_{eff.} = \int_0^\infty \frac{dI}{d\lambda} f(\lambda) d(\lambda) \qquad (2)$$

The total circuit sensitivity s for a given photomultiplier supply voltage and terminal impedance is the output voltage V, across the impedance,

per unit of I_{eff},

$$S = \frac{V}{I_{eff}} \tag{3}$$

When the detector is subsequently used to measure radiation from an unknown source (such as the gas-cap radiation about a model), the total effective intensity is

$$I_{eff} = \int_0^\infty \frac{dI}{d\lambda} f(\lambda) f_w(\lambda)\, d(\lambda) \tag{4}$$

This is the same as Eq. (2), except that now the spectral distribution $\frac{dI}{d\lambda}$ is from the unknown source rather than from the standard lamp; and the extra factor $f_w(\lambda)$ accounts for a transmission loss due to a window (between the detector and the source) which was absent in the calibrations.

If the response function $f(\lambda)$ covers only a narrow band, it is assumed that the spectral distribution is relatively constant over the band.

$$\frac{dI}{d\lambda} = \frac{I_{1,2}}{\lambda_2 - \lambda_1} \tag{5}$$

where $I_{1,2}$ is the desired quantity — the total radiation emitted in the band from λ_1 to λ_2. In this case,

$$\frac{I_{eff}}{I_{1,2}} = \frac{\int_0^\infty f(\lambda) f_w(\lambda)\, d(\lambda)}{\lambda_2 - \lambda_1} = \bar{f} \tag{6}$$

then

$$I_{1,2} = \frac{\int_0^\infty \left(\frac{dI}{d\lambda}\right)_s f(\lambda)\, d(\lambda)}{\bar{f}} = \frac{V}{V_0} = \frac{V}{s\bar{f}} \qquad (7)$$

where the subscript s refers to the calibration conditions. That is, V/V_s is the ratio of the voltage output, when measuring the unknown source, to the voltage output when measuring the standard source, which has the known spectral distribution $(dI/d\lambda)_s$. It is seen that the function $f(\lambda)$ may be given in any arbitrary scale as long as the same scale is used in both calibration and reduction of the data, since the scale factors cancel out in the ratio given by Eq. (7).

Where the accepted bandwidth is rather broad, the data may be reduced using response functions weighted with the intensity distributions predicted from theory.

$$\frac{I_{eff}}{I_{1,2}} = \frac{\int_0^\infty \frac{dI}{d\lambda} f(\lambda) f_w(\lambda)\, d\lambda}{\int_{\lambda_1}^{\lambda_2} \frac{dI}{d\lambda}\, d\lambda} = \bar{f} \qquad (8)$$

and then the value of $\bar{f}$ given by Eq. (8) is used to calculate the total radiation $I_{1,2}$ from measured voltages as given in Eq. (7). The factor $\bar{f}$ is a function of velocity and range pressure, as well as of bandwidth, in this case.

SECTION X
INFRARED RADIATION INSTRUMENTATION

The infrared emission from the gases about hypersonic bodies is being measured in the free-flight range. The object of this phase of the study is (1) the determination of the infrared contribution to the total radiation, and (2) a determination of the possible contribution of the 4.3 micron CO_2 band radiation to the infrared signature of the wake flow.

FAR INFRARED

The infrared radiometer module being employed is shown in Fig. 10-1. The module bolts onto a 6-in. flanged opening in the top of the range, and the detectors are mounted in a row perpendicular to the flight line. Three such modules, each capable of holding four detectors, are available. The detectors are mounted above calcium fluoride windows, 1 in. in diameter, which are sealed in the flange cover plate with O-rings. Filters to select particular bandwidths can be mounted in a recess above each window.

Two slit plates located in the range atmosphere below the flange cover plate, are used to define the fields of view of the detectors. Several slit-plate combinations are available to permit easy modification of the field of view as required.

Philco series ISC-301 photovoltaic indium antimonide detectors are currently being used. The spectral sensitivity of the detectors is shown in Fig. 10-2. The detector has a rise time of less than 1 microsec, and the signal response is linear up to flux densities of 1000

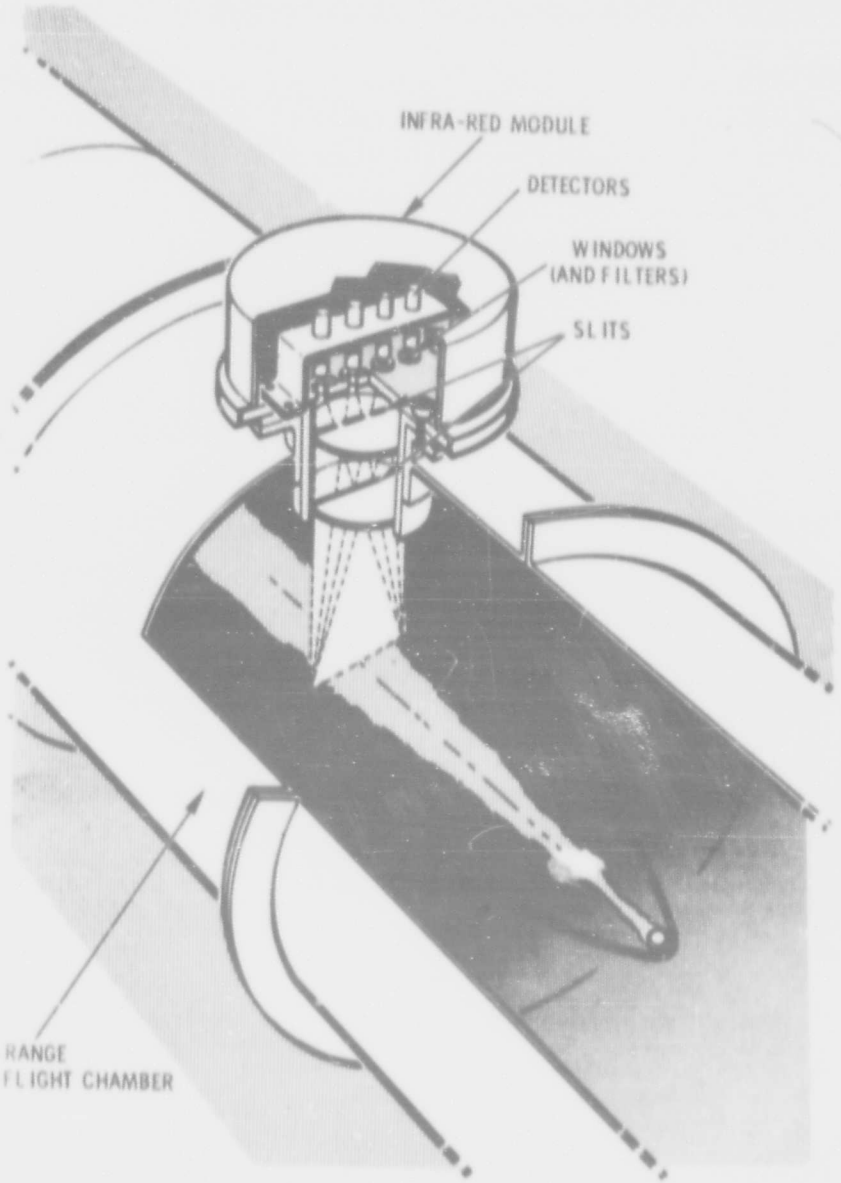

Fig. 10-1 Measurement of Radial Radiation Distribution

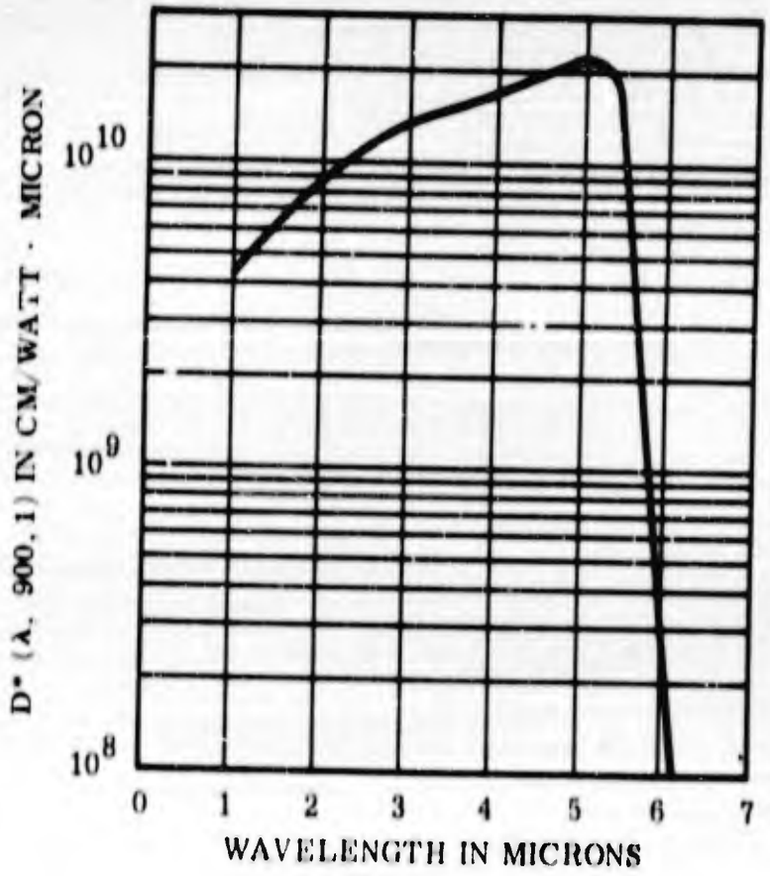

Fig. 10-2 Typical Absolute Spectral Response at 77°K for ISC-301 With $D^*(500, 900, 1) = 5 \times 10^9$ cm/watt

micro-watts/cm^2. The sensitive area has a diameter of 0.09 in. and is sealed in a dewar behind a sapphire window. The cell is cooled to -196°C with liquid nitrogen.

The output of the detector is amplified using a low-noise video amplifier with a voltage gain of approximately 50 from 200 cps — 5 Mc. The rise time of the detector-amplifier combination has been monitored using a Strobotac pulsed light source. For light pulses having rise times of less than 0.3 microsec, the amplified output of the infrared system was almost identical to the output of a photomultiplier in rise time. The amplifiers are mounted within the radiometer module adjacent to the detectors. Amplified outputs are displayed on Tektronix 551 oscilloscopes and recorded with Polaroid Land Cameras. The sweeps of the oscilloscopes are triggered by the output of a light-screen trigger station (described later) located 1 in. upstream of the first infrared detector station.

Two modules are presently in operation: the first has a single detector located directly above the flight line; the second has four detectors as shown in Fig. 10-1.

The single detector in one module, and one of the detectors in the four-unit module, see the event through calcium fluoride windows. Broad-band filtered radiation in the intervals 2-3, 3-4, and 4-5 microns are monitored by the other three detectors in the multiple module. The transmission of the interference filters (Infra Red Industries) are shown in Fig. 10-3. The filters show no detectable transmission outside of the specified wave length regions within the sensitive range of the detectors.

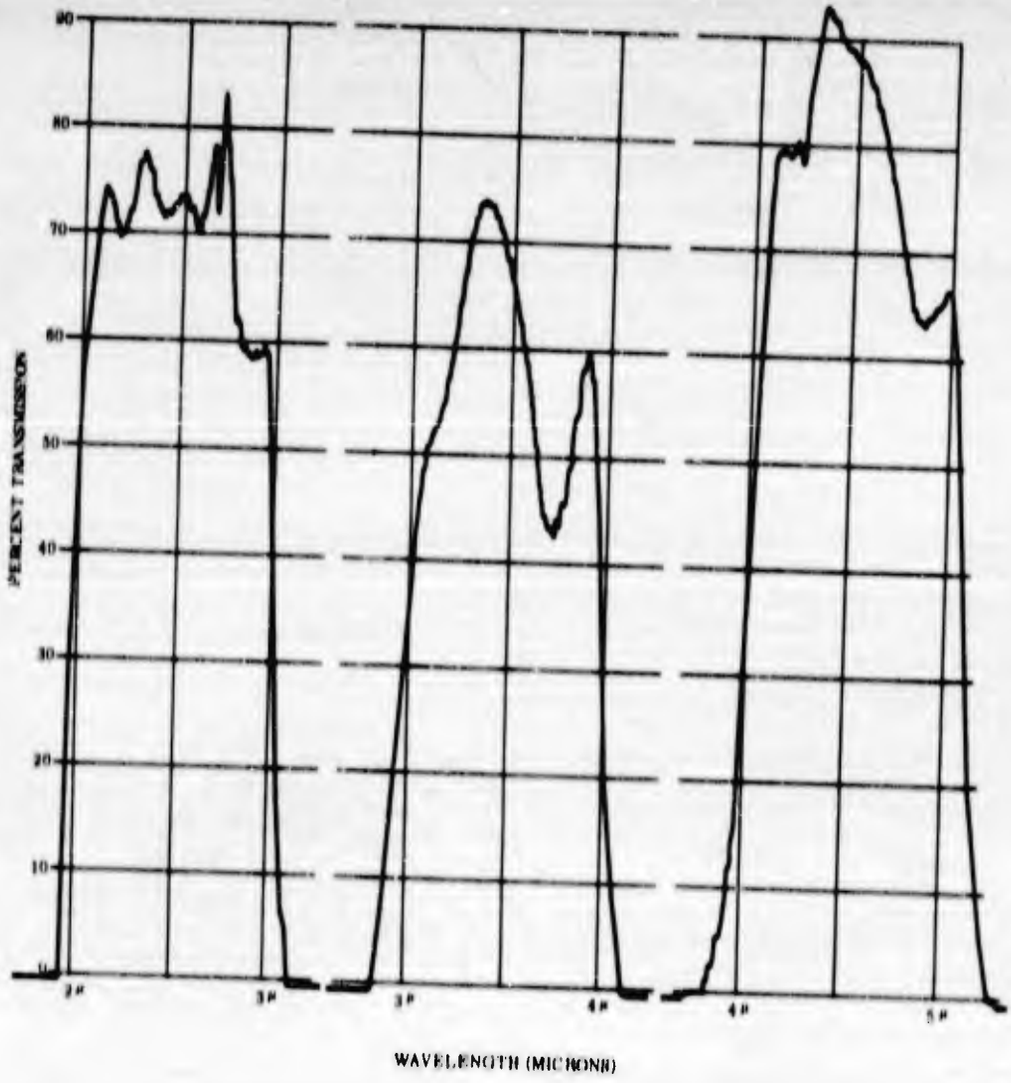

Fig. 10-3 Broadband Filter Spectral Transmission

The slit pairs for all of the detectors have been adjusted for the same field of view. The field is 4.5 in. wide and perpendicular to the flight line. Along the flight line, the field is 0.68 in. at the half-intensity point, ranging from 0.595 in. for the umbra to 0.76 in. for the penumbra. As radiation intensity increases with increasing flight velocity or the introduction of contaminants, the field of view will be decreased along the flight line. If there is sufficient intensity, the field will be monitored with a "fence" as shown in Fig. 10-1.

METHOD OF CALIBRATION

The IR optical system is calibrated against a blackbody source. The radiometer module is removed as a unit from the range and located above the aperture of a blackbody source (Infra Red Industries Model 406). The blackbody aperture is positioned the same distance from the detectors as is the flight line in the range. In this way, the geometrical optics and field of view, as well as the spectral response of each detector unit, is reproduced in the calibration. The blackbody radiation is chopped at 500 cps, and the amplified outputs of the detectors are displayed on the oscilloscopes and recorded.

The blackbody temperature and aperture, along with the slit-system geometry, determine the radiant flux incident on the window-filter-detector combination. The oscilloscope output then allows the calculation of the sensitivity of each filter-detector-amplifier system.

In order to guarantee that the system response is flat at the chopping frequency, the chopper disc rotation rate is decreased and the amplitude of the modulated output is monitored. The signal amplitude remains constant down to a few hundred cycles per second for all of the indium-antimonide detector systems. The responses of the

detectors were checked and found to be linear well beyond the 1000 micro-watts/cm^2 specified by the manufacturer.

METHOD OF DATA REDUCTION

A schematic drawing of the optical system is shown in Fig. 10-4. Both slits have the same width, W. The length L and position S_1 of the first slit determine the field of view perpendicular to the flight line at a distance d from the detector. The width W and position S_2 of the second slit determine the field of view along the flight line. The half-intensity point in the penumbra may be used to define the field of view along the flight line. For any point in the field of view of the detector, the solid angle Ω_d subtended by the detector is given by

$$\Omega_d = \frac{a}{d^2}$$

where a = area of sensitive element of detector.

During calibration, the weighted spectral power $\bar{I}_c$ in the wavelength region λ_1 to λ_2 to which the detector responds is

$$\bar{I}_c = A_b \Omega_d \int_{\lambda_1}^{\lambda_2} I_b R_\lambda T_\lambda \, d\lambda$$

where A_b = the area of the source intersected by the field of view of the detector

R_λ = responsivity of the detector at wavelength λ (see Fig. 2)

T_λ = transmissivity of the window-filter combination at wavelength λ

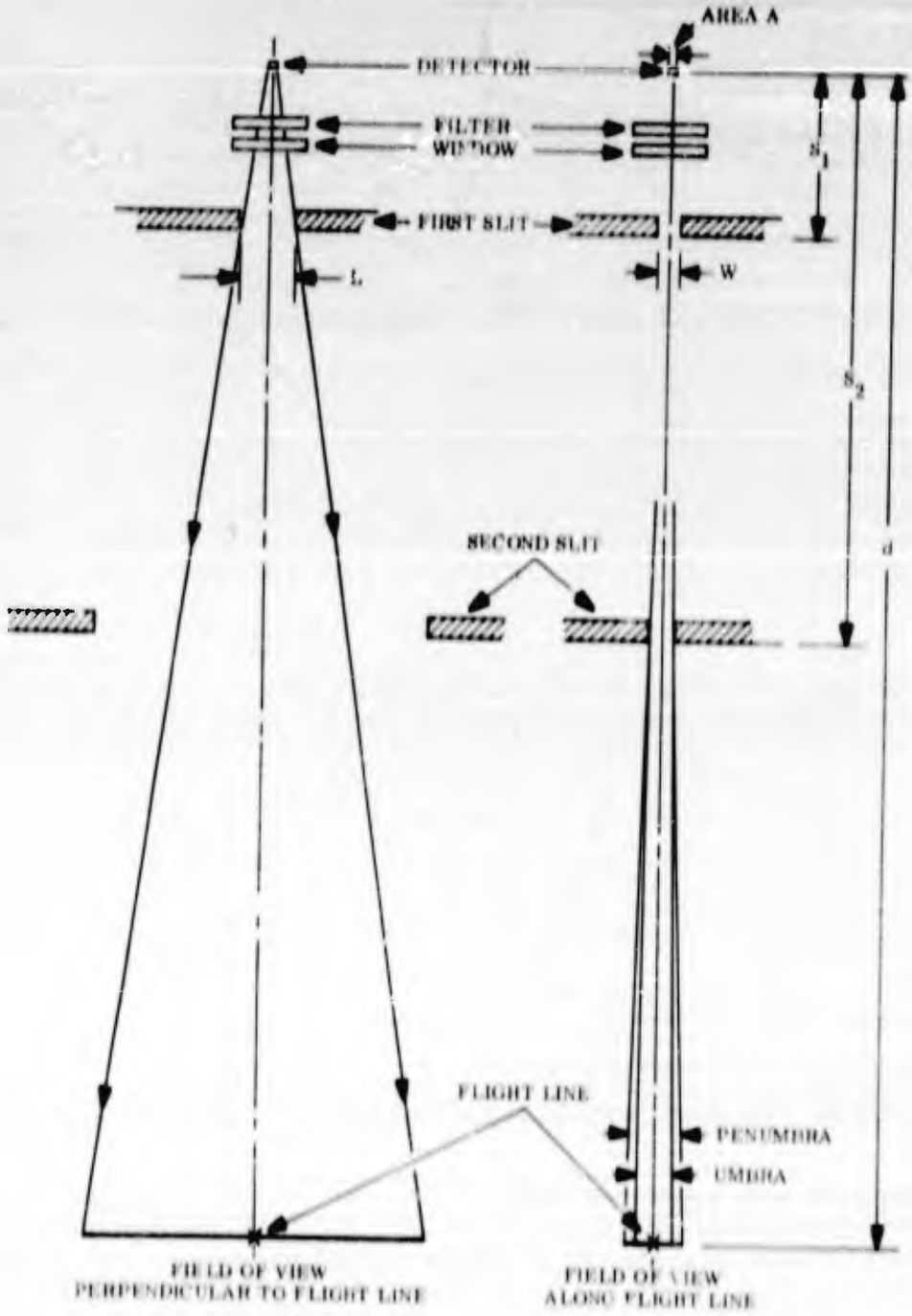

Fig. 10-4 Infrared Optical System

and $I_b = \frac{c_1}{\pi \lambda^5}\left(e^{-c_2/\lambda T} - 1\right)^{-1}$ is the blackbody

spectral radiance of the source at temperature T. This is given in watts/cm^2/ster normal to the source/cm wavelength when $c_1 = 3.742 \times 10^{-12}$ watts/cm^2 and $c_2 = 1.439$ cm^{0}K.

Now the output voltage E_c from the detector during calibration is proportional to the weighted spectral radiance $\overline{I}_c$. Thus,

$$E_c = \frac{1}{g} \overline{I}_c$$

where g = calibration factor

During an actual range test, a detector is found to record a voltage E_t at a particular instant. Then the weighted intensity $\overline{I}_t$, incident upon the detector from the event at that instant is given by

$$\overline{I}_t = g E_t$$

where g is the calibration factor of the detector concerned. The analysis can be carried one step farther by assuming tha the spectral distribution is flat within the measured wavelength interval λ_1 to λ_2. With this assumption the total radiated power I_d incident on the detector is

$$I_d = \frac{\overline{I}_t(\lambda_2 - \lambda_1)}{\int_{\lambda_1}^{\lambda_2} R_\lambda T_\lambda \, d\lambda}$$

Also, assuming that the gases about the model are optically thin, the total radiation intensity between wavelength λ_1 and λ_2 is

$$\frac{I_d}{\Omega_d}(\lambda_2 - \lambda_1) \quad \text{watts/sterad}$$

If the emission can be associated with any particular volume V of the gas, the total radiation intensity in the internal λ_1 to λ_2 can be expressed as

$$\frac{I_d}{\Omega_d V} \quad \text{watts/cm}^3\text{/sterad}$$

SECTION XI
TRANSVERSE PATH MICROWAVE ABSORPTION

INSTRUMENTATION AND DATA PEDUCTION PROCEDURE

INTRODUCTION

A major observable in the wake of a hypersonic velocity projectile is the ionization, which is characterized by electron density and collision frequency. Since ionization has a profound effect on radar tracking and discrimination of reentry bodies, it is important to be able to study this observable behind projectiles under controlled conditions.

This report will describe focused microwave probes which operate at 35 Gc/s and 70 Gc/s, and which are now in use to determine the magnitude and spatial distribution of electron density and collision frequency. Each probe employs six to seven adjacent beams which are stacked in a plane normal to the flight path to form a fence across the wake. Brief descriptions will be given of earlier versions of this equipment from which useful information has been obtained. The general properties of the focused antennas will be outlined and the specific performance figures will be given. The microwave circuitry will be dealt with in detail, and the discussion will include methods of operation and calibration.

Methods of recording, analyzing, and interpreting data will be discussed in detail; a typical record will be analysed.

The range of electron densities which can be measured accurately is about 10^{10} - 10^{13} e/cc. The maximum available resolution is about 1/4 in.

GENERAL APPROACH

The determination of the properties of an ionized wake involves a number of assumptions and procedures, outlined below and subsequently discussed in detail.

a. The amplitude and phase of the signal transmitted through the wake are measured.

b. Each microwave beam is focused to ensure the passage of as mu ' ' the energy as possible through the wake and to approx- ima' physical situation to the idealized case of a plane wave normally incident on a parallel-sided slab of uniform plasma.

c. If it is assumed that the conditions in b., above, are satisfied and that the wake is underdense, then measurements of the transmitted signal amplitude and phase can be interpreted in terms of average electron density and collision frequency.

d. If several, independent, adjacent beams in a plane normal to the trajectory are used, and if the measured transmission coefficient of each beam is interpreted as in c., above, then it is possible to determine the spatial distribution and magnitude of electron density and collision frequency in the wake.

Measurement of Transmitted Signal

A complete determination of the ionization properties of a plasma slab requires, in addition to knowledge of the slab dimensions and the spatial distribution of ionization within the slab, the measurement of both magnitude and phase of the signal transmitted through the slab for an incident, uniform plane wave. In the case of an underdense plasma, it will be shown that the reflected wave can be ignored. Consequently, in all that follows it is assumed that the only quantities which will be measured directly are the amplitude and phase of the transmitted wave.

Focused Microwave Apertures

Some of the pertinent features of focused apertures will be outlined here. Since the subject would require a lengthy treatment, any additional information will have to be obtained from the literature.

When an aperture is illuminated with microwave energy in such a manner as to cause focusing of the reradiated energy at a finite distance from the aperture, the effect of this focusing is to reproduce, in the focal plane, a replica of the far field produced by the same aperture when focused at infinity. An aperture focused at infinity is operating in the familiar far-field mode. Under the above conditions, the angular dimensions of the beam are preserved, whether the aperture is focused at infinity or in a plane which is at a finite distance from the aperture.

To consider a specific example, take the case of a circular aperture, of radius a, which is uniformly illuminated. The phase across the aperture is constant. The far-field pattern is:

$$E(u) = K \frac{J_1(u)}{u} \qquad \text{for } R \geq \frac{2(2a)^2}{\lambda} \text{ and } \frac{a}{\lambda} >> 1 \qquad (1)$$

K is a constant

$u = ka \sin\theta = \frac{2\pi}{\lambda} a \sin\theta$

λ = wavelength

θ = polar coordinate of the pattern

R = range from the aperture

If the same aperture were now focused at a finite distance f from the aperture, the field pattern in the focal plane would again be given by Eq. (1), with R = f. In either case the dimensions of the beam in terms of length rather than angle is given by Fig. 11-1

$$\tan \theta_1 \cong \frac{x_1}{R} \qquad \text{unfocused case}$$

$$\text{and } \tan \theta_2 \cong \frac{x_2}{f} \qquad \text{for the focused case}$$

and since the angular dimensions are preserved,

$$\tan \theta_1 = \tan \theta_2$$

$$\text{or } \frac{x_1}{R} = \frac{x_2}{f}$$

Also, equating R to its minimum value, $\frac{8a^2}{\lambda}$

$$\frac{x_1}{x_2} = \frac{8a^2}{\lambda f} \tag{2}$$

Now it can be shown in a general way that for apertures which have "smooth" (defined to exclude super-gain antennas) phase distributions, maximum focusing (smallest focal spot size) is achieved for 2a = f. Substituting in Eq. (2),

$$\frac{x_1}{x_2} = \frac{2f}{\lambda} = \frac{4a}{\lambda} \tag{3}$$

This ratio represents the amount by which the linear transverse dimensions of the beam can be decreased by focusing. It can be seen that for short wavelengths considerable reductions in dimensions are possible. The physical dimensions of a beam are usually given at the 3-db point. In this case,

Fig. 11-1 Radiation from a Circular Aperture

$$\tan \vartheta_1 \cong \frac{\lambda}{2a}$$

$$\text{or} \quad \frac{\chi_1}{R} = \frac{\chi_1}{\frac{\vartheta a^2}{\lambda}} = \frac{\lambda}{2a}$$

$$\text{or} \quad \chi_1 = 4a$$

So, from Eq. (2),

$$\chi_2 = \frac{f}{2a} \lambda \tag{4}$$

This is one of the most important results applicable to the use of focused beams in plasma diagnostics. It is immediately obvious that for maximum focusing (i. e., f = 2a) $x_2 = \lambda$. This represents the smallest physical dimensions that can be produced by conventional focusing techniques.

It can be shown more generally that if the illumination across the aperture is tapered, x_2 is given by

$$\chi_2 = \kappa \frac{f}{2a} \lambda \tag{5}$$

K depends on the amplitude distribution over the aperture.

For uniform illumination, K = 1

For optimum illumination, K ≈ 1.5 (to be discussed).

The detailed field distributions in the focal plane have been considered in Ref. 2.

Although the field distributions are important in estimating the dimensions of focused beams, the distribution of energy-flow through the focal plane is far more important in evaluating the effectiveness of a focused system, because it is this energy distribution which determines the percentage of the transmitted power that has flowed through a plasma of finite size located in the focal region. In this regard, the receiving antenna is just as important as the transmitting antenna, since its directivity pattern has a direct influence on the amount of power received and on the origin of this power in relation to points in the focal plane.

The power transmission between two identical, circular apertures, symmetrically located on opposite sides of a common focal plane, has been examined in detail (Ref. 2). The percentage of this power which passes through an arbitrary-sized circular area in the focal plane, as a function of arbitrary illumination functions over the transmitter aperture, has been evaluated. Some of the important results are shown in Fig. 11-2.

The error represents the amount of energy which does not flow through the circular area of diameter D compared with that which does. This can be related to a diffraction error encompassing, say, a cylindrical,

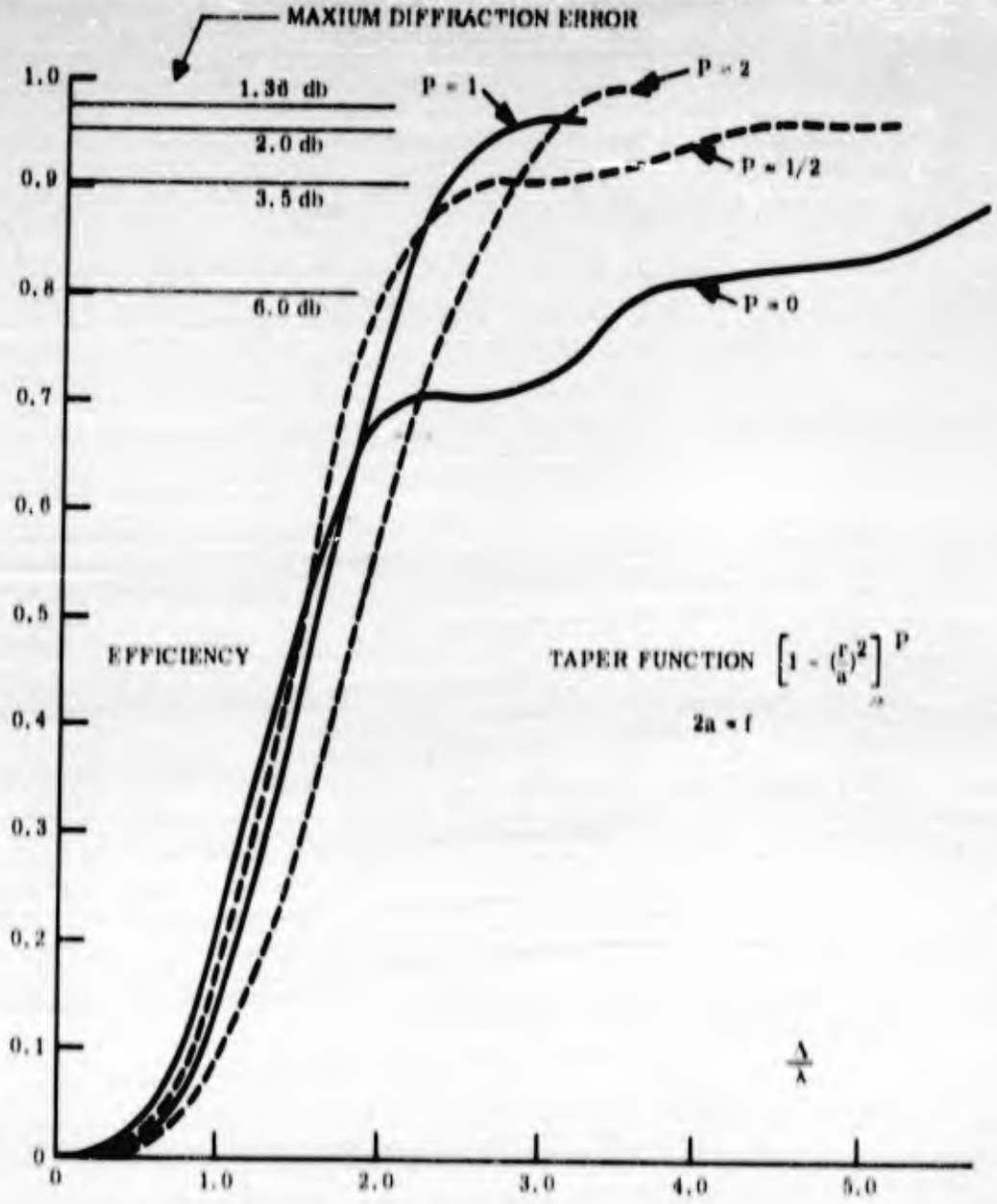

Fig. 11-2 Overall Efficiency of Two Focused Lenses with a Variable Aperture Stop in the Common Focal Plane

ionized wake whose axis lies in the focal plane, by equating the diameter D of the circular area to that of the cylinder.

It is immediately apparent that the use of uniform illumination incurs intolerable diffraction errors. It may also be inferred that the use of non-focused microwave beams results in prohibitive errors, and the only way in which such a probe may be used with confidence is to interpret the results in terms of a rigorous solution of the diffraction problem. According to Fig. 11-2, the diffraction error may be held within reasonable limits by tapering the illumination over the transmitter aperture. In fact, an optimum taper exists in that the error can be minimized for a certain diameter D by choosing a certain taper function.

As an example, it is found that for $D = 2.25\lambda$ and $p = 1$, about 90% of the transmitted power passes through this circle. The amount of energy passing outside of this circle is about 10% and can cause unwanted interference effects of up to 35 db. It is evident that if ionized columns with diameters of the order of several wavelengths are to be measured, it will be necessary to use strongly focused beams and optimum illumination.

The longitudinal field and power distributions are of interest if the ionized region has some finite extent in a direction normal to the focal plane. These distributions are usually less tractable than the transverse, and only a few special cases have been treated.

Born and Wolf (Ref. 3) have examined the focal region of a uniformly illuminated circular aperture in some detail, and Mathews and Cullen (Ref. 4) have examined the focal region of a square aperture

with both uniform and non-uniform illumination. In neither case was the effect of a receiving antenna included. In general, it is found that the field in the longitudinal direction is more extended than that in the transverse direction. In particular, for uniform illumination, zeros of field strength exist along the axis. However, for $f = 2a$, the 3-db points along the longitudinal axis are separated by a distance which is roughly four times that along the transverse axis. Since $f = 2a$ represents a condition of maximum focus, this transverse dimension is about 1λ, so the depth of focus is approximately $2 \times 4\lambda = 8\lambda$.

Tapered illumination has a major effect on the longitudinal field variations. Where the taper is close to optimum, the fluctuations virtually disappear and the field is monotonic on either side of the focal plane. If optimum illumination is used, the dimension of the transverse 3-db points is 1.5λ, and the depth of focus is greater than $2 \times 6.0\lambda = 12\lambda$.

The longitudinal field variations impose a loosely defined maximum trail diameter, whereas the diffraction error imposes a minimum trail diameter for use in a focused system. Accepting a 3-db diffraction error as tolerable, it is found that

$$2.25\lambda \leq D_T \leq 12\lambda \qquad (6)$$

An extremely interesting feature of the focal region field is that at distances from the focal plane which lie within the "depth of focus", the constant phase contours are planes approximately parallel to the focal plane. It is this feature which justifies the assumption of plane-wave incidence on the plasma.

An additional characteristic of the field in the focal region that may have to be taken into account is that the wavelength near the focus is

longer than the free-space wavelength. For uniform illumination the difference is about 8.5 percent and is correspondingly less for tapered illumination. It is found for underdense plasmas that this correction is unimportant.

In the foregoing arguments it has been assumed that, although a cylindrical ionized column is present in the focal region, the field distribution would not be perturbed if the column were absent. These arguments have been concerned with minimization of diffraction errors and idealization of the actual illumination in the vicinity of the plasma – all based on geometrical consideration. However, a real plasma can result in major perturbations of the focused field. The main desired perturbation is in the transmission coefficient from which the plasma parameters may be determined. However, an undesired perturbation could be caused by refractive effects and result in deviative absorption, or defocusing. Since the latter effects would be extremely difficult to interpret, it is important to determine the conditions under which refraction would be negligible. With this in mind, theoretical studies have been carried out (Refs. 6, 7). Two distinct cases have been examined.

In one case (Ref. 6), a finite slab of uniform plasma is located about the focal plane. For an underdense plasma, it is found that the transmission coefficient is identical to that which would be obtained for uniform plane-wave incidence on the same slab. This result is remarkable in that the non-uniform nature of the incident wave and the variation of wavelength are inherent in the analysis. It is a straightforward justification of the assumption asserted previously that the waves which propagate through the plasma are plane waves.

In the second case (Ref. 7), the effect on the transmitted wave of a uniform, cylindrical column, with its axis in the focal plane, is determined. Closed-form solutions are obtained and can be interpreted fairly simply, either for very small cylinders or for large cylinders (say, $D \gg 10\lambda$). For small cylinders the transmission coefficient can be related to the plasma properties but not in the same way as for a slab. For large cylinders (greater than 10λ) the results reduce to those for a slab. For intermediate sizes the results are more complex, but they can be computed in any given case.

The Interaction of a Plane Electromagnetic Wave with a Plasma Slab

The geometry of a focused beam which interacts with a cylindrical plasma can be approximated by that of a uniform plane wave incident on a uniform, parallel-sided plane slab. The interaction in either case will appear identical, provided that the plasma is underdense. It remains to be shown how the amplitude and phase of the transmitted wave may be related to the plasma properties. This will be done for the idealized case of a uniform, plane wave, normally incident on the slab. (See Fig. 11-3.) All waves are plane-polarized (in XY plane). A wave in the positive direction is written in the form,

$$\vec{e} = \vec{E} \exp(-\gamma z) \exp(j\omega t)$$

where

$$\gamma = \alpha + j\beta$$

For free space, $\alpha_0 = 0$ and $\gamma_0 = j\beta_0 = j\frac{2\pi}{\lambda_0}$

λ_0 is the free-space wavelength.

ω is the angular operating frequency.

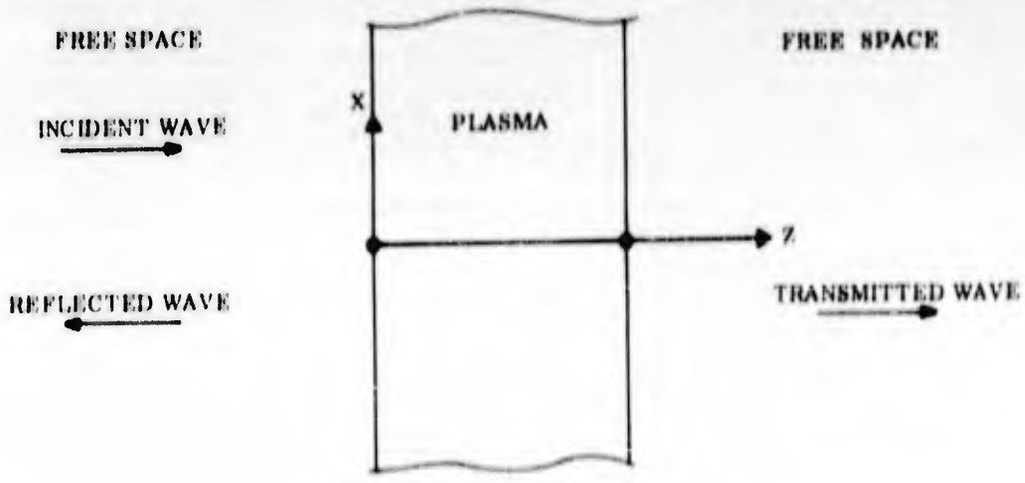

Fig. 11-3 Uniform Plane Wave Normally Incident on a Parallel, Plane Plasma Slab

For the plasma,

$$\gamma_p = \alpha_p + j\beta_p$$

where

$$\alpha_p = \frac{2\pi}{\lambda_0}\frac{1}{\sqrt{2}}\left[-\epsilon_r + \left(\epsilon_r^2 + \sigma_r^2\right)^{1/2}\right]^{1/2}$$

$$\beta_p = \frac{2\pi}{\lambda_0}\frac{1}{\sqrt{2}}\left[\epsilon_r + \left(\epsilon_r^2 + \sigma_r^2\right)^{1/2}\right]^{1/2}$$

and

$$\epsilon_r = 1 - \frac{\omega_p^2}{\omega^2 + \nu_c^2}$$

$$\sigma_r = \frac{\nu_c}{\omega} \frac{\omega_p^2}{\omega^2 + \nu_c^2}$$

$$\omega_p^2 = \frac{e^2 N_e}{\epsilon_0 m}$$

e = electron charge

m = electron mass

N_e = electron density

ϵ_0 = permittivity of free space

ω_p is the angular plasma frequency and ν_c is the collision frequency.

The transmission coefficient at z = d is

$$T = \frac{A}{A_0} \exp(j\phi') \tag{7}$$

A is the amplitude of the transmitted wave at z = d, and A_0 is the amplitude of the incident wave. ϕ' is the phase difference between the transmitted wave at z = d, before and after the introduction of the plasma slab.

This expression for T can be expressed as a function of both $\frac{\omega_p}{\omega}$, $\frac{\nu_c}{\omega}$, and d. Although it is complicated and difficult to interpret, if the following approximation is made

$$\left| \frac{(\omega_p/\omega)^2}{1 - j(\nu_c/\omega)} \right| << 1 \tag{8}$$

then the transmission coefficient can be simplified to

$$T \cong \exp\left[-\frac{\nu_c}{\omega}\,\frac{(\omega_p/\omega)^2}{1+(\nu_c/\omega)^2}\,\frac{\pi}{\lambda_0}\,d\right] \cdot \exp\left[j\,\frac{(\omega_p/\omega)^2}{1+(\nu_c/\omega)^2}\,\frac{\pi}{\lambda_0}\,d\right]$$

or (9)

$$T \cong \exp\left[-\alpha d\right]\exp\left[j\beta d\right]$$

where (10)

$$\alpha = \frac{\nu_c}{\omega}\,\frac{(\omega_p/\omega)^2}{1+(\nu_c/\omega)^2}\,\frac{\pi}{\lambda_0}$$

and (11)

$$\beta = \frac{(\omega_p/\omega)^2}{1+(\nu_c/\omega)^2}\,\frac{\pi}{\lambda_0}$$

Comparing Eqs. (7) and (9), it follows that

$$\alpha d = \ln\frac{A}{A_0} \tag{12}$$

and (13)

$$\beta d = \phi'$$

Equations (12) and (13) are particularly simple since A/A_0 and ϕ' are quantities that are readily measured. A_0 and the initial phase are recorded before the introduction of the plasma. After the plasma is introduced, the amplitude A and final phase are recorded. ϕ' is simply the difference of the two phase angles.

The plasma parameters ω_p/ω and ν_c/ω may then be obtained in terms of the measured quantities A, A_0 and ϕ'.

For example,

$$\frac{\alpha}{\beta} = \frac{\ln \frac{A}{A_0}}{\phi^0} = \frac{\nu_c}{\omega}$$

Substitution of ν_c/ω into Eqs. (10) and (12), or Eqs. (11) and (13), will determine ω_p/ω.

A special case of interest is the low-loss plasma, for which $(\nu_c/\omega)^2 << 1$.

Equations (10) and (11) become

$$\alpha = \frac{\nu_c}{\omega} \left(\frac{\omega_p}{\omega}\right)^2 \frac{\pi}{\lambda_0} \tag{10}$$

$$\beta = \left(\frac{\omega_p}{\omega}\right)^2 \frac{\pi}{\lambda_0} \tag{11}$$

Since $(\omega_p/\omega)^2 = N_e/(N_e)_c$

(where N_e is the actual electron density

and $(N_e)_c$ is the electron density which would result in cutoff at the frequency ω), the phase shift parameter β is directly proportional to the electron density.

An important feature of the underdense plasma is the condition of inequality (Eq. (8)) which defines the transition from dense to underdense plasma. If it is assumed from Eq. (8) that

$$\frac{(\omega_p/\omega)^2}{\sqrt{1+(\nu_c/\omega)^2}} \leq \frac{1}{10} \tag{14}$$

then by comparison, similar terms squared may be neglected. Preliminary computation based on a comparison of exact theory with the equality defined by Eq. (14) shows that negligible error is introduced by the underdense approximation. The inequality defined by Eq. (14) is plotted in Fig. 11-4. The way in which this curve is used is as follows.

The plasma parameters ω_p/ω and ν_c/ω are determined from measurements of A, A_0 and ϕ' using Eqs. (12) and (13). The underlying assumption is that of an underdense plasma. The values ω_p/ω and ν_c/ω are then plotted to ensure that they fall in the right-hand portion of the diagram. If they do not, the assumption is not justified and the results should be used with caution.

Radial Variation in Electron Density

In preceding paragraphs it has been understood that the radial distribution of electron density and collision frequency in an ionized wake is constant. This has not been borne out by practical experience, so a method by which information on radial gradients may be obtained will be outlined.

Use is made of the fact that a focused microwave beam can be so well-collimated that several beams can be placed adjacent to each other without significant mutual interference. If the beams are stacked in a plane which is normal to the flight direction, additional data on radial variations in ionization may be extracted from the measured transmission coefficients of the beam.

An idea of how the radial variations may be obtained can be derived from Fig. 11-5, in which seven adjacent beams intersect a cylindrical wake.

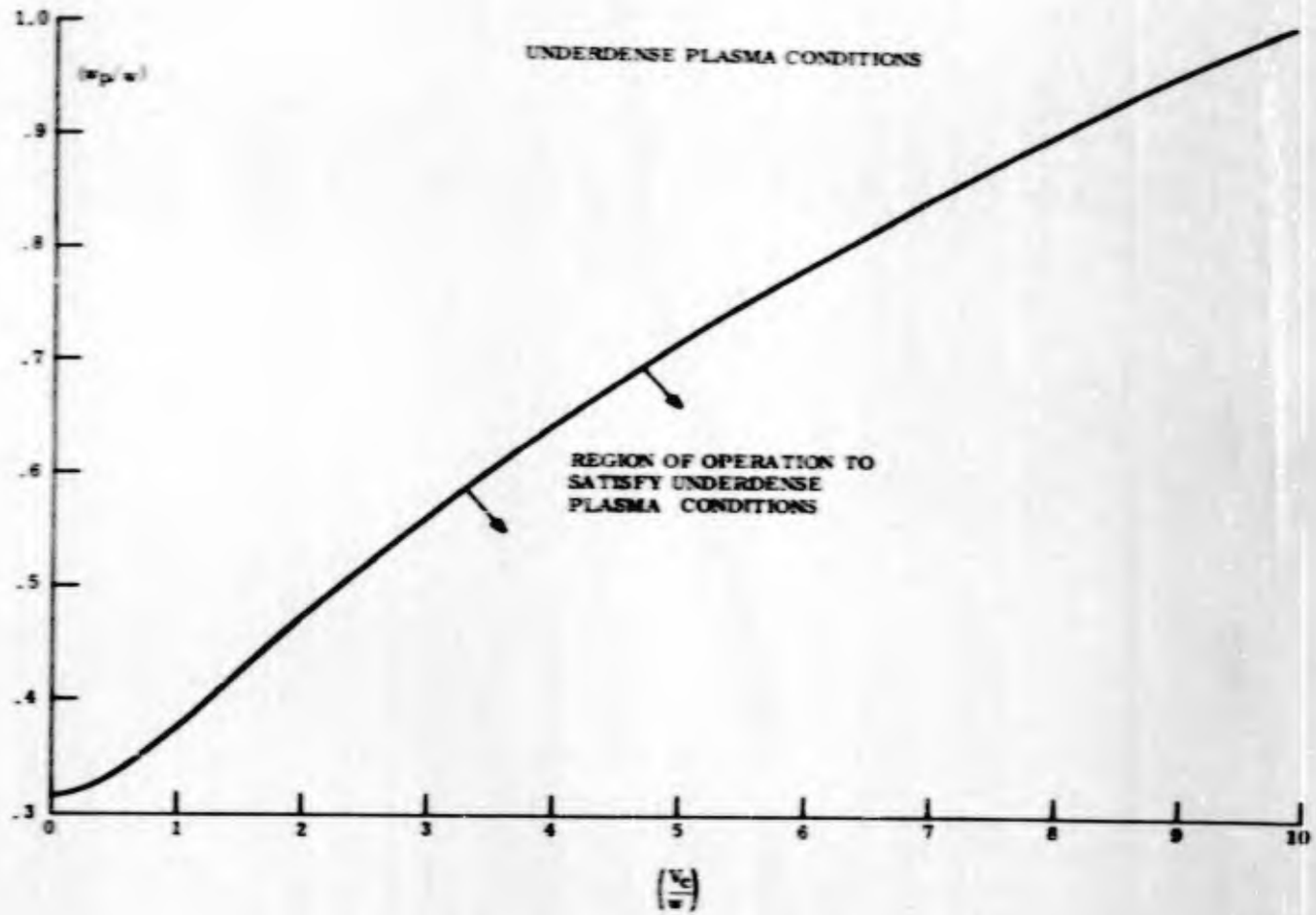

Fig. 11-4 Underdense Plasma Conditions

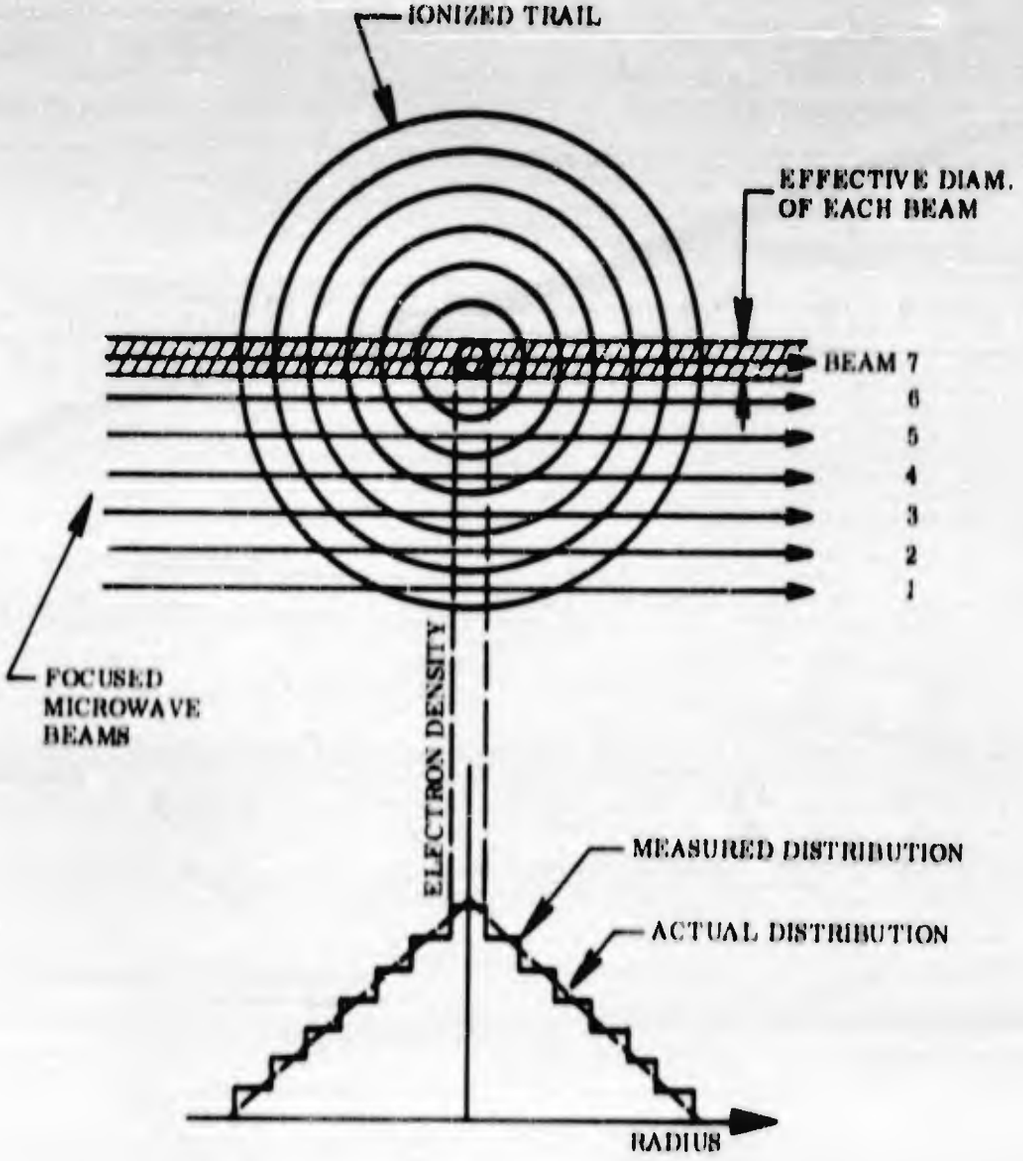

Fig. 11-5 Measurement of Radial Distribution of Ionization in Hypersonic Wake

The axisymmetric wake is supposedly broken up into a number of concentric layers, the thickness of each determined by the effective diameter of the microwave beam. The radial positions of the layers are determined by the positions of the adjacent beams.

A simple approach to the analysis of data in such a system is made by utilizing the underdense plasma approximation outlined in the previous subsection. Under these conditions, phase shifts and attenuations contributed by each layer are additive, and all multiple reflections are ignored. Each beam is replaced by a ray which passes through the mid-point of each layer.

The procedure for obtaining the radial distributions of both electron density and collision frequency will be illustrated by considering the passage of the k^{th} beam through the layered wake. The subscript q will denote the number of the layer, starting from the inner core.

Let $\phi_{k,q}$ and $\alpha_{k,q}$ denote phase shift per unit length and attenuation per unit length, respectively, experienced by the k^{th} beam in passing through the q^{th} layer of the wake.

Let $\ell_{k,q}$ denote the corresponding mean path length.

Let Φ_k denote the total phase shift experienced by the k^{th} beam in passing through the whole wake.

Let $\mathcal{L}_k$ denote the total attenuation experienced by the k^{th} beam in passing through the whole wake.

Then

$$\Phi_k = \phi_{k,q}\, l_{k,q} + \phi_{k,q-1}\, l_{k,q-1} + \cdots + \phi_{k,1}\, l_{k,1}$$

There are m such equations – one for each beam (m is the total number of beams). Since Φ_k is a measured quantity and $l_{k,q}$ is known from the geometry of the system, then the set of equations can be solved simultaneously to yield $\phi_{k,q}$.

Similarly $\alpha_{k,q}$ gives

$$\alpha_k = \alpha_{k,q}\, l_{k,q} + \alpha_{k,q-1}\, l_{k,q-1} + \cdots + \alpha_{k,1}\, l_{k,1}$$

From the complete set of equations, $\alpha_{k,q}$ may be determined

Now
$$\phi_{k,q} = \frac{\pi}{\lambda_0} \frac{\left((\omega_p)_q/\omega\right)^2}{1 + \left((\nu_c)_q/\omega\right)^2} \tag{15}$$

and
$$\alpha_{k,q} = \frac{\pi}{\lambda_0} \frac{(\nu_c)_q}{\omega} \frac{\left((\omega_p)_q/\omega\right)^2}{1 + \left((\nu_c)_q/\omega\right)^2} \tag{16}$$

where $(\omega_p)_q$ is the plasma frequency of the q^{th} layer, and $(\nu_c)_q$ is the collision frequency of the q^{th} layer.

Since $\phi_{k,q}$ and $\alpha_{k,q}$ are now known, Eqs. (15) and (16) can be solved simultaneously for $(\omega_p)_q$ and $(\nu_c)_q$, as in the previous subsection.

EQUIPMENT DETAILS

Selection of Operating Frequency

The selection of frequencies is governed to a large extent by the electron densities that are to be expected in the wakes of hypersonic projectiles, fired under conditions representative of those experienced during ICBM reentry. The maximum electron densities to be expected during reentry are of the order of $10^{16\text{-}17}$ e/cc, and the lowest of interest are about $10^{8\text{-}9}$ e/cc. The corresponding plasma frequencies are of the order of hundreds of megacycles per second ($10^{8\text{-}9}$ e/cc) to frequencies which have free-space wavelengths well into the submillimeter band.

Musal (Ref. 5) has estimated electron densities in the far wake over a wide range of conditions, from which it is possible to determine the effectiveness of a particular frequency in the measurement of wake electron densities. An example of such a calculation is shown (Fig. 11-6) in which the effectiveness of a 35-Gc/s probing frequency is illustrated. The maximum measurable density is determined by the condition that the plasma frequency be 35 Gc/s, i. e., $(N_e)_c \cong 1.5 \times 10^{13}$ e/cc. If the underdense approximation is used, this density has to be reduced by a factor of 10. The minimum measurable density is a strong function of the sensitivity of the measuring device; and for the equipment described, it was found to be about 10^{10} e/cc. Additional practical experience has shown successful probe operation into the far left of the diagram (Fig. 11-6) which indicates that the estimates of wake densities in Ref. 5 are too conservative. This is not too surprising in that Musal's analysis predicts neither the diameter of the wake nor the distance behind the projectile at which far-wake conditions prevail. However,

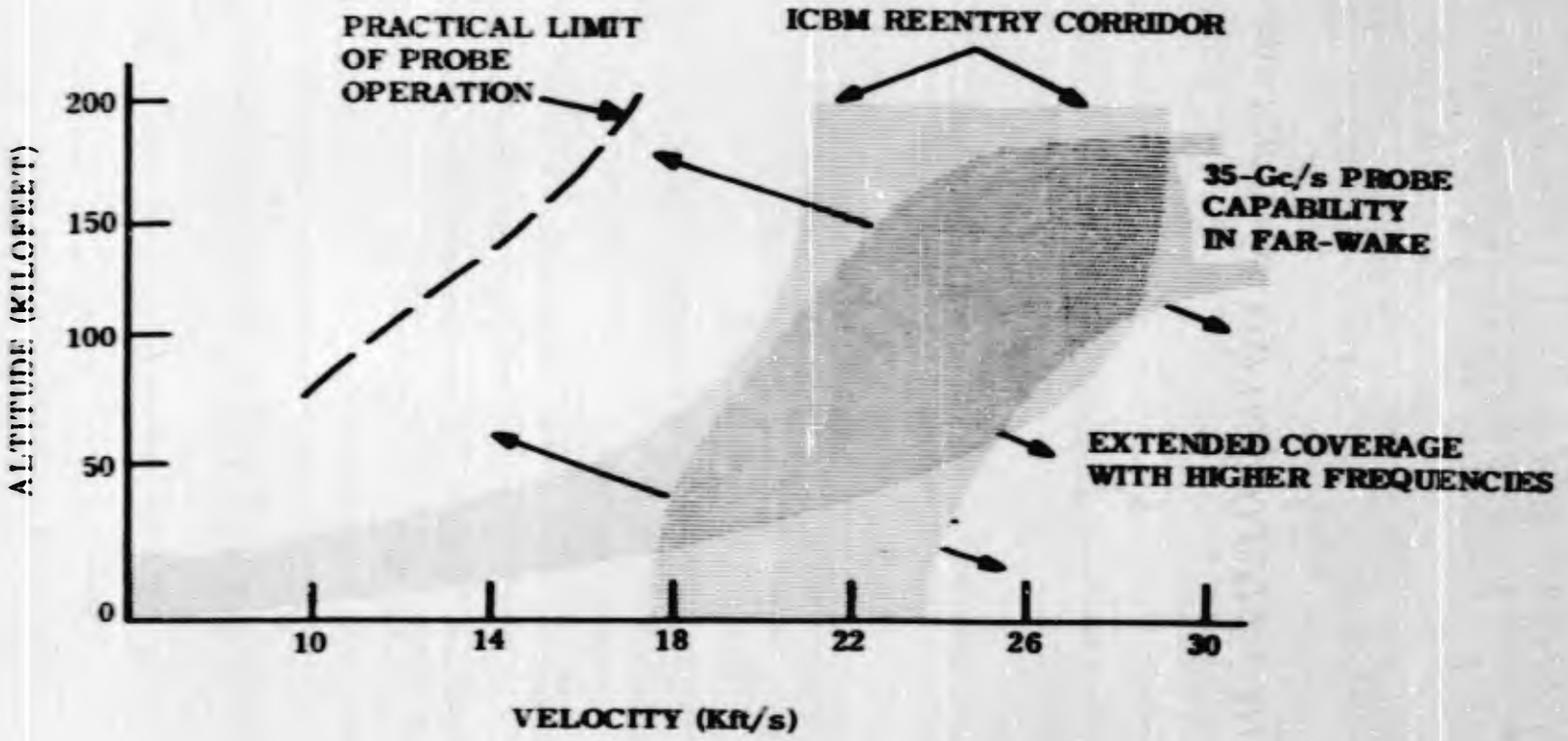

Fig. 11-6 35-Gc/s Microwave Probe Capability — Far Wake

it is clear that frequencies of the order of 35-Gc/s and higher would be extremely useful for wake studies.

The choice of frequency is also governed by the spatial resolution required which, in turn, is determined by model size. For the 3/4-in. diameter models of current interest, resolutions of no more than 3/4 in. are desirable. The arguments outlined in the subsection on Focused Microwave Apertures lead to the conclusion that wavelengths in the millimeter range would be most useful in the production of beam dimensions of this order. For instance, a frequency of 35 Gc/s would result in achievable resolutions of about 1/2 – 3/4 in. A frequency of 70 Gc/s would increase these resolutions by a factor of two.

A combination of these factors leads to a selection of frequencies of 35 Gc/s and higher. To date, systems have been developed which use 35 Gc/s and 70 Gc/s, precise values which were dictated by the availability of commercial equipment. Experience has shown that, with this choice, electron densities in the range 10^{10} - 10^{13} e/cc can be measured with ease. It can be seen from the subsection on Focused Microwave Apertures Eq. (6), that trail diameters which can be measured accurately are:

$$35\ \text{Gc/s}: \quad 0.75'' \leq D_T \leq 4''$$

$$70\ \text{Gc/s}: \quad 0.38'' \leq D_T \leq 2''$$

The Focused Antennas

In the present instance, a focused microwave beam is produced by inserting a plastic lens in the path of radiation which has a spherical

phase front at the lens. A small conical horn is used to illuminate the lens. (See Fig. 11-7.) The lens is constructed of low-loss polystyrene and consists of two identical plano-convex sections. The function of the curved surface opposite the feed horn is to convert the incident spherical wavefront into a plane wavefront. The second section of the lens is used to convert the plane wavefront into a spherical wavefront which converges towards the focal region. For simplicity in construction, the feed distance and focal length are made to be equal, since this results in a symmetrical lens.

The focal ratio of the lens is unity in order to produce the smallest focused beam size. At the same time, the illumination across the lens is tapered so that maximum collimation of the energy in the focal region may be achieved.

The optimum taper has been obtained by using a small conical feed horn with the correct aperture-to-length ratio. It should be noted that the result is not an optimum gain horn, as the antenna system does not have maximum gain for the aperture size chosen. However, this disadvantage is more than offset by the optimum collimation available.

The measurement of the properties of the focal field is an extremely difficult task, due to the fact that the dimensions of the focal region are comparable to those of available pickup antennas so will not be dealt with in detail here. In brief, the field distribution in the focal region was obtained by measuring the back-scatter from metallic spheres (very much smaller than the wavelength – about 1/20 λ) which were made to traverse the focal region. An example of the measured field distribution (amplitude and phase) in the focal plane is shown in Figs. 11-8a and 11-8b. The resolution of the lens was determined by passing two

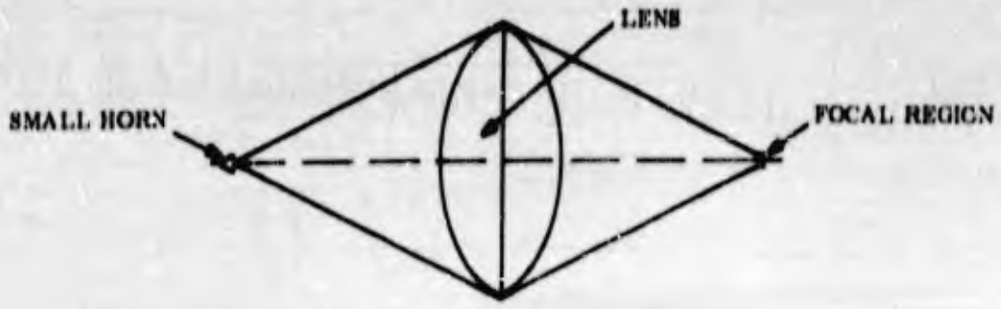

Fig. 11-7 Focusing Lens

identical small spheres through the focal plane to achieve various spacings between the spheres (Fig. 11-9). Where the spheres are separated by more than a beamwidth, the field distribution in the focal plane is traced out by each sphere. As the spheres are placed closer together, the two patterns ultimately overlap. An arbitrary criterion for resolution is taken to be the condition that two identical objects in the focal plane produce field patterns which overlap at the 3-db points. It can be seen, for the 70-Gc/s results shown, that the resolution is about 1/4 in., which is in good agreement with predictions based on the theoretical antenna pattern.

The manner in which the lens system (Fig. 11-7) is utilized to construct a plasma probe is depicted in Fig. 11-10. Identical lenses and feed horns are used for both transmission and reception. Each lens is mounted in the side of the 2-ft-diameter section of the physics range and forms an air-tight seal with the range. The physical advantage of using a horn-lens combination, rather than, say, an elliptical reflector, is evident from this diagram.

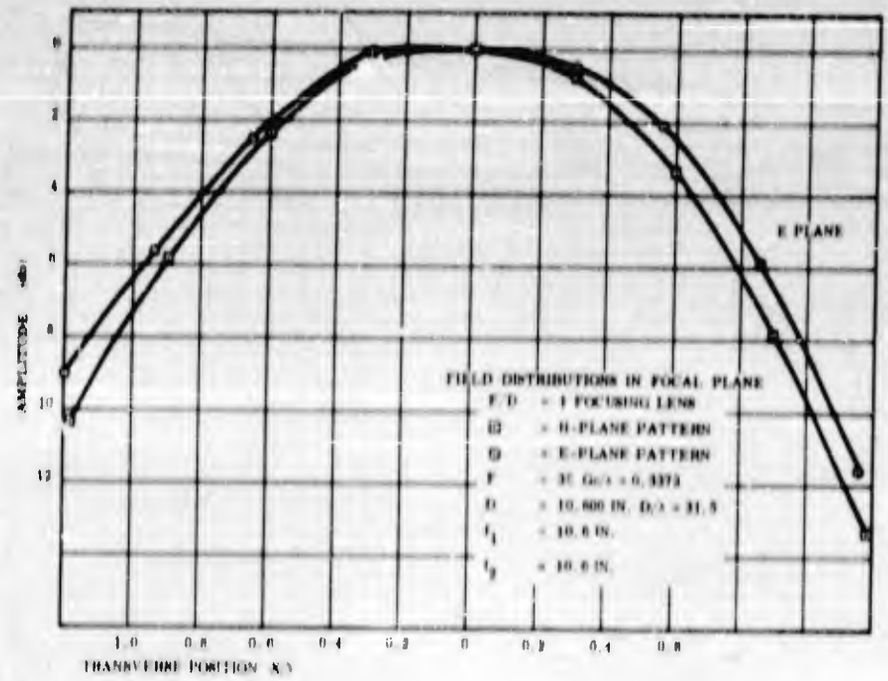

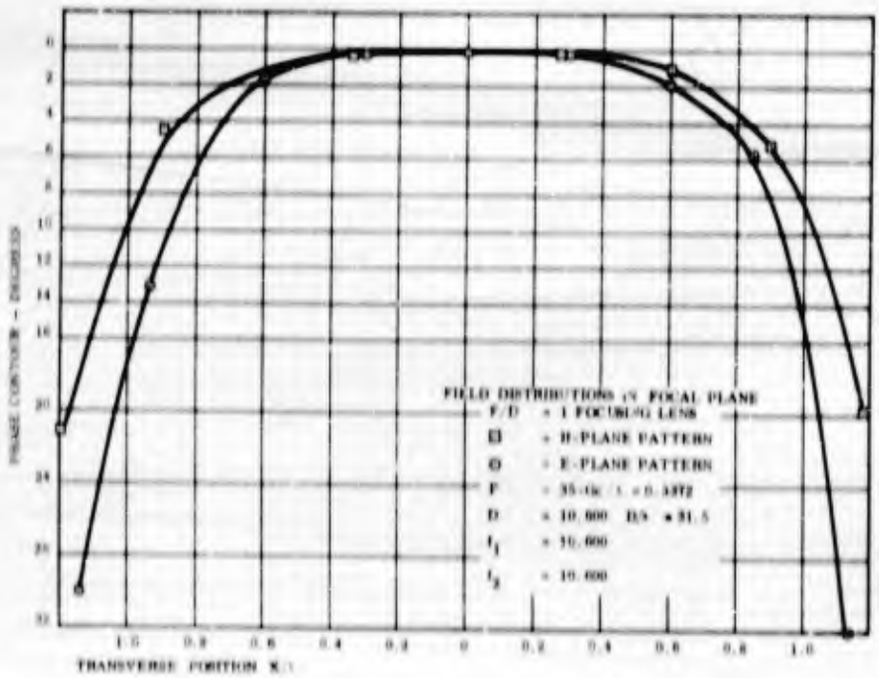

Fig. 11-8 Field Distribution in Focal Plane

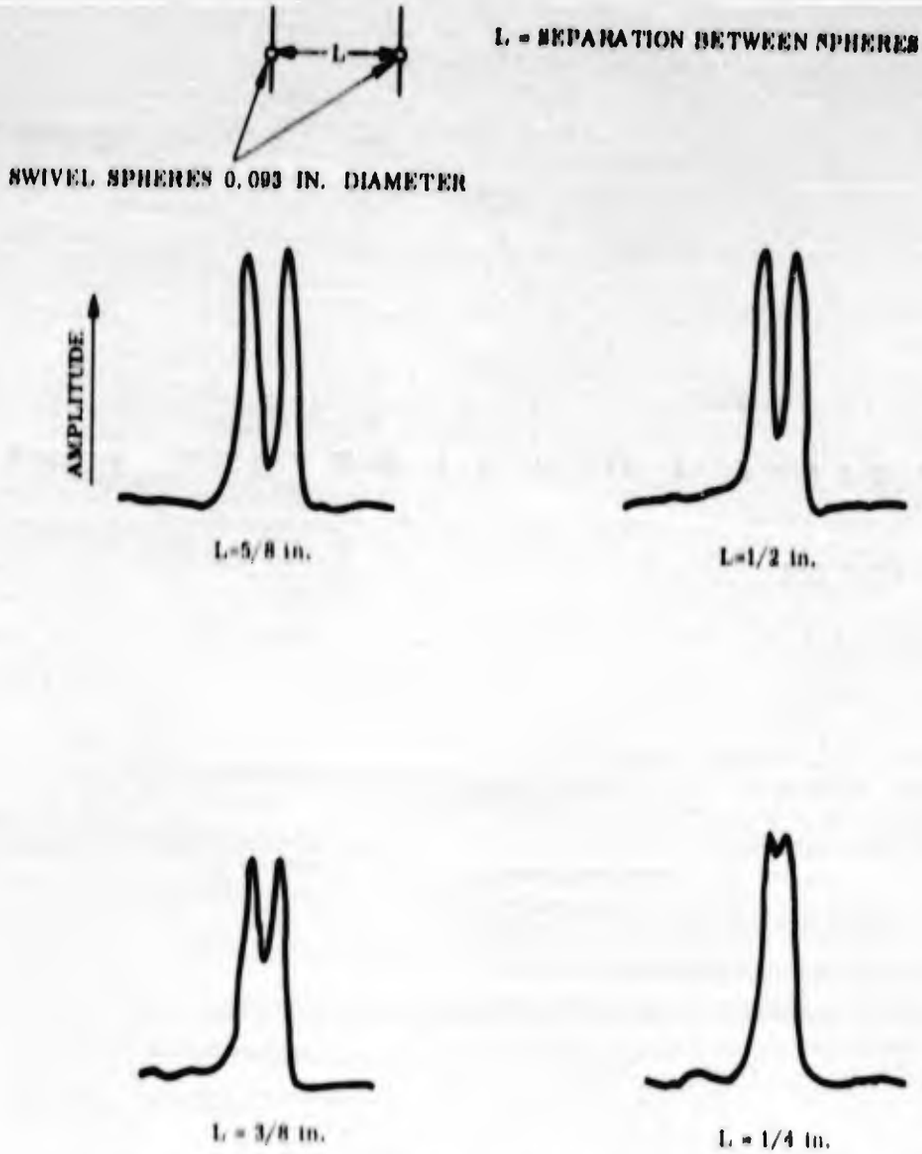

NOTE: MEASURED PATTERNS TO BE REDUCED BY SPHERE DIAM(.093 in) TO GIVE ACTUAL BEAM PATTERN

Fig. 11-9 70-Gc/s Probe Resolution Measurements

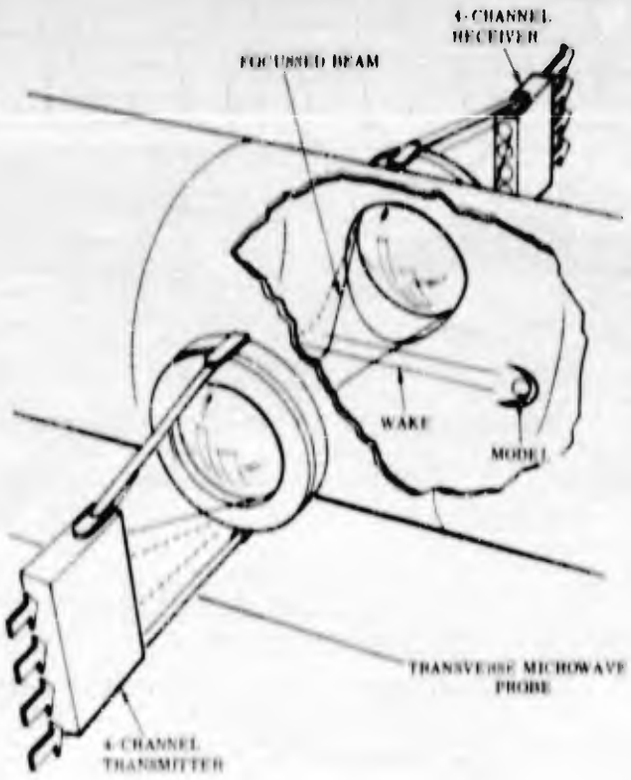

Fig. 11-10 Transverse Focused Microwave Probe

The power transmission through the system is specified in terms of the insertion loss. When the feed horn is located on axis, the insertion loss has been found to be about 10 db – or 5 db per lens system – at both 35 Gc/s and 70 Gc/s. The loss can be reduced to about 3 db per lens by matching each curved surface. The residual loss (3 db per lens) is inherent in the lens-feed system and cannot be reduced without interfering with the collimating properties.

If single, on-axis, feed horns are used, the resulting focused beam will intercept some part of the flow field. In order to cover the major part of the flow field in the radial direction while allowing for some dispersion in firing, it has been necessary to employ several adjacent beams, provided for by separate off-axis feed horns.

The off-axis scanning properties of the system were investigated by a measurement of the transmission of a single beam, where the feed horns (transmitter and receiver) were moved in unison in a direction transverse to the axis. It was found that the horns could be moved about 1 in. off axis without any appreciable decrease in transmission (Fig. 11-11). Consequently, separate beams could be produced by locating additional pairs of feed horns – one on the transmitter side and the other on the receiver side – anywhere within a 1-in.-radius circle, centered on axis. In general, the spacing between feed horns is made equal to the spatial resolution. Feed horns are stacked in a vertical plane normal to the flight path, and the polarization of adjacent channels is alternated in order to minimize cross-coupling between channels. The present disposition of the 35-Gc/s and 70-Gc/s system beams in the focal plane is shown in Fig. 11-12.

Types of Measurement Systems

During the development of the probe equipment, two basic measuring systems have been used. The first is the amplitude system used to measure only the change in the amplitude of the transmitter signal caused by the interruption of the beams by the wake; the second is the system used to measure both amplitude and phase with the phase quadrature circuit. The sequence in the equipment development has been as follows: (1) a four-channel amplitude system, (2) 35-Gc/s, four-channel phase-and-amplitude system, (3) 70-Gc/s, seven-channel amplitude system, (4) 70-Gc/s seven-channel phase-and-amplitude system, and (5) 35-Gc/s seven-channel phase-and-amplitude system.

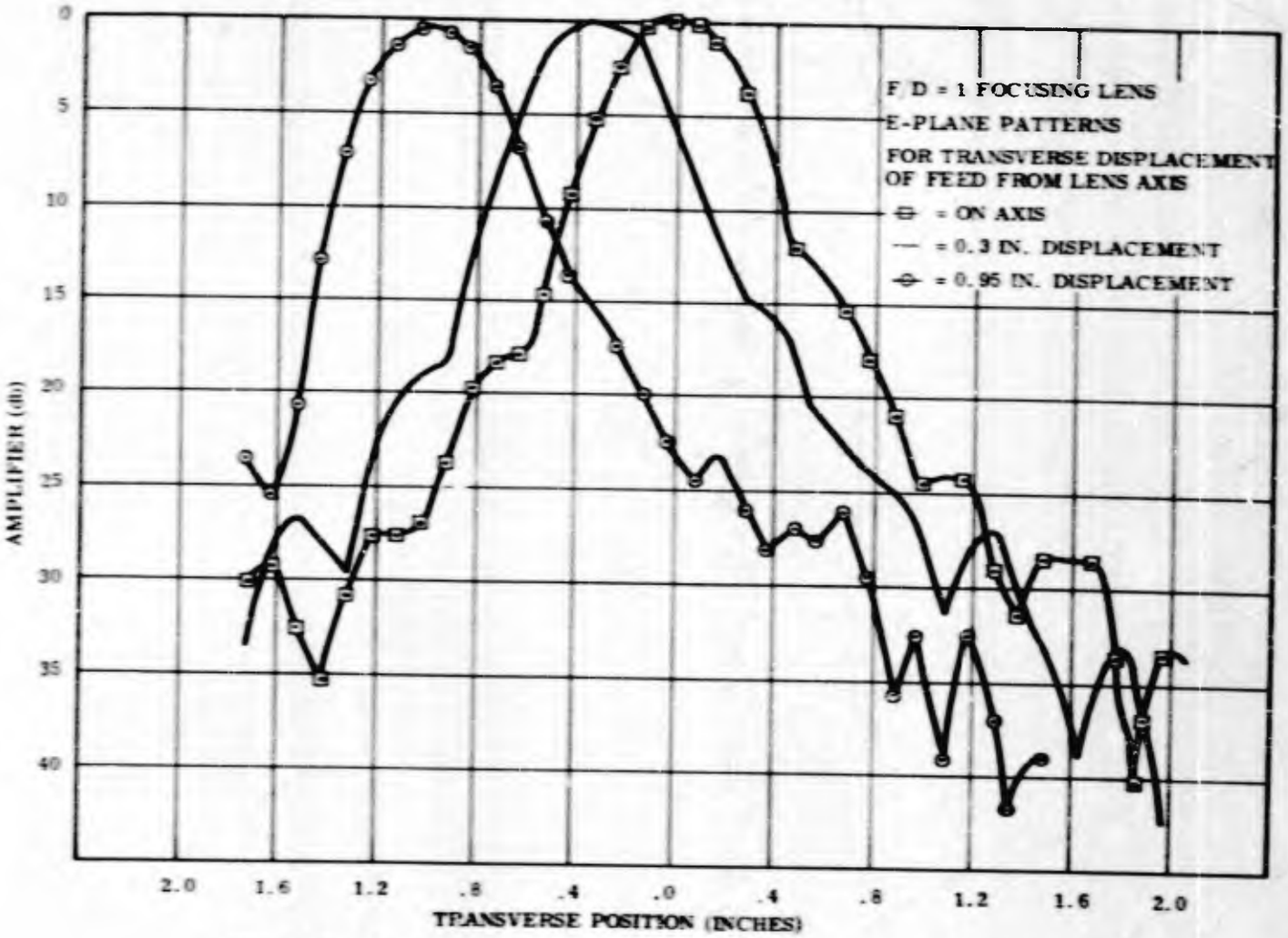

Fig. 11-11 Off-Axis Scanning Properties of the Focusing Lens

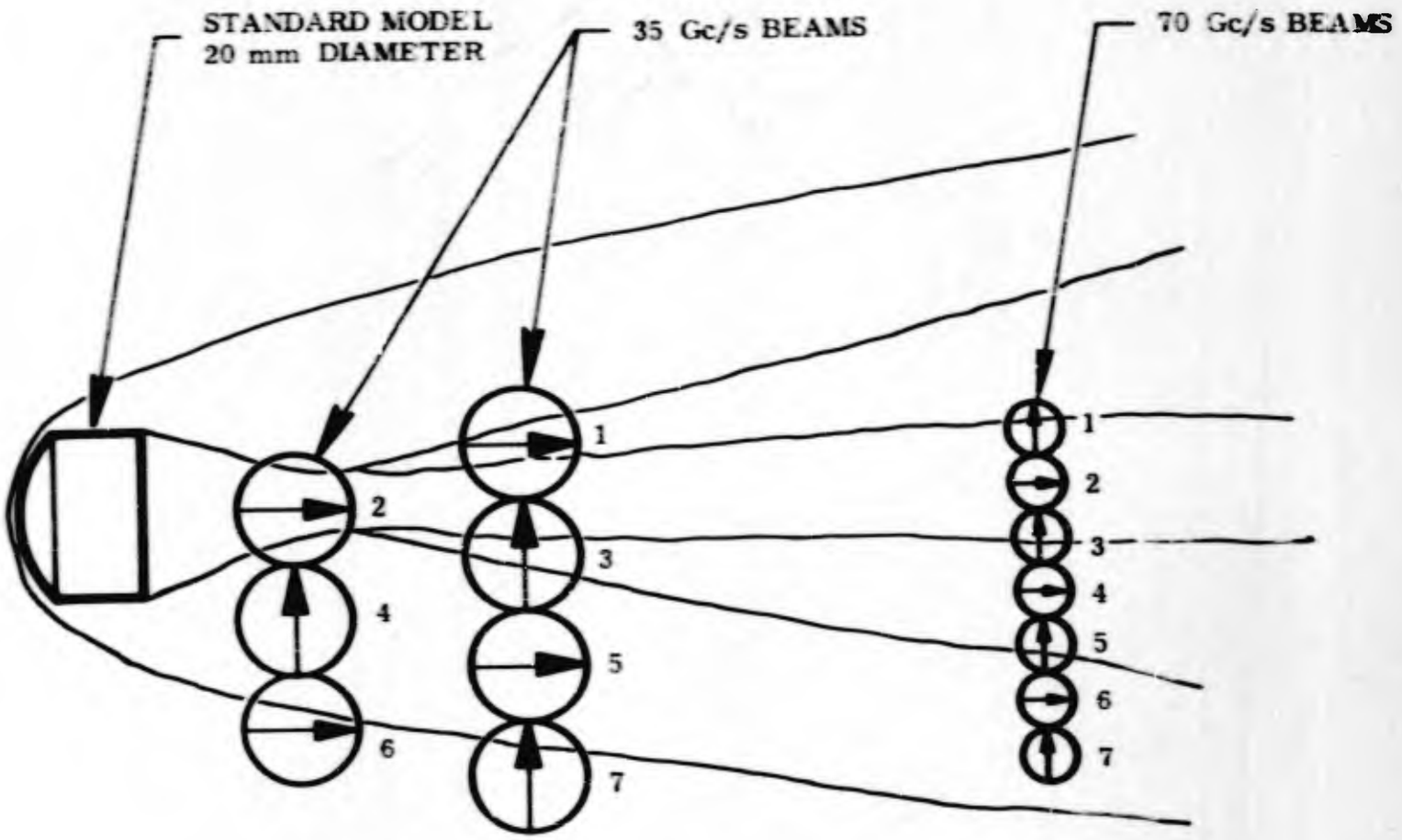

Fig. 11-12 Ideal Disposition of Focused Microwave Beams across a Hypersonic Wake

AMPLITUDE SYSTEM. The main reason for using the amplitude system as an initial stage in the development of both the 35-Gc/s and 70-Gc/s probes was the simplicity of the measurement circuit. By measuring the change caused by the plasma wake in the amplitude of the signal, collision frequency can be obtained for regions of the wake where attenuation of the signal can be assumed to be wholly due to collision processes. The amplitude measurements also give a measure of trail duration and, where multiple beams are used, detailed structure of the wake near the projectile and trail diameter (as discussed in a later section). The disadvantage of this system is that it cannot be used to measure the change in the phase of the transmitter signal and, therefore, cannot give information on electron density of the wake.

Amplitude System Description -- A simplified schematic of a one-channel, amplitude-measuring system is shown in Fig. 11-13. The signal from the transmitter klystron goes to a feed horn which illuminates the focusing lens on the transmitter side. The signal is then focused by the lens to form a beam of about 1/2-in. diameter for the 35 Gc/s and of 1/4-in. diameter for the 70-Gc/s probe at the center of the range. An identical feed horn and lens system on the receiver side collects the beam energy at the center of the range. From the receiver horn, the signal goes to a microwave diode operated as a video, square-law detector to give output voltage proportional to the transmitted signal power. A photograph of an oscilloscope trace showing the change in transmitted signal amplitude as a function of time is then recorded.

35-Gc/s Four-Channel Amplitude System -- In the 35-Gc/s system, the transmitter signal is split up by short slot hybrids to energize four feed

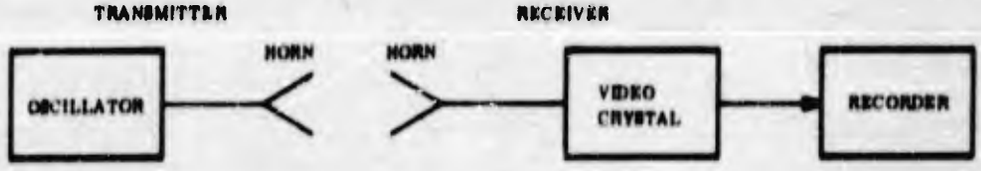

Fig. 11-13 Block Diagram of Amplitude System

horns in a block as shown in Fig. 11-14. The energy from each of the four feed horns is focused by the lens to form four beams of 1/2-in. diameter, with beam centers 1/2 in. apart to set up a vertical fence which intercepts the projectile in flight. On the receiver side, the feed horns collect the energy of the beam from its mate in a corresponding position of the transmitter feed horn block. Cross-coupling between channels is reduced by using orthogonal polarization between adjacent channels. Isolation between adjacent channels which are cross-polarized is greater than 25 db, and greater than 20 db for alternate channels which have the same polarization. The signal from each of the horns in the receiver goes to separate diode detectors, and the amplified signals are recorded as four separate oscilloscope traces. The oscilloscopes are triggered when a focused microwave fan beam located uprange from the recording beams is interrupted by a projectile. This fan beam is formed by a line source which can be seen adjacent to the horn block.

Calibration of Amplitude System -- Calibration of the system is carried out before each firing by adjusting attenuators ahead of each of the detector diodes so that they operate at the same known level. The output signal varies from a maximum value (zero attenuation) before a firing

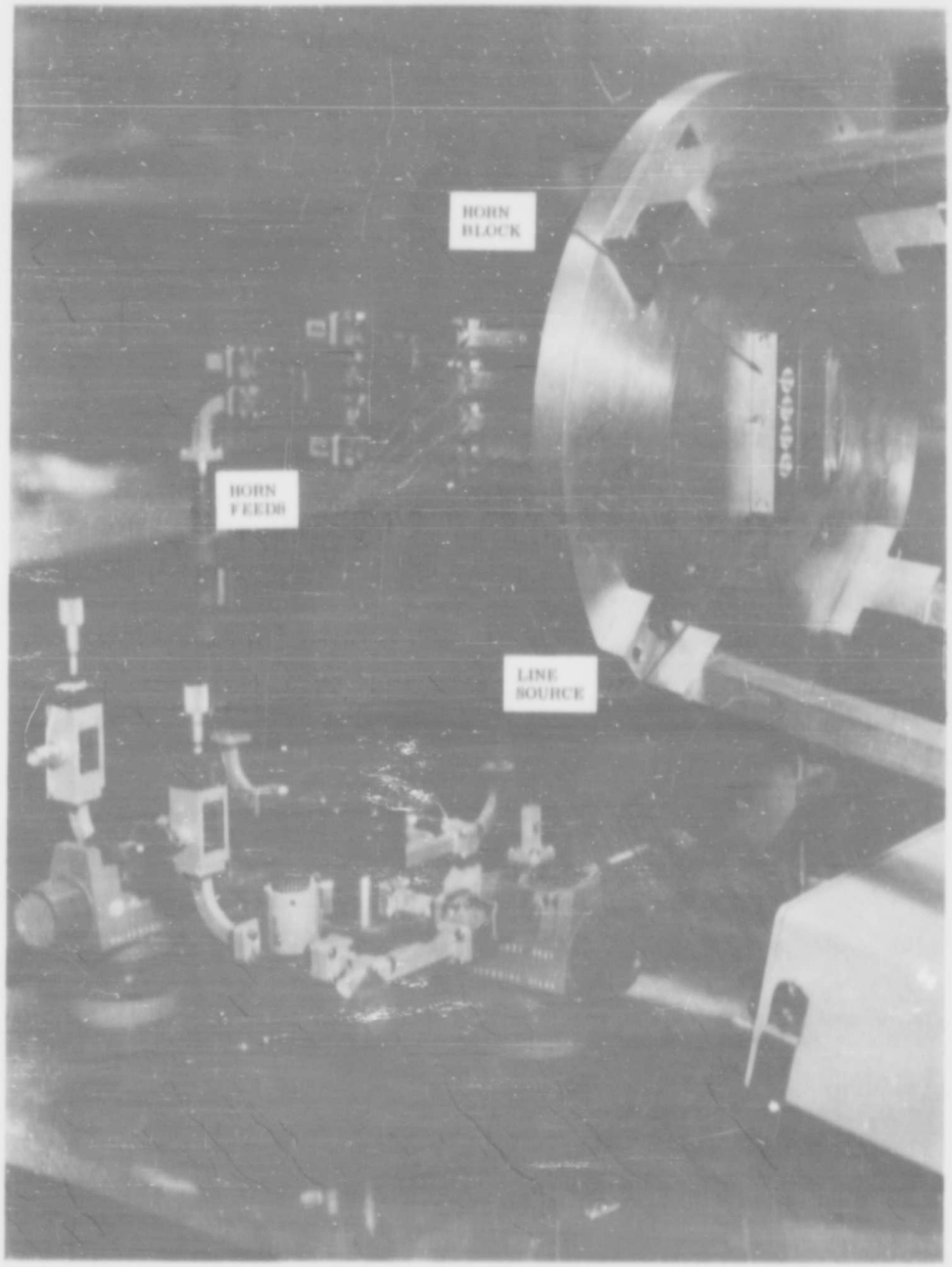

Fig. 11-14 Transmitter of 35-Gc/s, Four-Channel Amplitude System Showing Feed Horn Block

to zero (maximum attenuation) for a beam completely cut off by a projectile or overdense plasma. Since the maximum level is set before a firing, the oscilloscopes are readily adjusted to give suitable, calibrated deflections of the change in signal amplitude.

70-Gc/s Seven-Channel Amplitude System -- The 70-Gc/s amplitude system is essentially the same as the 35-Gc/s system, except for the differences in number of channels and operating wavelength. The shorter wavelength, of course, requires different microwave components and also means that the focused beams are now 1/4-in. diameter instead of 1/2 in. at 35 Gc/s. Horn blocks with seven feeds are used to produce a fence of seven beams 1/4 in. in diameter and with the beam centers 1/4 in. apart at the center of the range. The polarization of the feed horns is again alternated between adjacent channels to keep the cross-coupling at approximately the same level as for the 35-Gc/s probe. The intercept area with the seven beams is almost the same as for the four beams of the 35-Gc/s probe; but the finer beams have twice the resolution and give a much clearer picture of the wake structure in the vicinity of the projectile, both in the radial and axial direction of the wake.

Calibration procedure is as for the 35-Gc/s amplitude system, except that sweep speeds were generally set higher to take advantage of the resolution capabilities of the finer beams.

Typical Results 35-Gc/s and 70-Gc/s Amplitude Systems -- Figure 11-15 is a typical 35-Gc/s amplitude trace. Points on the trace are correlated with points on the model and its wake. In all cases, the ordinates are in terms of amplitude changes and the abscissas in terms of time. The first main pulse is due to the passage of the projectile

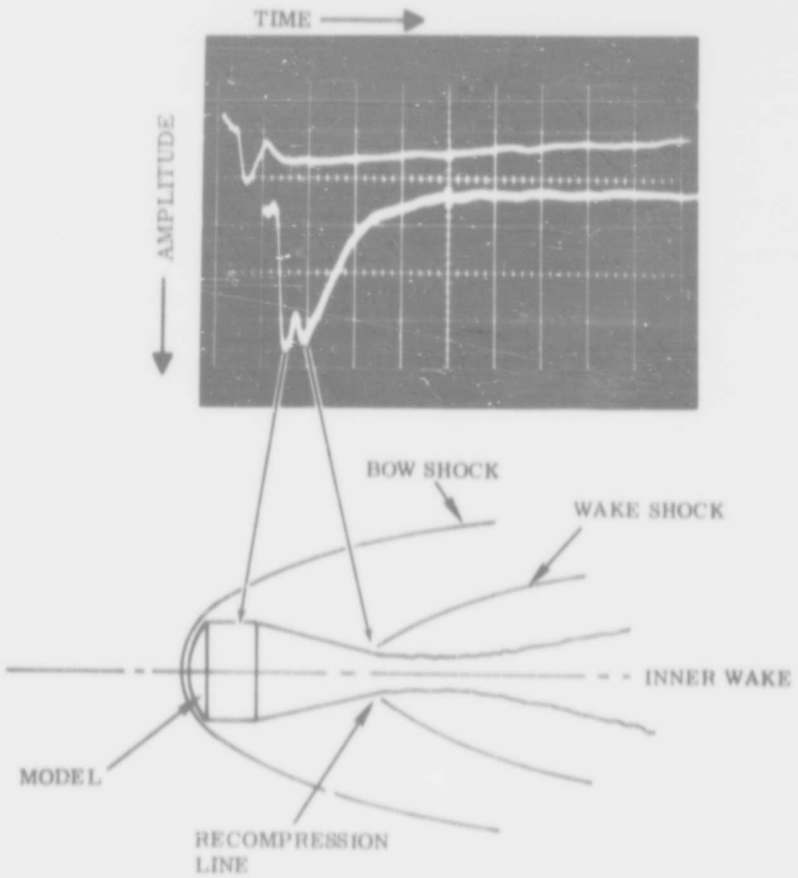

Fig. 11-15 Typical Oscilloscope Trace from the 35-Gc/s Amplitude System

and the associated bow shock-wave ionization through the microwave beam. The second pulse is believed to be due to intense ionization in the recompression region behind the body.

In Fig. 11-16a the response of four adjacent amplitude channels is shown. In this case the projectile appeared to pass through channel 3.

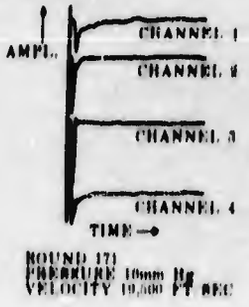

FIGURE 11-16a MICROWAVE PROBE DATA - ROUND 171

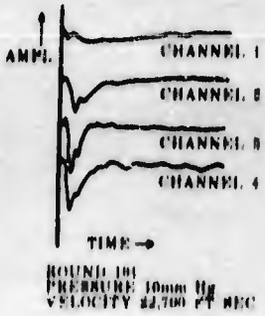

FIGURE 11-16b MICROWAVE PROBE DATA - ROUND 191

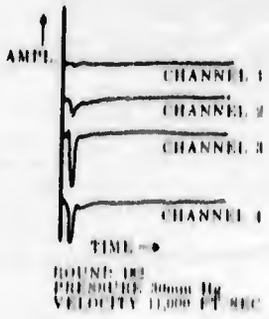

FIGURE 11-16c MICROWAVE PROBE DATA - ROUND 182

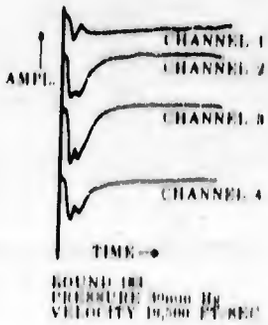

FIGURE 11-16d MICROWAVE PROBE DATA - ROUND 183

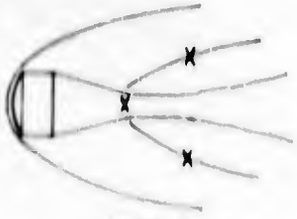

FIGURE 11-16e

Fig. 11-16 35-Ge/s, Four-Channel Amplitude Results

There are small pulses behind the projectile in the side channels, whereas only a slight disturbance is evident in the center channel. However, as the velocity is increased, a strong second pulse is indicated in all channels (Fig. 11-16b). A repeat of these phenomena at a different velocity and pressure is indicated in Figs. 11-16c and 11-16d. A careful study of these results has shown that the pulses on the side channels occur later than those on the center channel (Fig. 11-16e). A tentative conclusion is that the pulses correspond to ionization in the recompression zone and along the secondary shocks.

A 70-Gc/s amplitude result is shown (Fig. 11-17) with a schlieren photograph of the model in flight. The resolution capabilities of the 70-Gc/s probe can be readily seen from the comparison of the record with the photograph. It is evident that the second attenuation pulse is associated with the recompression zone. Not shown is an additional feature which is that the dimension of the recompression zone (in terms of electron density) is about 1/4 in., since beams adjacent to the on-axis beam showed little evidence of the recompression.

PHASE QUADRATURE AMPLITUDE-AND-PHASE SYSTEM. The microwave signal which is transmitted through an ionized wake is a time-varying function of both amplitude and phase, which in turn are functions of the electron density, collision frequency, surface reflections and wake dimensions. It has been shown that for underdense plasmas, independent measurements of signal amplitude and phase can be used to determine the spatial distribution and magnitude of both the electron density and collision frequency. This is achieved by the phase quadrature system shown in block form (Fig. 11-18).

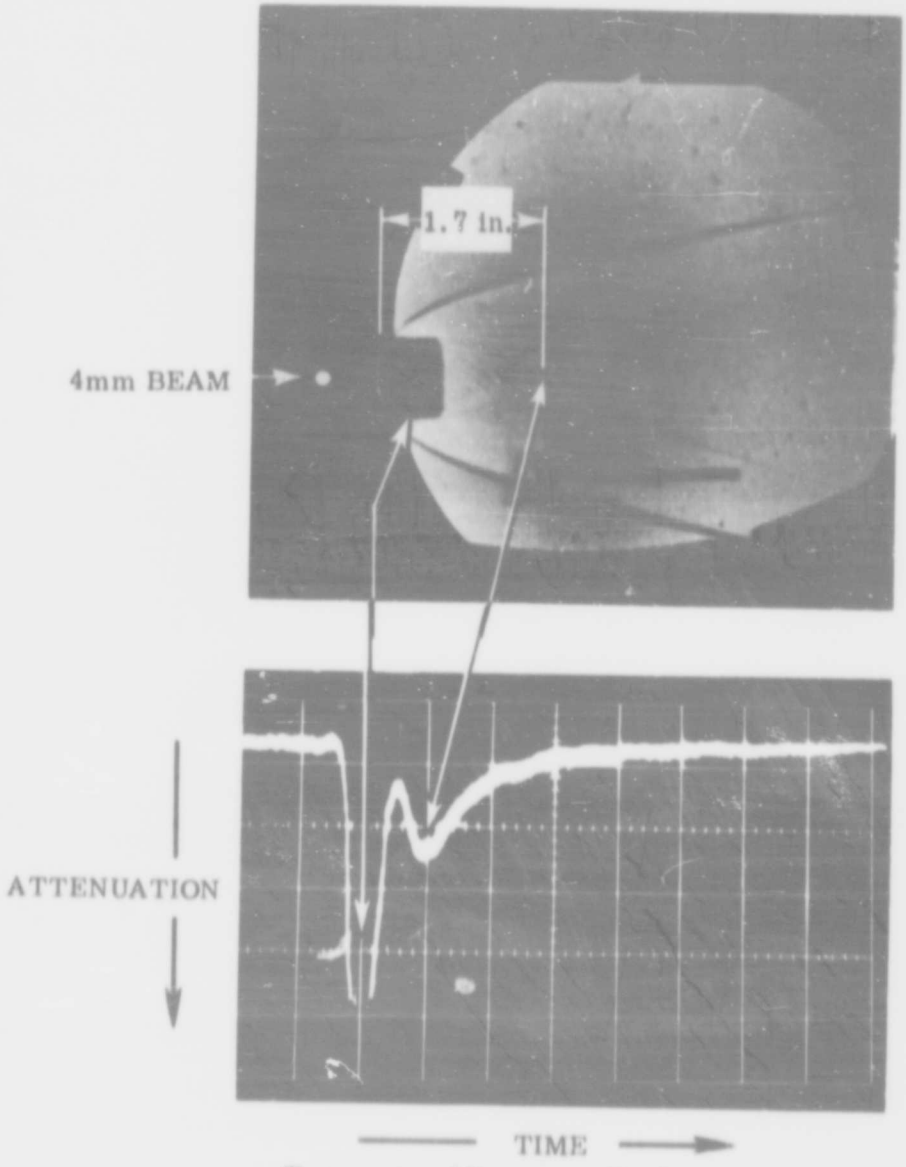

Transverse Microwave Probe:
Results with 70-Gc/s System;
V=16,100 ft/sec, P = 106mmHg-Air

Fig. 11-17 Oscilloscope Trace from the 70-Gc/s Amplitude System

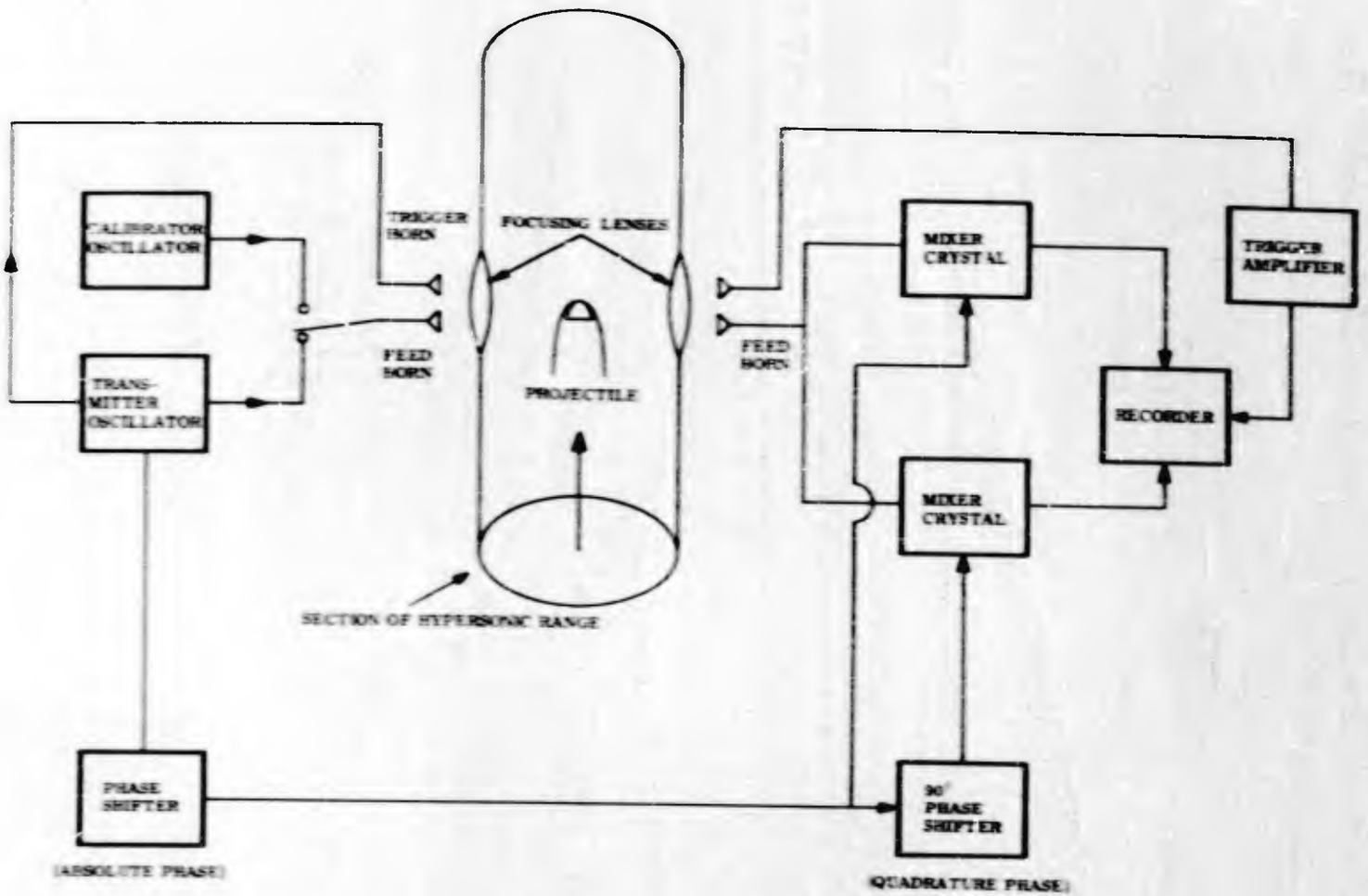

Fig. 11-18 Block Diagram of Phase-and-Amplitude System

Part of the transmitter signal is beamed through the lens system to the receiver circuitry, while part of the signal goes directly through the waveguide to the receiver as a reference signal. The level of the reference signal is very much greater than the signal transmitted through the lens system and biases the receiver diodes to operate as autodyne mixers. The signal in each transmitter beam is split into two branches and combines with the reference signal in the mixer diodes. By shifting the phase of the reference signal in one of the branches by 90°, two quadrature components of the transmitted signal are obtained. The absolute phase, that is, the angle between the signal and reference phasors, is set to the desired initial value by adjusting the phase shifter in the common reference line. With the correct initial conditions, the demodulated output can be expressed as $A(t) \sin \phi(t)$ and $A(t) \cos \phi(t)$, where $A(t)$ and $\phi(t)$ are the time-varying-amplitude and change-of-phase, respectively, of the transmitted signal. The amplitude and phase can now be derived explicitly, the former as the root of the sums of squares of the output, and the latter as the arc tangent of their ratio. The desired initial conditions are set accurately before each firing with a special calibration method which will be described in detail later.

Signal Flow Analysis -- The three basic modes of operation of the phase quadrature circuit are shown in Fig. 11-19. Case I_a describes the normal transmission mode before a firing. Case I_b covers the same mode of operation, except that the amplitude of the transmitted signal is periodically reduced so that the absolute phase can be set to a desired value in the calibration procedure. Case II describes the mode used to calibrate both the quadrature phase and the magnitude of the demodulated signal. Case III is the transmission mode used during a firing when a plasma wake is introduced in the transmission path.

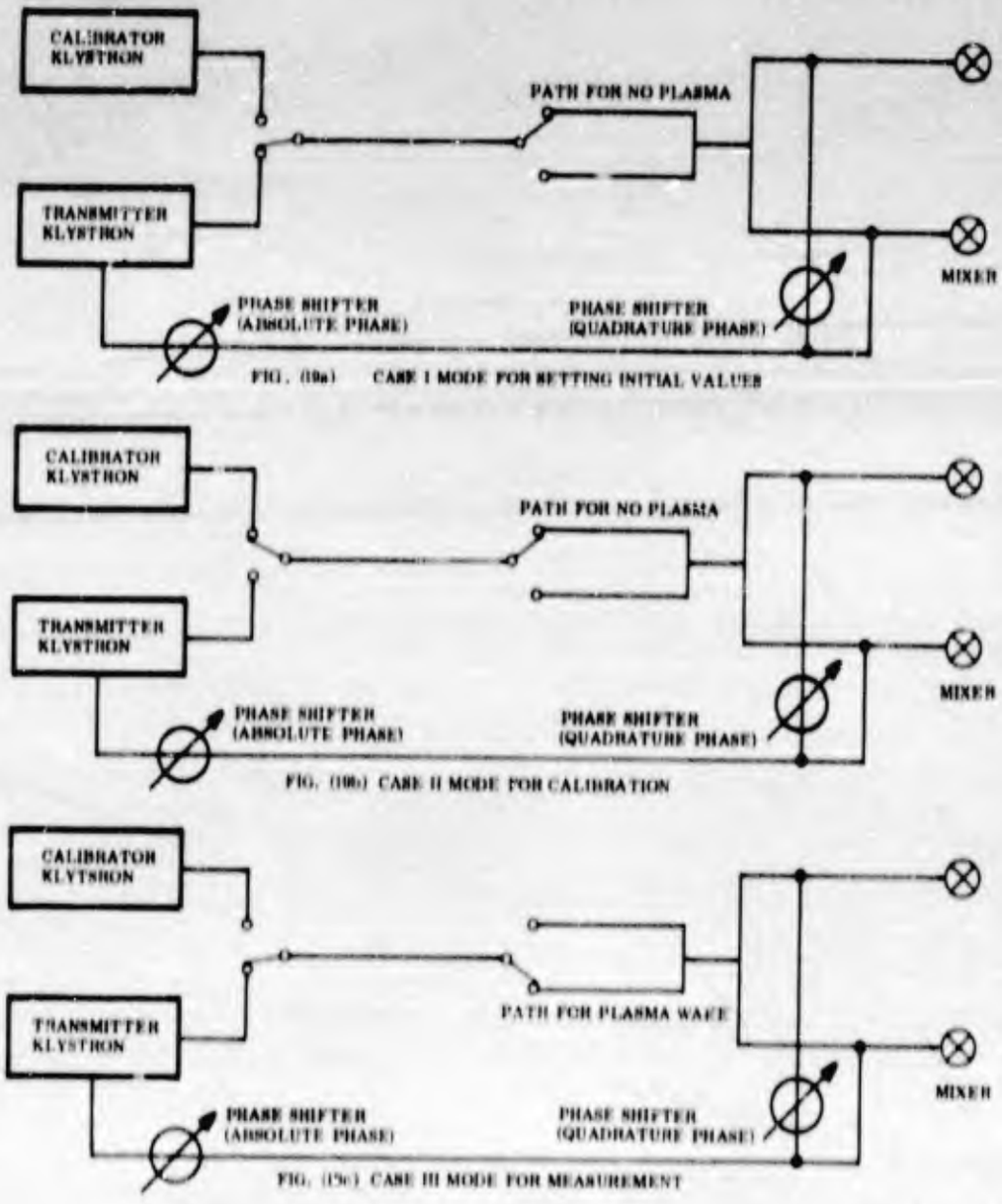

Fig. 11-19 Modes of Operation of the Phase-and-Amplitude System

In all of the above cases, the output signal which is recorded depends upon the operation of the microwave mixer. It has been shown (Ref. 9) that when the signal voltage is very much smaller than a large local oscillator voltage, the mixer transconductance g_m may be considered as a function of the local oscillator voltage only. The g_m may, therefore, be considered as periodically varying at the local oscillator frequency and may be written as a Fourier series

$$g_m = \sum_{n=0}^{\infty} a_n \cos(n\omega_o t + \phi_{rn}) \tag{1}$$

where ω_o is the angular frequency of the local oscillator, t is the time, ϕ_{rn} is the phase and a_n is the amplitude of the n^{th} component.

Consider a small harmonic or nearly harmonic signal

$$e_{sig} = E_{sig} \tag{2}$$

where E_{sig} is the constant or slowly varying amplitude, ϕ_s is the constant or slowly varying phase and ω_s is the angular frequency of the signal. The expression "slowly varying" means that, during the time for which ω_{st} changes by 2π radians, changes in both E_{sig} and ϕ_s are negligible. In fact, ϕ_s may be considered to have a slowly varying component $\phi(t)$ and constant part ϕ_{so}.

When signal (2) is applied to the mixer, the resulting alternating output current, to the first order in e_{sig}, may be written

$$i_p = g_m e_{sig} \tag{3}$$

Using Eqs. (1) and (2) in Eq. (3) and rearranging gives

$$i_p = \frac{1}{2} E_{LO} \sum_{n=1}^{\infty} a_n \left[\sin(\omega_s t + n\omega_c t + \phi_s + \phi_{rn}) + \sin(\omega_s t - n\omega_c t + \phi_s - \phi_{rn}) \right] \tag{4}$$

The total current i is the sum of the direct current I, due to the rectified bias voltage and the alternating current i_p in Eq. (4). That is,

$$i = I_0 + i_p \tag{5}$$

Output voltage of the mixer is proportional to the total current i, i. e.,

$$e_0 = K i \tag{6}$$

where K is a constant of proportionality. Using Eqs. (4) and (5) in Eq. (6) gives

$$e_0 = E_0 + \frac{1}{2} E_{LO} \sum_{n=1}^{\infty} b_n \left\{ \sin[(\omega_s + n\omega_c)t + \phi_s + \phi_{rn}] + \sin[(\omega_s - n\omega_c)t + \phi_s - \phi_{rn}] \right\} \tag{7}$$

where

$$E_0 = K I_0 \tag{8}$$

and

$$b_n = K a_n \tag{9}$$

The local oscillator frequency ω_c is always set equal to the signal frequency ω_s, and any small difference between them can be included in the slowly varying phase term. Hence, with $\omega_c = \omega_s$, Eq. (7) becomes

$$e_0 = E_0 + \frac{1}{2} E_{LO} \sum_{n=1}^{\infty} b_n \left[\sin\{\omega_s(n+1)t + \phi_s + \phi_{rn}\} + \sin\{\omega_s(1-n)t + \phi_s - \phi_{rn}\} \right] \tag{10}$$

As a low-pass filter in the mixer mount removes all microwave components of the output signal, Eq. (10) reduces to

$$e_s = E_0 + \frac{1}{2} E_{sig} b_1 \sin(\phi_s - \phi_r) \tag{11}$$

where ϕ is written for ϕ_{r1}

If an additional phase shift of $\pi/2$ radians is inserted in the reference arm of one of the receiver branches (Fig. 11-18), then, denoting the output voltage of this branch by e_c,

$$e_c = E_0 + \frac{1}{2} E_{sig} b_1 \cos(\phi_s - \phi_r) \tag{12}$$

Now denote

$$A(t) \equiv \frac{1}{2} E_{sig} b_1 \qquad A(t) = A(0) \quad \text{at } t = 0 \tag{13}$$

$$\gamma(t) \equiv \phi_s - \phi_r \tag{14}$$

where A(t) and γ(t) are constants or slowly varying functions of time.

Substituting Eqs. (13) and (14) into Eqs. (11) and (12) gives

$$e_s = E_0 + A(t) \sin \gamma(t) \tag{15}$$

$$e_c = E + A(t) \cos \gamma(t) \tag{16}$$

Case I -- Mode for Setting the Initial Values

When ω_s is constant and

$$\gamma(t) = k\pi \qquad k = 0, 1, 2, \ldots \tag{17}$$

then, with subscript 1 denoting the Case I

$$e_{1r} = E_0 \tag{18}$$

i. e., it is independent of A(t). However, since

$$\cos K\pi = \pm A(0) \tag{19}$$

(16) becomes for K odd.

$$e_{cr} = E_0 - A(0) \tag{20}$$

because A(t) retains its original value. $A(0)$.

Equations (18) and (20) are used to set $\psi(t)$ to the desired initial value $\psi(0)$ which, for convenience in photographic recording, is chosen to be $(2K-1)\pi$.

Case II – Calibration Mode

In this case, the transmitter signal to the horns is replaced by a calibration signal* of amplitude equal to that of the transmitter signal and having a frequency which differs from that of the transmitter signal by a constant frequency Ω such that

$$\Omega \ll \omega_s \tag{21}$$

The signal at the mixer is then

$$e_{sig} = E_{sig} \sin[\omega_s t + \Omega t + \phi_{sig}] \tag{22}$$

*Note: Details of calibrator to follow

where subscript II denotes Case II. A(t) retains its initial value A(0), and due to condition (21) we may regard ϕ_r in (2) for this case to be

$$\phi_r = \Omega t + \phi_{r0} \tag{23}$$

where Ωt represents the slowly varying time component $\phi(t)$ of ϕ_r. The output from the mixer is then

$$e_{rI} = E_0 + A(0) \sin [(\phi_{s0} - \phi_{r0}) + \Omega t] \tag{24}$$

Again, for the convenience in photographic recording, set

$$\phi_0 = (2k-1)\pi \qquad k = 0, 1, 2, \tag{26}$$

Then Eqs. (15) and (16) become

$$e_{rI} = E_0 - A(0) \sin \Omega t \tag{27}$$

$$e_{rII} = E_0 - A(0) \cos \Omega t \tag{28}$$

As the two signals are CW and of a frequency readily displayed on an oscilloscope, the calibration procedure for setting up the initial conditions of phase quadrature and magnitude of the deflection A(0) is greatly simplified.

The phase relationships of the quadrature signals are as illustrated in Fig. 11-20. The table of the polarities of the sine and cosine signals show how the quadrant in which the signal phasor lies is uniquely determined for $0 \leq \phi(t) \leq 2\pi$ radians. When $\phi(t) > 2\pi$ radians, it is always possible to determine the phase angle from the actual flight records by following in reverse the time variations of $\phi(t)$ which must eventually drop to zero with increasing distance behind the projectile.

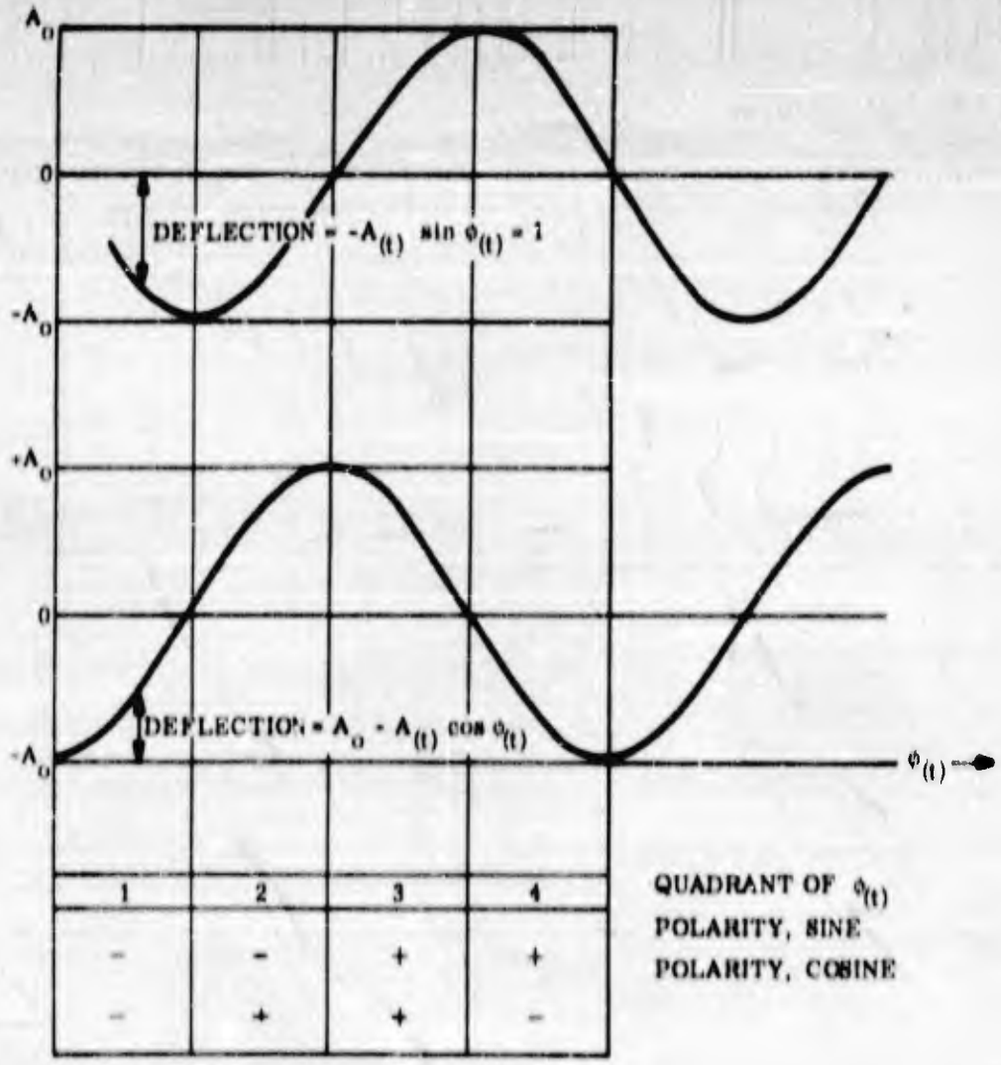

Fig. 11-20 Graphic View of Quadrature Circuit Output for $\phi(t) = \Omega t$, $A(t) = A(0)$

Case III — The Measurement Mode

When a hypersonic projectile with its ionized wake passes through the microwave beam (Fig. 11-10), the transmitted signal is time varying, in both amplitude and phase. The phase Φ_3 can be written as

$$\Phi_3 = \phi(t) + \Phi_{30} \tag{29}$$

where $\phi(t)$ is the change in phase caused by the passage of the plasma wake through the microwave beam and $\Phi(t)$ for no plasma $\Psi(t)$ is now

$$\Psi(t) = \Phi(t) + \Phi_{30} - \Phi_{\infty} = \phi(t) + \Phi_0 \tag{30}$$

Hence, Eqs. (15) and (16) become:

$$e_{3III} = E_0 + A(t) \sin [\phi(t) + \Phi_0] \tag{31}$$

$$e_{3II} = E_0 + A(t) \cos [\phi(t) + \Phi_0] \tag{32}$$

where again the subscripts refer to Case III. By repeating the choice for Φ_0 (Eq. (26)), we have, finally,

$$e_{3III} = E_0 - A(t) \sin \phi(t) \tag{32}$$

$$e_{3II} = E_0 - A(t) \cos \phi(t) \tag{33}$$

In the actual system, an oscilloscope is used to display the output of the mixers. The procedure described in Cases I and II is used to calibrate vertical deflections and initial phase-setting. Hence, this scope will, in Case III, display for the sine channel a deflection proportional to

$$e_{s\Pi} - e_{s\Sigma} = -A(t)\sin\phi(t) \tag{34}$$

and similarly, for cosine channel

$$e_{c\Pi} - e_{c\Sigma} = A(0) - A(t)\cos\phi(t) \tag{35}$$

If A(t) is set at A_0 and $\phi(t)$ denotes a linear phase-change with time, say, Ωt, the output signals would be as shown (Fig. 11-20) for the given initial phase conditions. It is evident that the sine output equals the deflection; that is, $-A(t)\sin\phi(t)$, whereas the desired cosine output

$$= -[A_0 - (e_{c\Pi} - e_{c\Sigma})]$$

$$= -\{A_0 - [A_0 - A(t)\cos\phi(t)]\}$$

$$= -A(t)\cos\phi(t)$$

It may be noted that the deflection of the trace in the cosine output as referred to the initial starting position is always positive, varying from zero for $\phi(t) = 0$ to a maximum value of 2 Ao for A(t) = A(0) and $\phi(t) = 2(k-1)\pi$ radians.

The desired quadrature signals $-A(t)\sin\phi(t)$ and $-A(t)\cos\phi(t)$ are, of course, the AC components of the time-varying transmitted signal phasor which was initially π radians out of phase with the reference phasor. The two signal components determine the total angle between the signal and reference phasors. Since this angle is π radians when $\phi(t) = 0$, π radians must be subtracted from the value of the total phase angle derived from the trace deflection.

Phase-and-Amplitude System Details -- The 35-Gc/s four-channel phase-and-amplitude-system was the first equipment put into operation

at GMDRL which was capable of measuring both phase and amplitude of the signal transmitter through a plasma wake. Since details of circuitry, calibration, operating procedure and reduction of data are very similar for the seven-channel 35-Gc/s and 70-Gc/s systems which are presently in use, the four-channel, 35-Gc/s system will be described in full; certain features and differences will be mentioned only for the seven-channel systems.

35Gc/s, Four-Channel Amplitude-and-Phase System -- The feed horn and focusing lens arrangement is unchanged from the 35-Gc/s, four-channel amplitude system, and the 1/2-in. beam widths and 1/2-in. beam centers still apply.

The transmitter circuitry is best described by referring to Fig. 11-21. Power division to the feed horns and trigger horn is as before, but additional circuitry has been added to permit the switching of a calibrator signal source to the feed horns instead of to the transmitter signal. A power monitor in the line to the feed horns, plus attenuators in both the calibrator and transmitter lines, makes it possible to equalize the two signals to a known level. A large part of the transmitter signal is used to provide both the reference signal for the receiver circuit and a reference to which the calibrator signal source is phase-locked.

The receiver circuitry for two channels is shown in detail (Fig. 11-22) indicating how the reference signal from the transmitter is split to provide a common phase reference and to bias the mixers to their correct operating points. The signal from each receiver horn is split into two branches and mixed with the reference signal, as mentioned previously. It is worth noting that phase shifters are used in reference

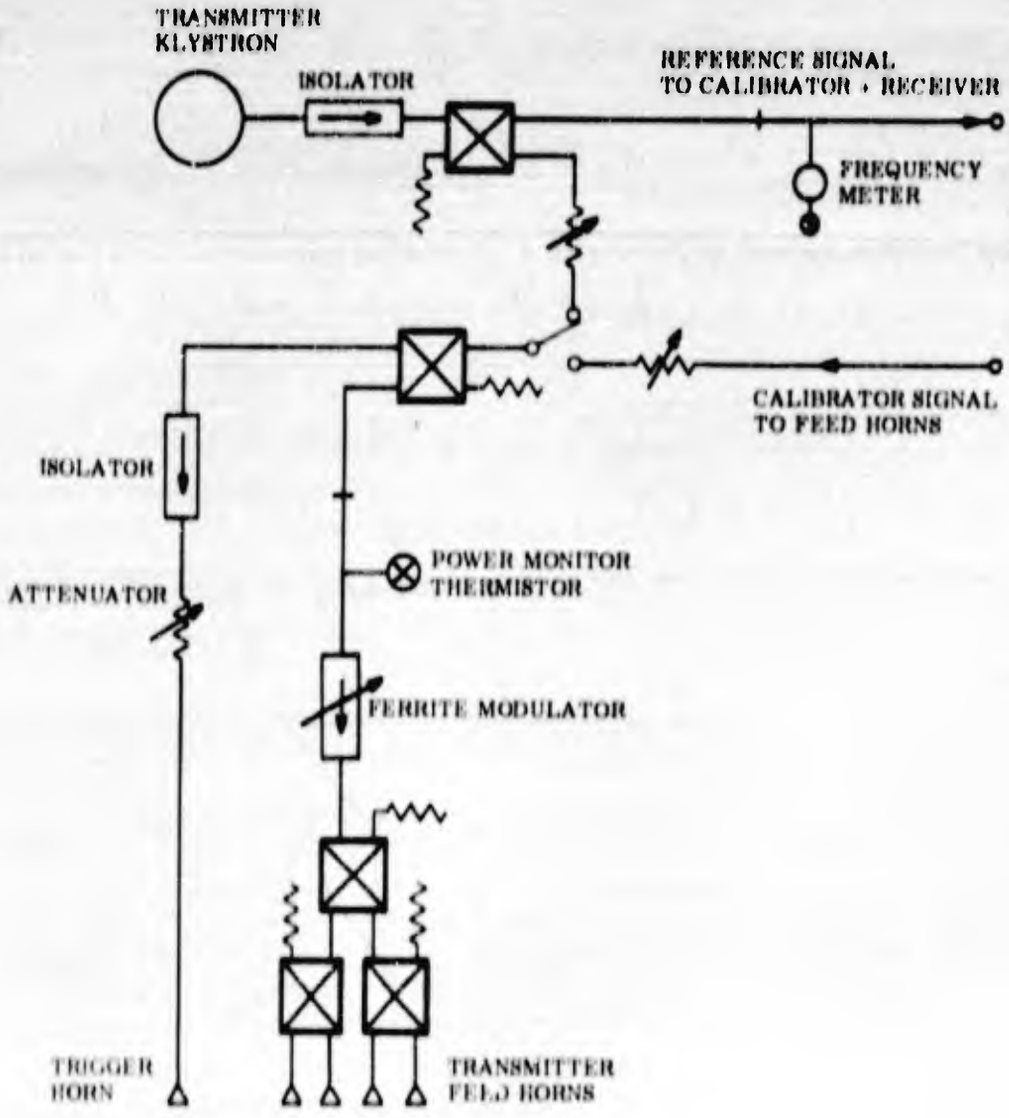

Fig. 11-21 Transmitter 35-Gc/s, Four-Channel Amplitude-and-Phase System

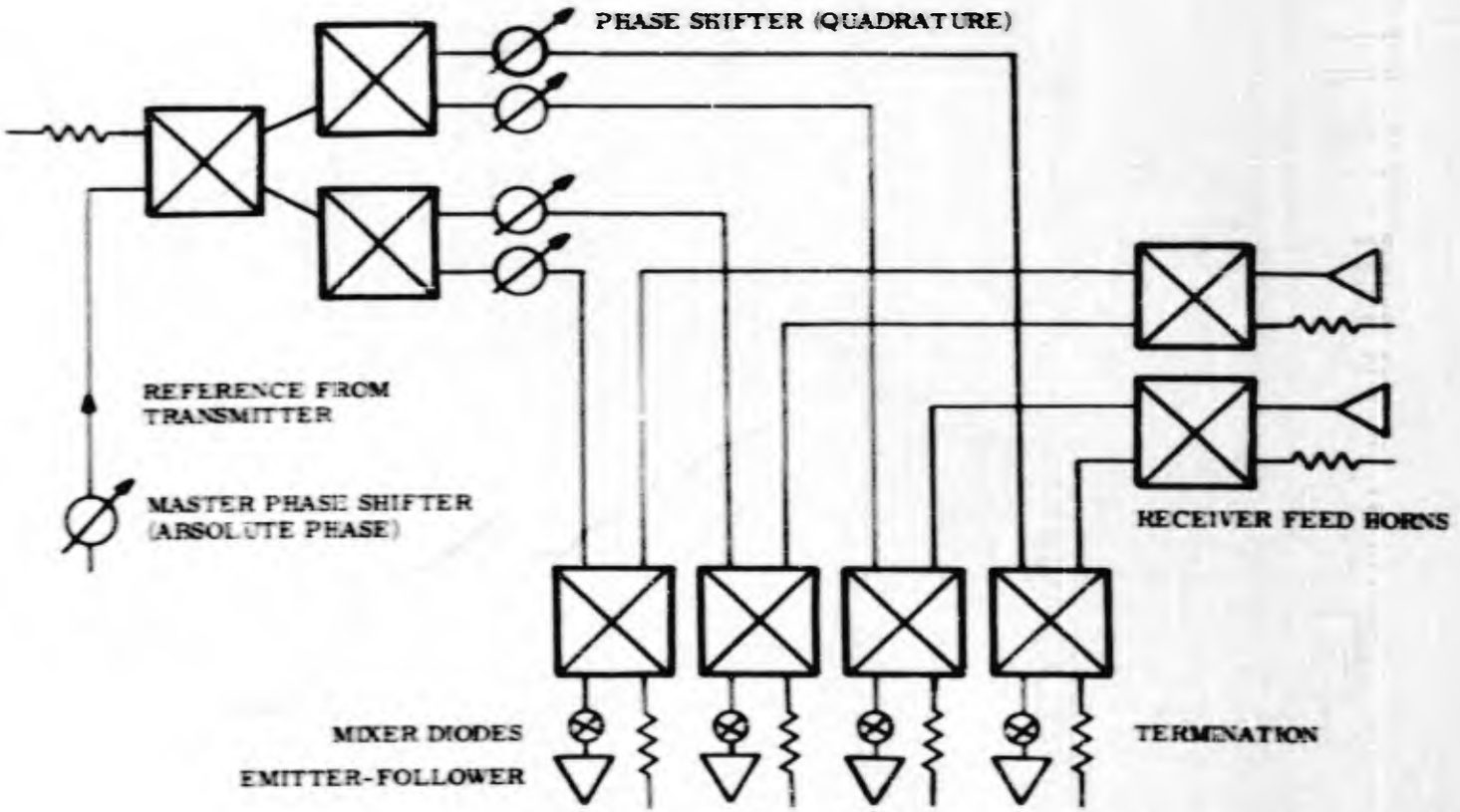

Fig. 11-22 Phase-and-Amplitude System Receiver Circuitry for Two Channels

lines which go to both branches of the received signal. This is necessary to ensure that not only is the relative phase between the two branches of a given signal channel in quadrature, but that the same phase with respect to the reference signal is maintained in all four branches representing the sine and cosine components of the transmitted signal. Special phase shifters, made at Defense Research Laboratories, meet the requirement of total phase adjustment of greater than 360° with a VSWR less than 1.15 while conforming to limited physical size and configuration.

An emitter-follower is mounted on each mixer-holder to match the impedance of the mixers to a long transmission cable which is used to transmit the output signals to the recording oscilloscopes. Dual-beam Tektronix 551 oscilloscopes are used to display the phenomena, with the upper trace recording the sine component and the lower trace the cosine component of the transmitted signal. The amplified signal triggers the oscilloscope, a result of the interruption of the trigger fan beam by the projectile. Photographic records of the oscilloscope display are taken on Polaroid film with cameras operated remotely from the control room.

Calibration -- The most essential requirement of the calibration is that the initial phase-and-amplitude conditions be set to give a suitable display which can be readily analyzed. The relative phase of the signals in the branches of a given channel must be set in quadrature to get the sine and cosine components of the output signal; also, the sine and cosine components in all the channels must have the same phase relationship with respect to the reference signal. The absolute phase ϕ_o, that is, the arbitrary phase between the transmitted signal vector and the reference vector, must be set to some convenient value -- chosen

to be $(2n-1)\pi$ radians. The amplitude Ao must also be set for all channels to give a known deflection on the oscilloscope.

The quadrature phase and amplitudes are set by the use of a calibrator signal-source which is phase-coherent but offset in frequency from the transmitter source by a small amount, say, 1 mc. When this calibrator signal (set to the same power level) is substituted for the transmitter signal which is going to the feed horns while part of the transmitter signal source is still used for the phase reference signal, the output is a simulated pure phase shift which is changing linearly with time. This CW signal is readily displayed and permits adjustment of the peak-to-peak deflection (2 Ao) and the phase quadrature.

The absolute phase ϕ_o, that is, the arbitrary phase difference between the transmitted and reference signal, is set by periodically cutting off the transmitter signal in the configuration mentioned previously (Case I). The outputs on the sine and cosine displays are rectangular pulses whose amplitudes depend on the value of ϕ_o. For $\phi_o = n\pi$, the magnitude of deflection in the sine component is zero and is Ao in the cosine component. ϕ_o is set at $(2n-1)\pi$ by observing the polarity of the deflection in the cosine channel.

At present, a mechanical chopper, made from a small four-bladed fan with microwave absorber covering a flat metal sheet, is used to cut off the beam periodically at the receiver feed horn. This method is expected to be replaced by a ferrite modulator having a high on-off ratio placed in the common line to the transmitter feed horns.

Description of Calibrator -- The generation of the calibrator signal is based on the use of another klystron which is phase-coherent to, but offset by a small difference frequency, from the transmitter klystron. This technique has been used previously for a different purpose[Ref. 9].

The operation of the circuitry is best described by referring to Fig. 11-23. A reference signal from the transmitter klystron is used to generate a single sideband signal. As 30-Mc IF amplification is used in the phase-locking loop, the sideband modulator is set at 30 Mc + Δ f – Δf being the desired difference frequency between the transmitter and calibrator klystrons. For the 35-Gc/s system, the upper sideband [(35 Gc/s + (30Mc + Δf)] is mixed with the output of the calibrator klystron in a balanced mixer. When the frequency of the calibrator klystron is at 35 Gc/s + Δf, the mixer output is 30 Mc. The amplified 30-Mc signal is compared with a 30-Mc reference signal in a phase detector. The output voltage from the phase detector is applied to the repeller of the calibrator klystron to keep it phase-locked at 35 Gc/s + Δ f.

As the modulator which drives the single sideband generator can be varied in frequency, Δ f can be varied from 0 – 10 Mc. This feature makes it possible to make a rapid and accurate over-all frequency response of the receiver and recording equipment.

Operating Procedure -- A careful calibration of the system is made before each firing; this procedure will be outlined next.

After a suitable warmup period, the transmitter klystron is accurately set to the desired frequency – 35.0 Gc/s for this equipment. The calibrator klystron is then phase-locked at 1 Mc above this frequency.

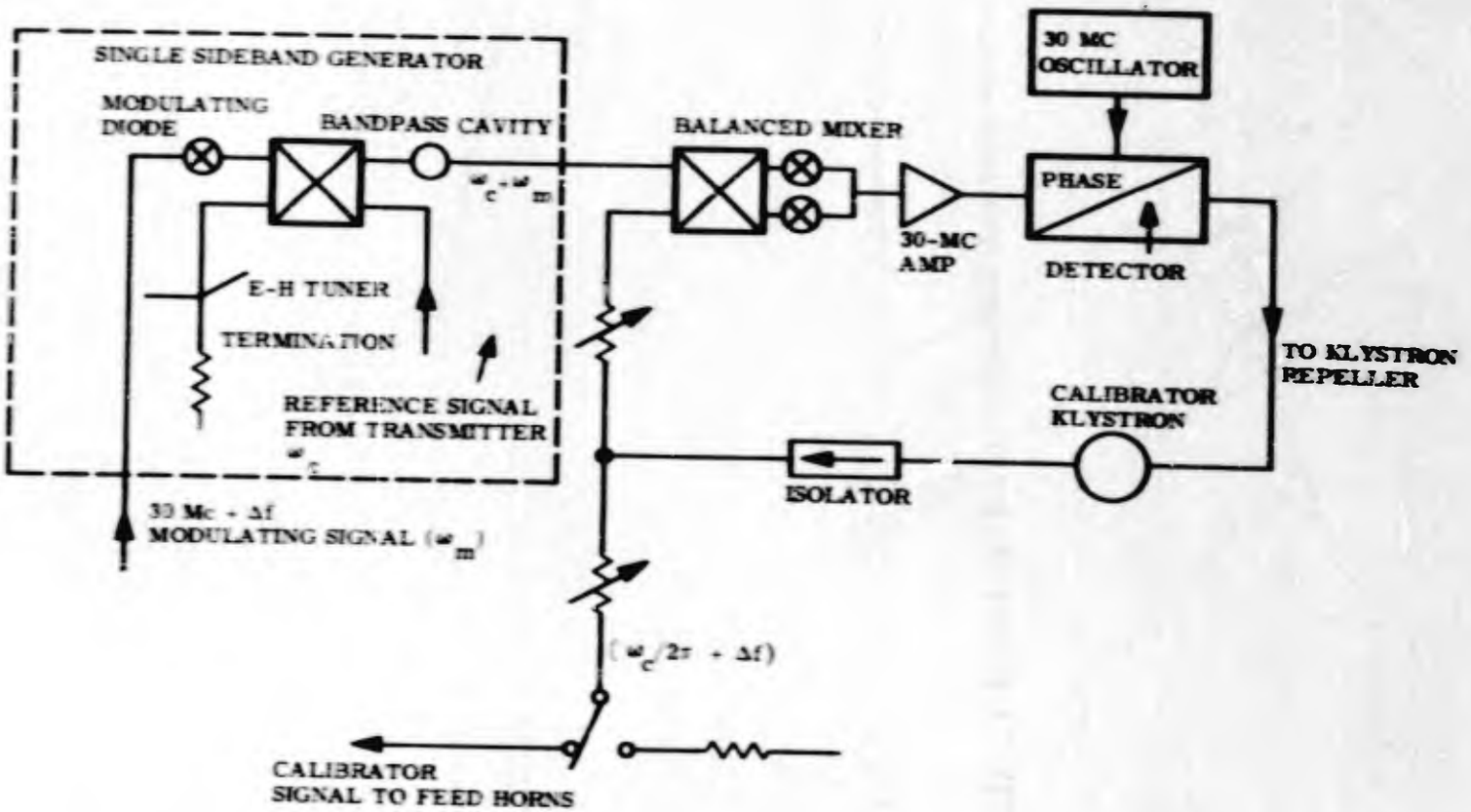

Fig. 11-23 Calibrator Circuit-35-Gc/s, Four-Channel Phase-and-Amplitude System

The transmitter power in the reference line is set to bias each mixer at a level of approximately 0.5 mw, while the part going to the feed horns is adjusted so that the level of the transmitter signal at the mixer is approximately 1 μw . The calibrator signal to the feed horns is also set to this level by switching the signal sources and equalizing the power at a monitor point in the feed line.

With the calibrator signal switched into the feed line, there are two 1-Mc signals for each probe channel. As the power division of the hybrids and the mixer efficiencies are not perfectly matched, the small differences in the output amplitudes of the signals are equalized by adjusting the gain controls of the oscilloscope preamplifiers. The peak-to-peak deflection for each trace on the oscilloscope is limited to 4 cm, and this is the value used for most records. This sets the value of Ao = 2 cm, since the level of the transmitter and calibrator signals to the feed horns has been previously equalized. The trace width in this case sets the lower limit to the measurable electron concentration to approximately 10^{11} e/cc. When data from the far wake where electron concentrations are of this order or less is desired, the deflection for Ao is increased by some known factor to permit reading of smaller phase changes. This technique has permitted measurements of electron concentrations in the order of 10^{10} e/cc.

To set the quadrature phase of all the channels, the relative phase between the signals of equal amplitude in the sine and cosine traces in a master channel are set by adjusting the waveguide phase shifters in the reference branch arms so that the phase of the cosine signal accurately leads that of the sine signal by 90°. The sine and cosine signals of this master channel are now used as a reference to which the phase of the respective sine and cosine signals of all the other channels

are equalized. At present, the oscilloscope display of the traces is used to determine the relative phase of the two components. The phase can be set to within a few degrees with this method, but improved techniques are planned for increasing accuracy.

After the amplitude and quadrature phase has been set, the feed line is switched back to the transmitter klystron to adjust the absolute phase ϕ_o. The mechanical chopper is placed just ahead of the receiver feed horns, and the phase shifter in the common reference line is adjusted so that there is minimum change in the sine trace but positive deflection of magnitude Ao in the cosine trace when the beams are cutoff.

With a checkout of the trigger system, and the setting of the oscilloscopes for photographic recording of the phenomena, the calibration is complete.

Data Reduction -- A typical data record is shown in Fig. 11-24 to illustrate the data reduction procedure. The grid represents the graticule of the oscilloscope face, and the lines are 1 cm apart. Four traces are recorded — the sine and cosine signals, and the reference lines for the sine and cosine signals. The reference traces are recorded as a double exposure immediately after the signals have been recorded and is used to facilitate the reading of the deflections of the traces. Use of the graticules as reference is not too satisfactory because of parallax problems and because the traces are not necessarily accurately parallel to the graticule. In fact, the traces are sometimes slightly curved due to beam distortion at the maximum vertical positions of the traces as at the cosine reference line. Reading of the difference in the deflection between the signal and reference traces reduces errors from these sources.

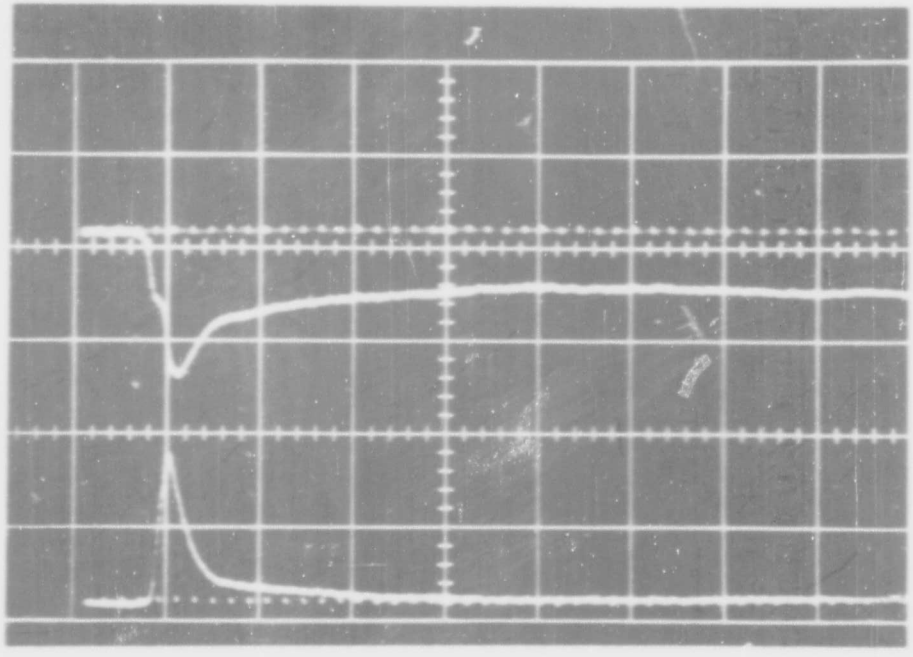

Fig. 11-24 A Typical Oscilloscope Record from the Amplitude-and-Phase System Identifying the Traces and Data Points

The data records are read on a Telecomputing Corporation Universal Telereader, and the readout is in the form of punched cards (IBM). A projection system is used to magnify the record 10 times in order to improve reading accuracy. Readings are made by positioning adjustable perpendicular crosshairs so that they intersect at a desired data point. The readout from the vertical and horizontal crosshairs are then the X and Y coordinates, respectively, of that point with respect to some reference. This is because the X and Y readouts are directly proportional to the excursion of the crosshairs on the screen giving 417 counts/in.

As a first step in the reading, the horizontal crosshair is aligned so that it is parallel with the reference trace. The Y readout is zeroed with the horizontal crosshair slightly below the cosine reference trace, while the X readout is zeroed at the start of the traces. At any given X setting of the vertical crosshair, four Y readings are taken -- Y_1, Y_2, Y_3 and Y_4. This gives time-coincident readings of the sine and cosine deflections. The spacing of the readouts depends on signal variations, with a large number of readings evident when the signals are changing rapidly, and fewer where the changes are small. In fact, where ionization is high enough to produce large phase shifts, the readings must be close enough in that part of the trace which is recording the phenomena near the projectile so that the change in the computed phase is not greater than 180°; otherwise, ambiguities in the determination of the quadrant in which the signal vector lies will arise.

The X and Y readouts are normalized in terms of counts/cm by taking, say, the counts for 4 cm in the Y axis to set the vertical scale factor for 2Ao, and the counts for, say, 4 cm in the X axis to set the horizontal scale factor. As the sweep spread of the oscilloscope is

calibrated in sweeptime, the X readout is related to the time from the start of the trace. From this we can see that

$$\frac{Y_4 - Y_3}{\text{counts for } A_0} = \frac{\text{sine deflection}}{A_0} = -\frac{A(t)}{A_0}\sin\phi(t)$$

$$\frac{Y_2 - Y_1}{\text{counts for } A_0} = \frac{\text{cosine deflection}}{A_0}$$

But from the signal analysis

$$-\frac{A(t)}{A_0}\cos\phi(t) = -\frac{1}{A_0}\left[A_0 - \text{cosine deflection}\right]$$

$$= -\left[1 - \frac{Y_2 - Y_1}{\text{counts for } A_0}\right]$$

then

$$\phi(t) = \arctan\frac{(Y_4 - Y_3)/\text{counts for } A_0}{1 - (Y_2 - Y_1)/\text{counts for } A_0} - \pi$$

and

$$\frac{A(t)}{A(0)} = \left\{\left(\frac{Y_4 - Y_3}{\text{counts for } A_0}\right)^2 + \left[1 - \frac{(Y_2 - Y_1)}{\text{counts for } A_0}\right]^2\right\}^{1/2}$$

These relations are derived from the cards in a computer. To get a feeling for the order of magnitude of the radial and axial variations in the electron concentrations in the wake, the program was written to compute the electron concentration as a function of distance from the shock front of the projectile. Rather strong assumptions were made to simplify the program. The first is that each of the four beams is passing a slab of constant thickness equal to the projectile diameter and of uniform distribution across the slab. The observed total phase shift then gives a measure of the electron density in each of the slabs and gives a good estimate of the radial and axial density variations in the wake. The other assumption made is that the collision frequency is

low enough to be neglected in the derivation of the electron density from the measured phase shift. In most of the firings, observed errors due to this latter assumption are serious in only a small region in the near wake.

Output from the computer was in the form of both printout and plots of the normalized transmitted signal amplitude ratio and the ratio of electron density to the critical density, both as a function of distance from the shock front.

Typical Results -- The initial reduced data from the four-channel records of the 35-Gc/s phase-and-amplitude system showing the amplitude ratio and the normalized electron density as a function of distance is presented in Fig. 11-25.

Further analysis of the data is in progress and is being reported under a separate title[Ref. 11].

35-Gc/s Seven-Channel Phase-and-Amplitude System -- During the operation of the four-beam, 35-Gc/s phase quadrature, it was observed that considerable differences existed in the adjacent channel response of the 70-Gc/s systems in the recompression region. These effects were often lost in the 35-Gc/s system, partly due to the lower resolution of the 1/2-in. beams, and partly due to the phenomena of interest passing between two beams which are at 1/2 in. centers. To improve the data acquisition capabilities of the 35-Gc/s system while permitting direct comparison of the measured quantities with the results of a 70-Gc/s beam observing the wake along the same axis, the number of channels was increased to seven with the beams staggered to have beam centers 1/4 in. apart. The ideal disposition of beams for

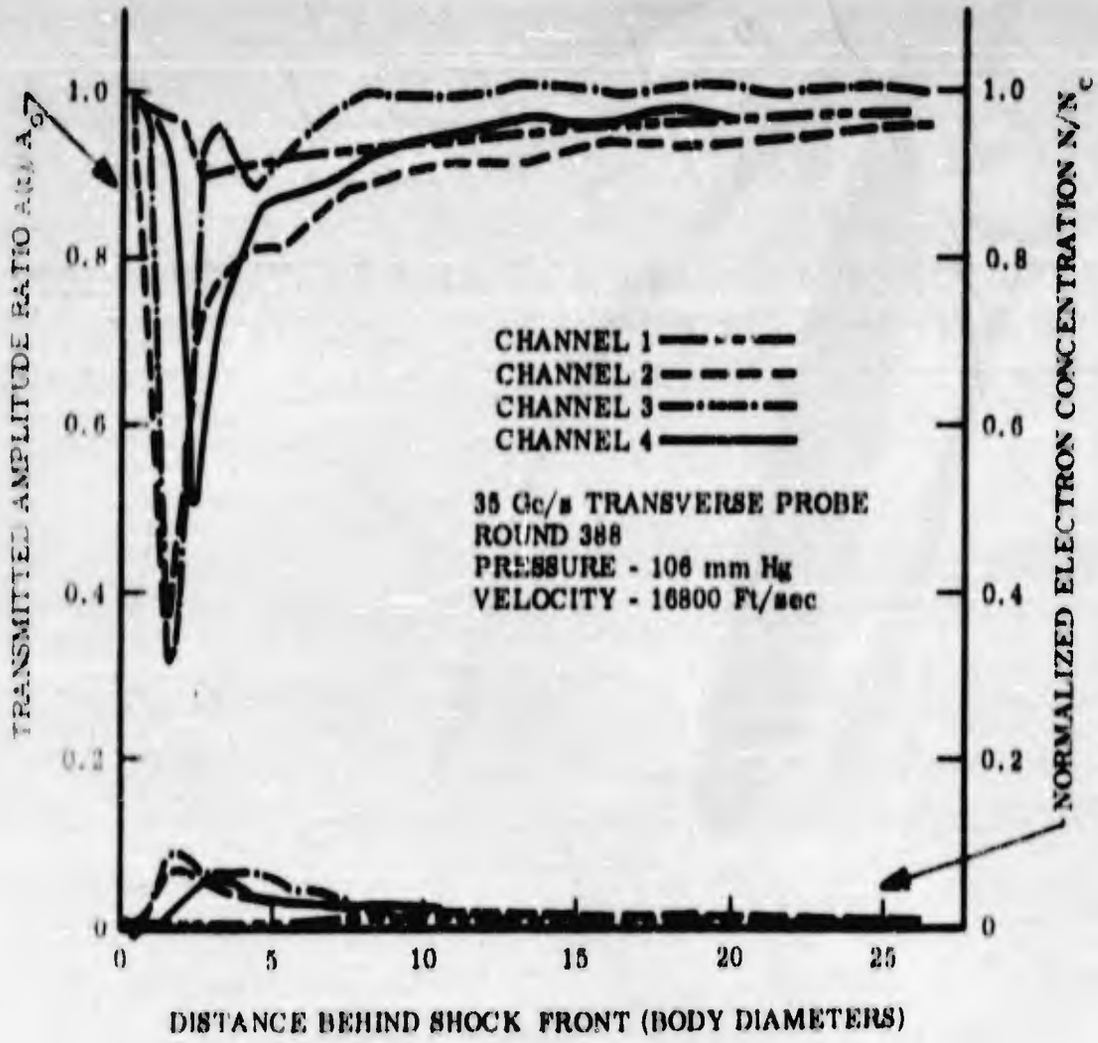

Fig. 11-25 Typical Result of 35-Gc/s, Four-Channel Phase-and Amplitude System

the 35-Gc/s and 70-Gc/s seven-beam systems is shown in Fig. 11-12 where the beams of a given channel in the 35-Gc/s and 70-Gc/s systems make measurements along the same part of the wake.

The basic circuitry and method of operation are essentially the same as for the four-channel amplitude-and-phase system. There are some differences in the circuit details and configuration — partly to accommodate the increased number of channels, and partly to improve or simplify operating procedure.

The transmitter circuitry is shown in Fig. 11-26. The method by which the transmitter and calibrator signals are switched to the feed horns and equalized in power with the DPDT waveguide switch can be readily seen. This switch can be operated from the receiver side where the operator does most of the calibration. The trigger horns for both the 35-Gc/s and 70-Gc/s systems are energized from this transmitter but otherwise provide independent triggering for each system as the projectile interrupts their respective trigger beams. Isolators are used in the lines to each trigger-horn source to prevent signals reflected from the projectile from being coupled to the second trigger system. A ferrite modulator in the common trigger line is pulsed prior to a firing to simulate interruption of the beams by a projectile, thus ensuring a complete trigger system checkout.

By comparison with the 35-Gc/s, four-channel system, the receiver circuitry is changed only in channel capacity and configuration. Although the principle of operation of the calibrator remains unchanged, the method of single sideband generation has been changed to the phase discrimination circuit[Ref. 12]. Figure 11-27 shows the basic operation

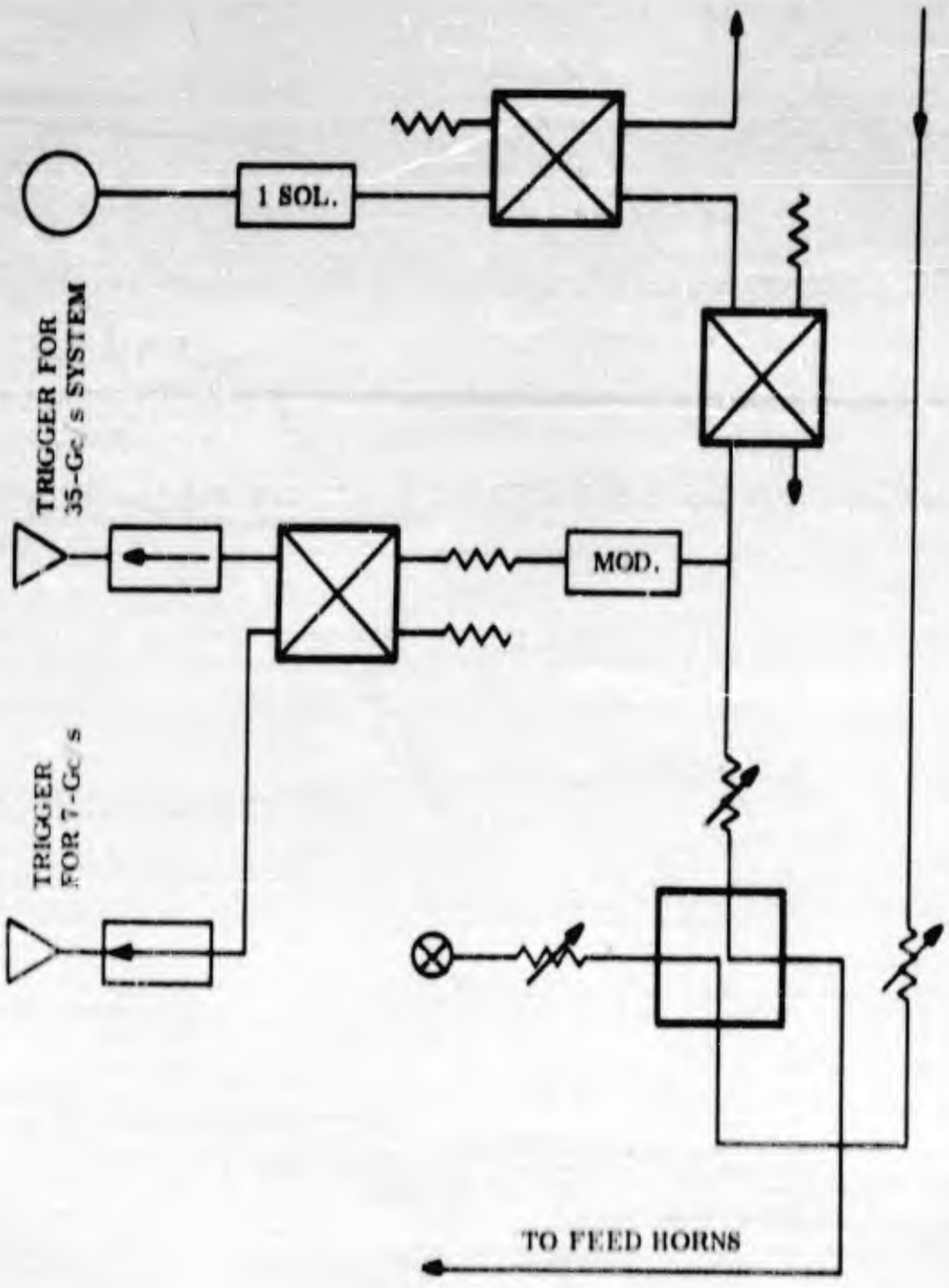

Fig. 11-26 Transmitter 35-Gc/s, Seven-Channel Phase-and-Amplitude System

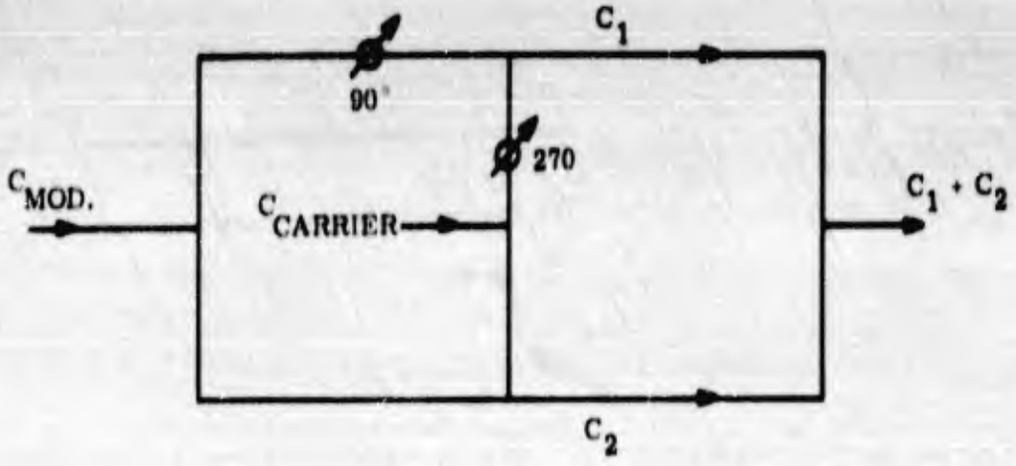

Fig. 11-27 Single Sideband Generator

where

$$e_1 = \frac{E_m}{2} \sin\left[\left(\omega_s t + \frac{3\pi}{2}\right) + \left(\omega_m t + \frac{\pi}{2}\right)\right] + \frac{E_m}{2} \sin\left[\left(\omega_s t + \frac{4\pi}{2}\right) - \left(\omega_m t + \frac{\pi}{2}\right)\right]$$

$$= \frac{E_m}{2} \sin(\omega_s + \omega_m)t - \frac{E_m}{2} \sin(\omega_s - \omega_m)t$$

$$e_2 = \frac{E_m}{2} \sin(\omega_s + \omega_m)t + \frac{E_m}{2} \sin(\omega_s - \omega_m)t .$$

$$e_1 + e_2 = E_m \sin(\omega_s + \omega_m)t$$

is the desired upper sideband, where $\omega_s/2\pi$ is the carrier frequency, and $\omega_m/2\pi$ = 30 Mc ± Δf.

The detailed circuit of the calibrator (Fig. 11-28) is essentially the same as that shown in Fig. 11-23, except for the single sideband generator which is blocked out in dashed lines.

Data Reduction — 35-Gc/s Seven-Channel Amplitude and Phase -- Although the basic procedure in this data reduction is the same as for the four-channel, 35-Gc/s system, there are some differences which will be outlined below.

Time markers from a controlled crystal oscillator are now used to intensity-modulate the reference traces. This makes it possible to adjust the relative starting positions of the two traces so that a vertical line passing through time-coincident points in the two trace is accurately perpendicular to the reference lines. Since an external trigger is also generated by the marker generator, it is possible to correlate data at a given time from different channels. The markers are used also to give a more accurate horizontal scale factor, since there is no error due to parallax.

Because a more complex computer program is being written to derive the radial variation in electron density by the method described in section 3. 4, the computer plots of the initially reduced data have been changed to present the amplitude ratio and the total phase shift. These quantities are derived from actual measurements and are not subject to the assumptions regarding the plasma properties, as was the case for the previous plot of the electron concentration.

Typical multichannel plots of the seven-channel, 35-Gc/s amplitude-and-phase system are shown in Fig. 11-29a and 11-29b.

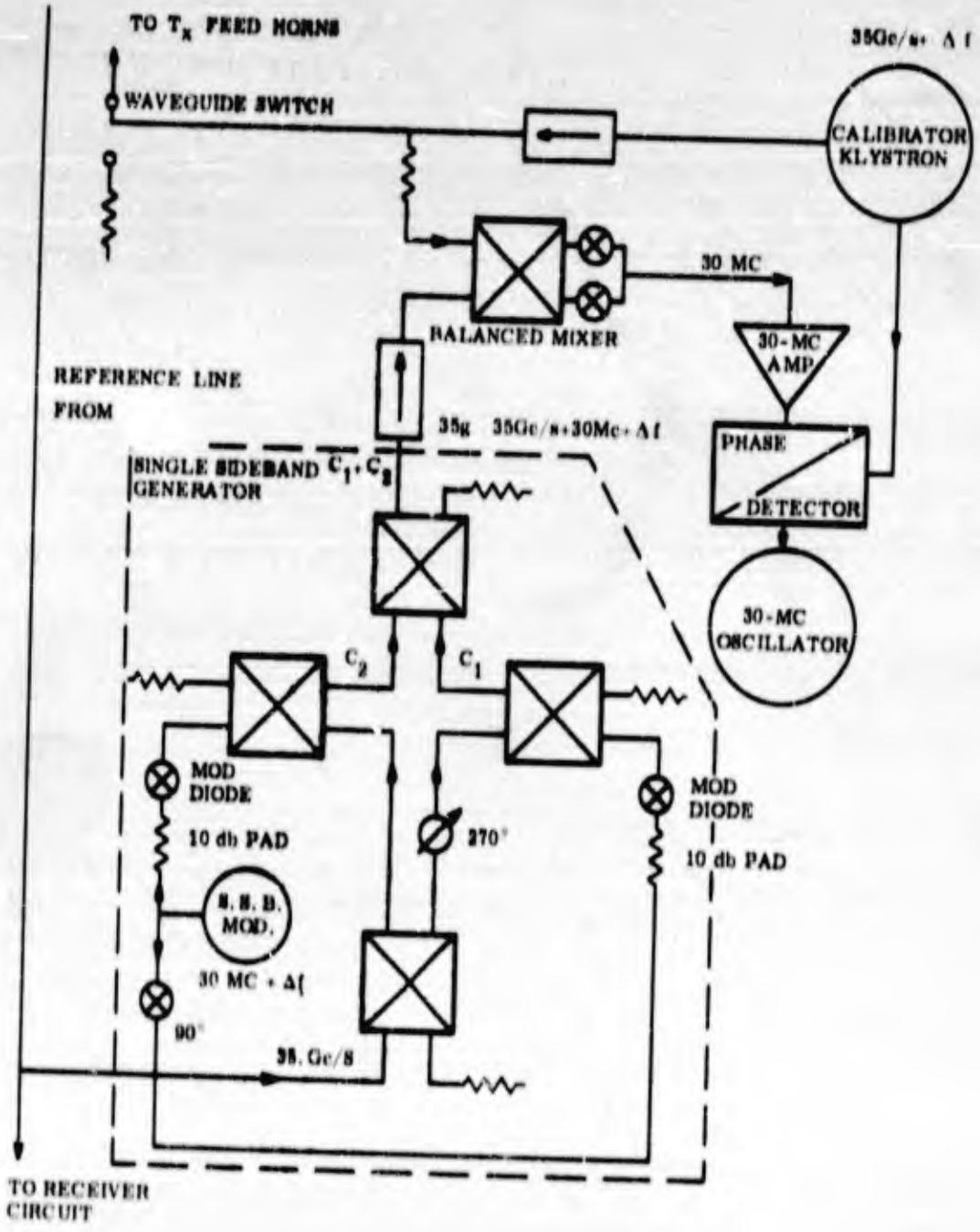

Fig. 11-28 Calibrator Circuit of Seven-Channel Phase-and-Amplitude System

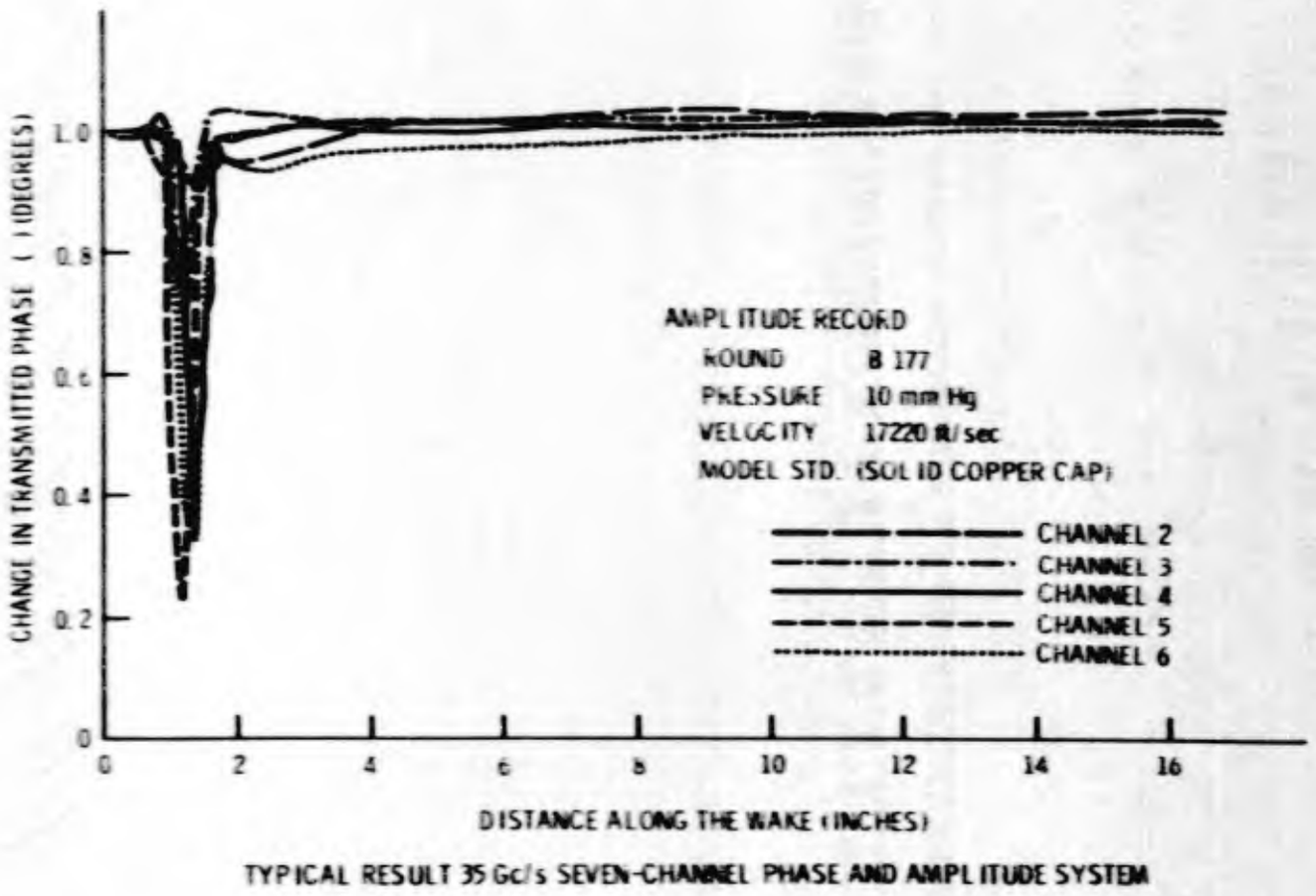

Fig. 11-29a Typical Results 35-Gc/s, Seven-Channel Phase-and-Amplitude System

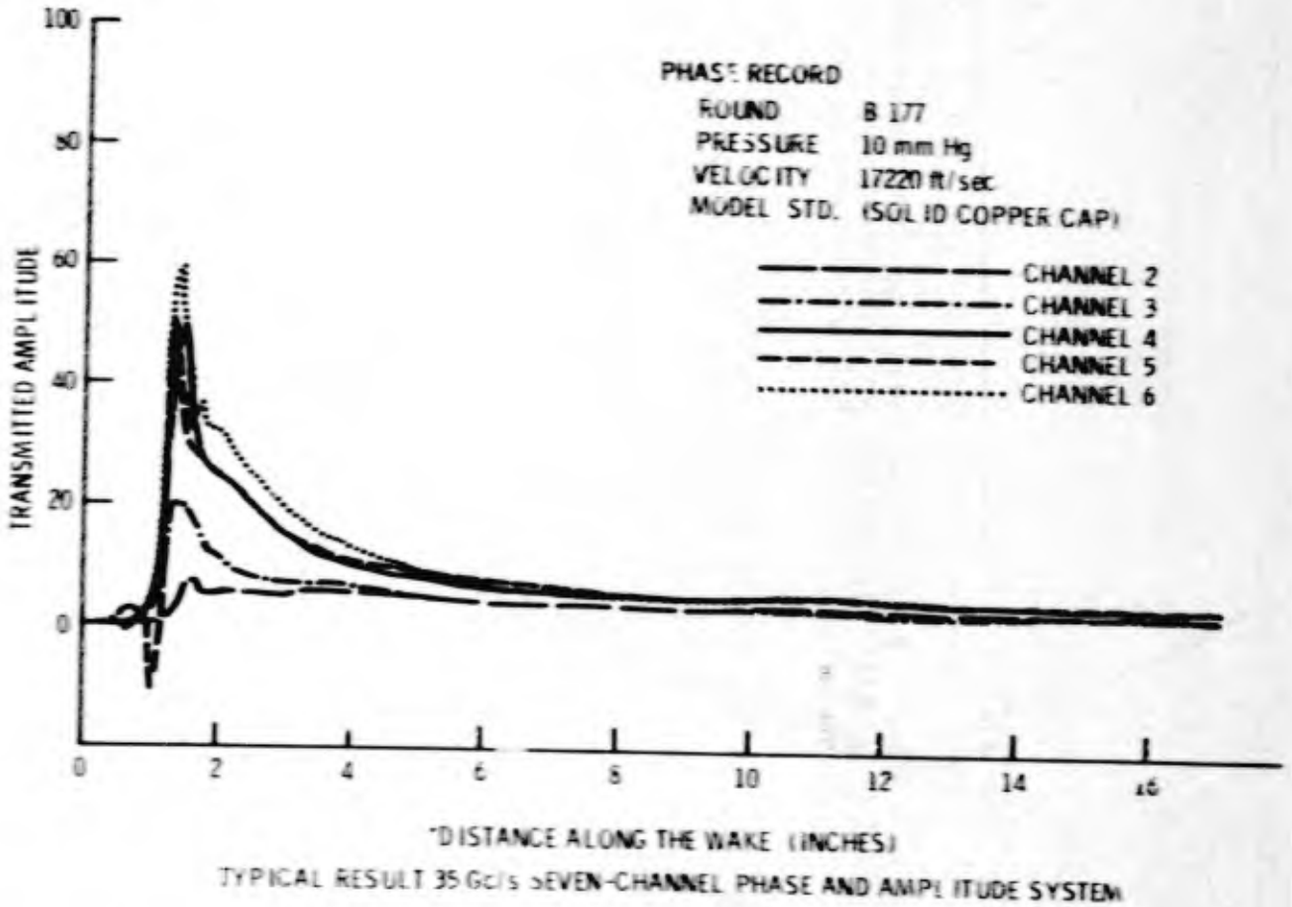

Fig. 11-29b Typical Result 35-Gc/s, Seven-Channel Phase-and-Amplitude System

70-Gc/s Seven-Channel Phase and Amplitude System -- An over-all view of the installation on the hypersonic range of the 70-Gc/s, seven-channel phase-and-amplitude system is shown together with the 35-Gc/s system in Fig. 11-30.

The focusing system is unchanged from that for the 70-Gc/s amplitude system, and the beam properties are as described previously. The circuitry to record the quadrature components of the transmitted signal, the operating procedure, and data reduction is essentially the same as for the 35-Gc/s channel phase-and-amplitude system.

The only difference in the transmitter circuit is that the trigger takeoff is absent as the trigger source is supplied from the 35-Gc/s system. In the receiver circuitry, the wide variation in the characteristics of the mixer diodes (Philco 1N2792) made it necessary to use waveguide attenuators at the output of each of the receiver feed horns to permit coarse equalization of the output signal levels.

The lower output signals from the mixers made it necessary to use additional amplification ahead of the oscilloscope input to obtain the necessary deflection of the traces. Transistorized video amplifiers were developed chiefly to meet the requirement of flat frequency response (within 1/2 db between 150 cps – 6 Mc), good transient response, and 50-ohm input and output impedance.

The single sideband generator circuit identical to that used in the seven-channel, 35-Gc/s phase-and-amplitude system was initially tested for use in the 70-Gc/s system. The change from the circuitry used in the four-channel, 35-Gc/s system was necessary, since a bandpass cavity with a high enough to suppress the lower sideband

Fig. 11-30 Overall View of Seven-Channel, 70-Gc/s and 35-Gc/s Phase-and-Amplitude Systems

(of the two sidebands which are separated by approximately 62 Mc at 70-Gc/s) was not readily available. The other difficulty was the mechanical and electrical stability required to maintain the lower sideband suppression.

The present system is very easy to set up and requires virtually no adjustment by the operator.

The operating data reduction procedures are the same as for the seven-channel, 35-Gc/s phase-and-amplitude system.

Typical multichannel results from the 70-Gc/s phase-and-amplitude system are shown in Figs. 11-31a and 11-31b. Figure 11-31a shows the ratio of the transmitted signal amplitude, and Fig. 11-31b the change in the phase of the transmitted signal, both plotted against distance along the wake. The scale drawing of the model in flight shows the relative positions of the focused beams with respect to the wake.

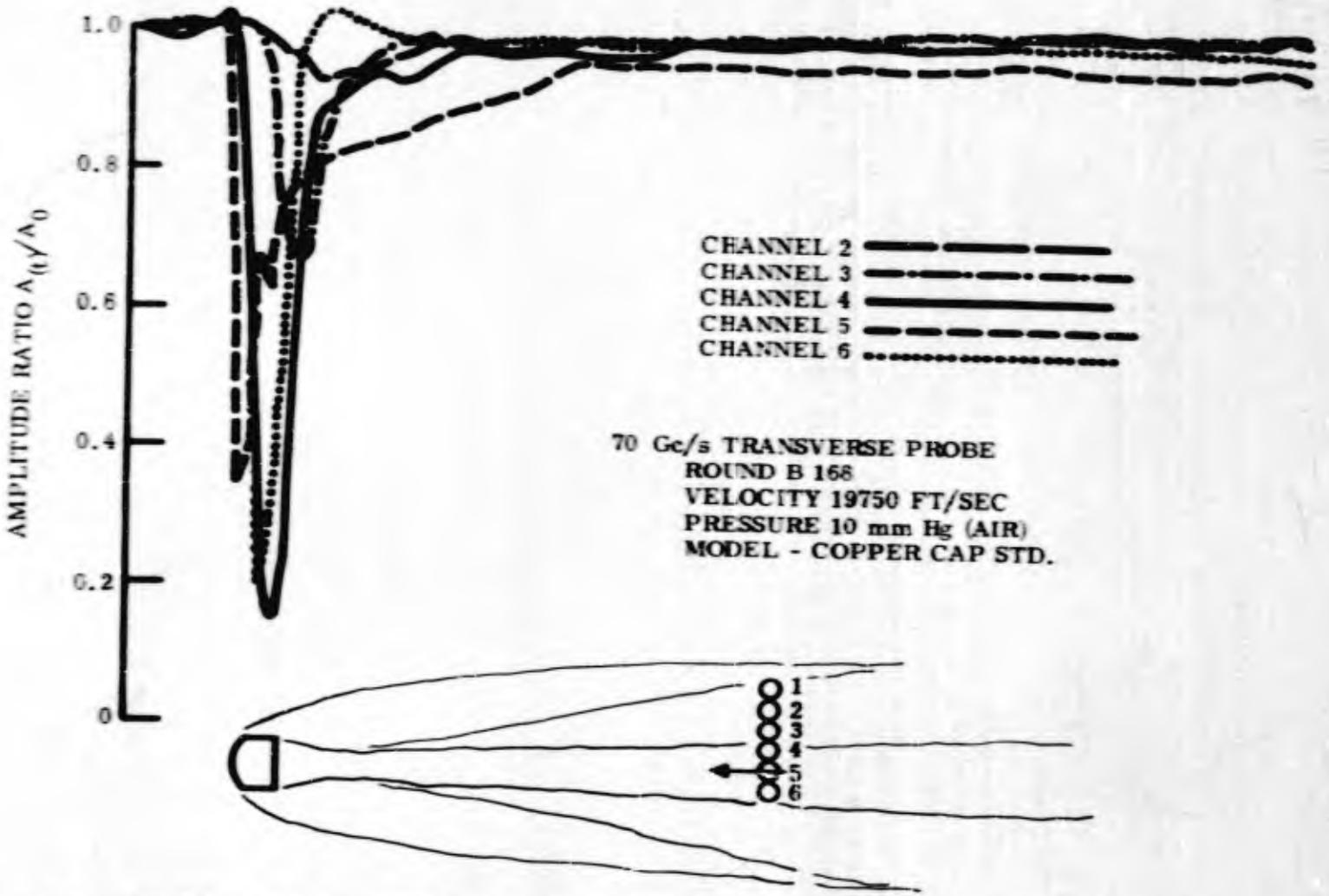

Fig. 11-31a Typical Result 70-Gc/s, Seven-Channel Phase-and-Amplitude System

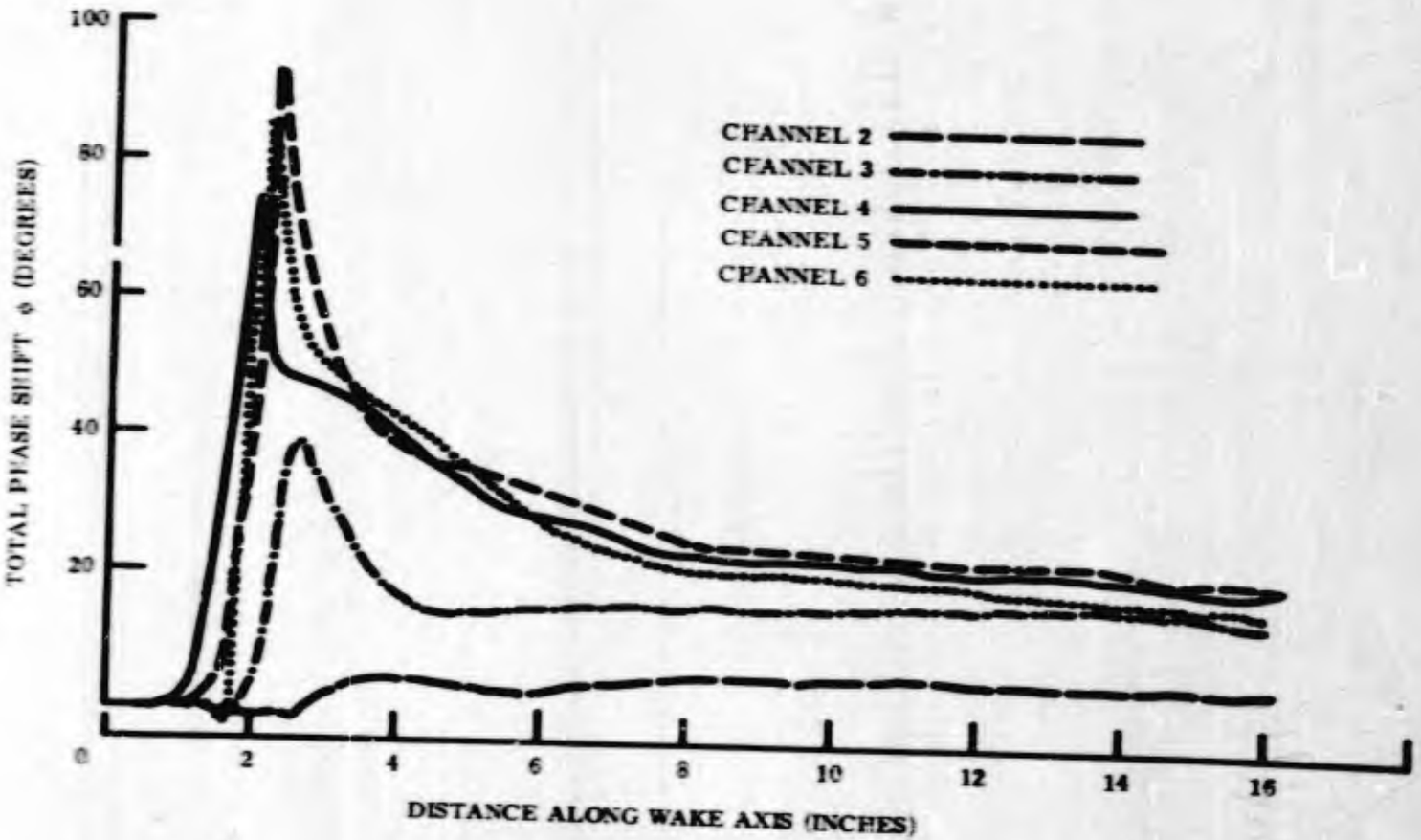

Fig. 11-31b Typical Result 70-Gc/s, Seven-Channel Phase-and-Amplitude System

REFERENCES

1. S. Silver,
Microwave Antenna Theory and Design,
Vol. 12, Radiation Labs. Series.
McGraw-Hill, 1951

2. R. L. Primich and F. H. Northover,
Defense Research Telecommunications Establishment,
Use of Focused Antenna for Ionized Trail Measurements,
Rpt. No. 1076,
October 1961,
DRTE, Shirley Bay, Ottawa, Canada

3. M. Bron and E. Wolf,
Principles of Optics,
Pergamon Press, 1959,
p. 434

4. P. A. Matthews and A. L. Cullen,
"A Study of the Field Distribution at an Axial Focus of a Square Microwave Lens",
Proc. I. E. E., London, Pt. C, Vol. 103,
Sept 1956, p. 449

5. H. M. Musal, Jr., GM Defense Research Labs.,
Plasma Frequency and Electron Collision Frequency Charts for Hypersonic Vehicle Equilibrium Flow Fields in Air,
TR62-209C,
Santa Barbara, California, Dec 1962

6. F. H. Northover and R. L. Primich, GM Defense Research Labs.,
The Incidence of Focused Microwaves upon Ionized Distributions
Part I, Plane Distributions,
TR62-209N,
Santa Barbara, California, Dec 1962

7. F. H. Northover and R. L. Primich, GM Defense Research Labs.,
The Incidence of Focused Microwaves upon Ionized Distributions
Part II, Cylindrical Distributions,
TR62-209O,
Santa Barbara, California Dec 1962

8. R. Primich, C. F. Hansen, and A. C. Charters,
"Measurements of Reentry Radar Characteristics in Free-Flight Range",
12th AMRAC Meeting,
Santa Barbara, California, Nov 1961

9. E. W. Herold,
"The Operation of Frequency Converters and Mixers for Superheterodyne Reception",
Proc. IRE,
Feb 1942

10. P. E. Robillard and W. E. Blore,
Defense Research Telecommunications Establishment,
A Target Simulator for a 35-Gc CW Doppler Radar,
Report No. 1089, Sep 1962,
DRTE, Shirley Bay, Ottawa, Canada

11. R. A. Hayami and R. I. Primich, GM Defense Research Labs.,
Ionization in Hypersonic Wakes No. 1,
Santa Barbara, California, Dec 1962

12. R. W. Landee, D. C. Davis, A. P. Albrecht,
Electronic Designer's Handbook,
McGraw-Hill, 1957

SECTION XII
CW DOPPLER RADARS TO MEASURE THE RADAR CROSS SECTION OF HYPERSONIC MODELS

INTRODUCTION

The flow field produced by a hypersonic vehicle during reentry is known to produce a heavily ionized sheath around the vehicle. Laboratory experiments have shown that ionized gases or plasmas interact with electromagnetic waves and, as a result, electromagnetic waves are used as a means of plasma diagnostics. A plasma sheath can behave either as a reflector or as a lossy dielectric, depending on the electron density, the electron collision frequency, and the operating frequency. The present interest in the interaction of reentry plasma with electromagnetic waves lies in its effect on communications and radar detection. The equipment described in this report has been developed to investigate the plasma properties at the nose region of hypersonic projectiles. From the results obtained by this controlled experiment, conditions which could affect radar detection of a reentry body can be determined.

General Motors Defense Research Laboratories operates a free-flight range facility capable of launching model projectiles into a controlled atmosphere. This facility is instrumented to investigate many aspects of the flow field and plasma created by hypersonic bodies. Models up to 20 mm in diameter are launched by a light-gas gun into the instrumented chamber where atmospheric pressures can be adjusted from sea level up to 300,000 ft (0.01 mm Hg).

To date, two CW doppler radars, operating at 35 Gc/s at 70 Gc/s, have been used to study the effect of the plasma sheath on the radar cross section of hypersonic projectiles. The selection of these frequencies was governed by the high electron concentrations expected in the nose or stagnation region of the projectiles. The initial experiments were designed so that the radar frequency would be in the vicinity of the equilibrium, stagnation, plasma frequency. At 35 Gc/s and 70 Gc/s, the plasma frequency is equal to the radar frequency at an electron concentration of $1.52 \times 10^{+13}$ e/cc and $6.1 \times 10^{+13}$ e/cc, respectively. The above electron concentrations are produced at the stagnation region of blunt models at velocities of approximately 14,000 – 15,000 ft/sec in an atmospheric pressure of 10 mm Hg, assuming equilibrium conditions. Since reentry velocities often exceed the above figure, the need for a higher radar frequency is obvious. However, at the time of development of the described systems, millimeter wave sources above 70 Gc/s were not readily available. Present plans are to develop identical systems at 140 Gc/s (and higher) as components and microwave sources become available.

The two doppler radar systems were designed to measure the absolute radar cross section of projectiles at velocities ranging from 2,000 – 30,000 ft/sec. As a result of the calibration procedure which will be described in this report, absolute radar cross sections from 1×10^{-1} square wavelengths to 1×10^{3} square wavelengths can be measured with an accuracy of ±1 db. The radar cross section of a model measured in flight is then compared to the radar cross section of the same model measured in a static radar cross section range to obtain the change in radar cross section. This change has been attributed to the

plasma sheath. A number of firings have been observed with both radars, and results of radar cross section as a function of velocity at constant atmosphere pressures have been obtained. These results and their interpretation are discussed elsewhere.

INSTALLATION OF RADARS ON PHYSICS RANGE

The installation of the 35-Gc/s and the 70-Gc/s radars is shown in Fig. 12-1. The range consists of a cylindrical tank approximately 100 ft long. The first 50 ft of the range, 2 ft in diameter, contains instrumentation consisting of velocity measuring stations, radiation detectors and focused microwave probes. The last 50 ft of the range, 8 ft in diameter, is used only for the doppler radar studies.

As shown in Fig. 12-1, the two doppler radars are installed at the impact end of the range. The 35-Gc/s radar is mounted on one side of the range with its radar antenna aligned to illuminate a radar reflector placed on the axis and oriented at 45° with the flight axis. The signal from the antenna is fed into the radar chamber through a 2-in.-thick, matched dielectric window* and reflected off the radar reflector along the flight axis. The signal scattered back by the model returns to the radar antenna along this same path. The radar reflector consists of a 2-ft square of thin aluminum sheeting mounted on a rigid reflector support. The reflector sheet is impacted by the projectile and is replaced after each firing. A study of the perforation of the reflector sheet by the model can reveal not only the condition of the model at impact but the coordinates of the impact point as well.

*Polypenco 1402

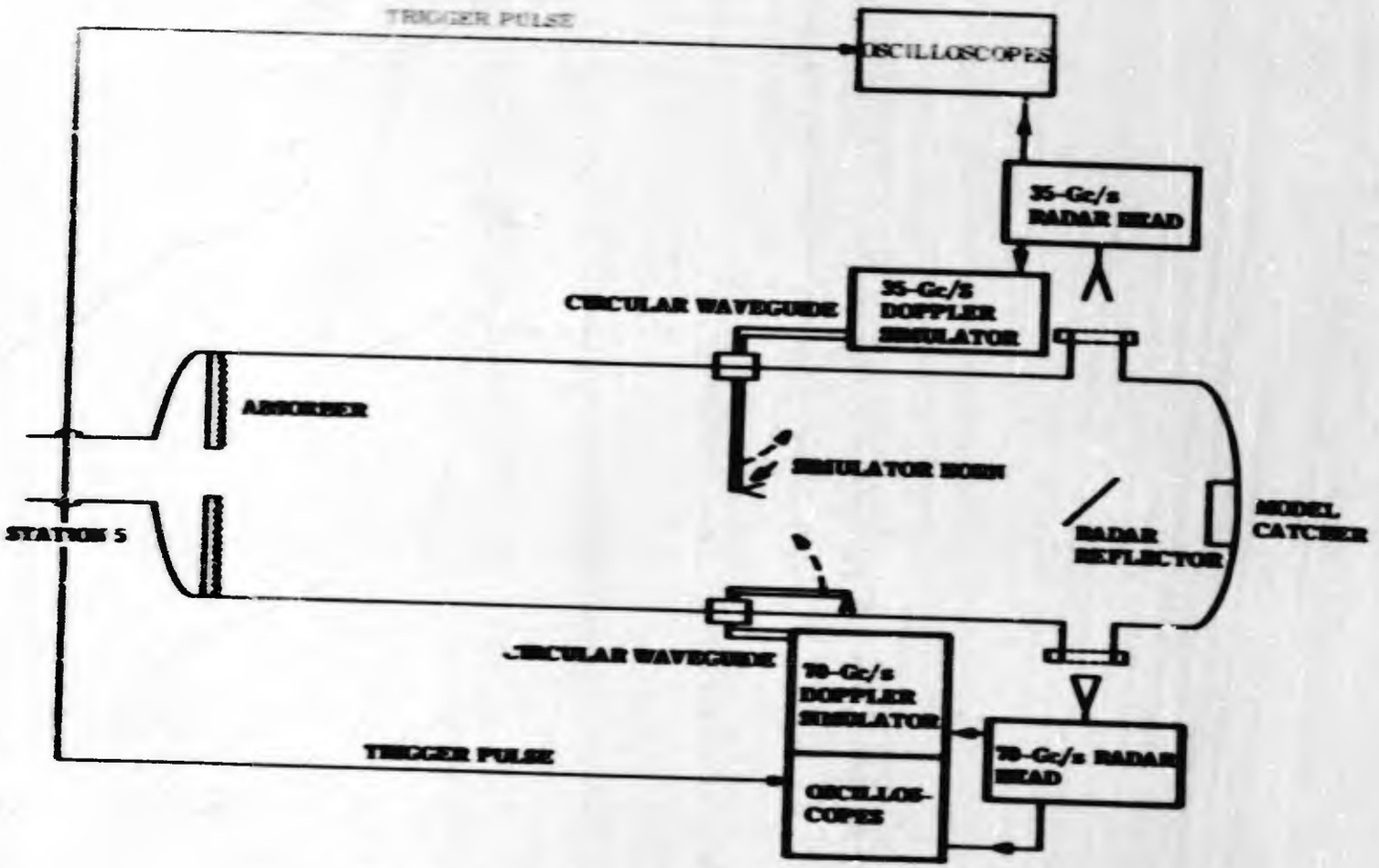

Fig. 12-1 Radar Installation, Physics Range

Since the equipment is used to determine the absolute radar cross section of projectiles, calibration of the radar system prior to each firing is necessary. This is accomplished by transmitting a simulated doppler signal toward the radar from a horn positioned on the flight axis 19 ft from the radar reflector. The simulator horn is mounted on a boom which is swung away from the flight axis after the calibration is complete. A more complete description of the doppler signal simulator will be given later in this report.

Because multiple operation of several radars under the above conditions has not yet been achieved, the 70-Gc/s doppler radar has been mounted on the side of the radar range directly opposite the 35-Gc/s radar. Changeover from 35-Gc/s to 70-Gc/s doppler radar operation includes a 90° counterclockwise rotation of the radar reflector. The 70-Gc/s doppler radar also has a signal simulator horn located uprange for calibration purposes.

In both radar systems, the signal received from the projectile is displayed on oscilloscopes that are operated in a transient recording mode, and then recorded on Polaroid film. It is advantageous to record the signal from the projectile from the time it enters the 8-ft section of the range until it impacts the radar reflector. To accomplish this, the oscilloscopes are triggered from a velocity-measuring station located at the end of the 2-ft diameter section of the range. By setting the oscilloscope sweeps to endure longer than the flight, a record of the signal for the complete flight path can be obtained.

To facilitate the analysis of the received signal, another trigger has been added to the system. This trigger is a microwave located the same distance from the reflector as the signal simulator horns. The

projectile interrupts the narrow microwave beam to provide the pulse that triggers an additional oscilloscope. The need for this trigger at the calibration distance is indicated in the analysis of a typical doppler result at the end of this report.

THE DOPPLER RADAR TECHNIQUE

Since the experiments involve a moving target, the doppler radar technique was the obvious choice. Such a system is sensitive only to moving targets and remains unaffected by signals reflected from stationary surfaces; the signals reflected from the metallic range walls do not appear as output signals. Although the doppler frequency shift can be used to obtain velocity information, this is not of direct interest in this experiment because accurate velocity measurements are made with optical velocity-measuring stations. The amplitude of the doppler signal is a function of the power which is back-scattered by the moving target.

The doppler frequency shift f_d produced by a moving target is approximately

$$f_d = \frac{2 f_c V}{C}$$

where f_c is the radar frequency, V is the velocity of the target, and C is the velocity of light. At 35 Gc/s, the doppler frequency shift is 71 kc per 1,000 ft/sec of target velocity. Since the receiver has a flat frequency response from 300 kc – 3 Mc, the radar can be used to observe targets with velocities ranging from 4,000 – 40,000 ft/sec. At 70 kmc, the doppler shift is 142 kc per 1,000 ft/sec of model velocity; therefore, with a receiver frequency response of 500 kc – 4 Mc, this system can be used to observe projectiles with velocities of 300 – 28,000 ft/sec.

In the initial experiments, an abnormally high noise level was noticed at the radar receiver. This noise, which seemed to develop from vibrations at the end of the 8-ft section of the range, was overcome by lining the end of the range with microwave absorber*. A hole approximately 8 in. square and centered on the flight axis was cut in the absorber to permit the projectile to enter the radar range.

THE CW DOPPLER RADAR ANTENNA

Both the 35-Gc/s and 70-Gc/s doppler radars have been fitted with a conical horn antenna, each with an aperture of 20 wavelengths in diameter. A matched lens correction has been provided in each aperture for the purpose of maximizing the gain.

The antenna's design resulted from a compromise between gain (of the antenna), or beam width, and the extent of the near field in which the field distribution over the model's flight path would not be uniform.

The gains of these 20λ antennas have been measured to be 34.8 db above an isotropic source. The H-and E-plane half-power beam widths for these antennas are 3.5° and 3.0°, respectively, and the H-and-E plane patterns are shown in Figs. 12-2a and 12-2b, respectively. With the radar antenna located 50 ft from the end of the range, the beam width in the H-plane is 3.1 ft. In the E-plane, the beam width at 50 ft is only 2.6 ft. From these calculations it is obvious that if multipath propagation is present, it will be very small. The angle at which the signal starts illuminating the side of the range is 4.6°, which is at the first null of the E-plane pattern of the antenna. Therefore, the

*B.F. Goodrich VHP-2

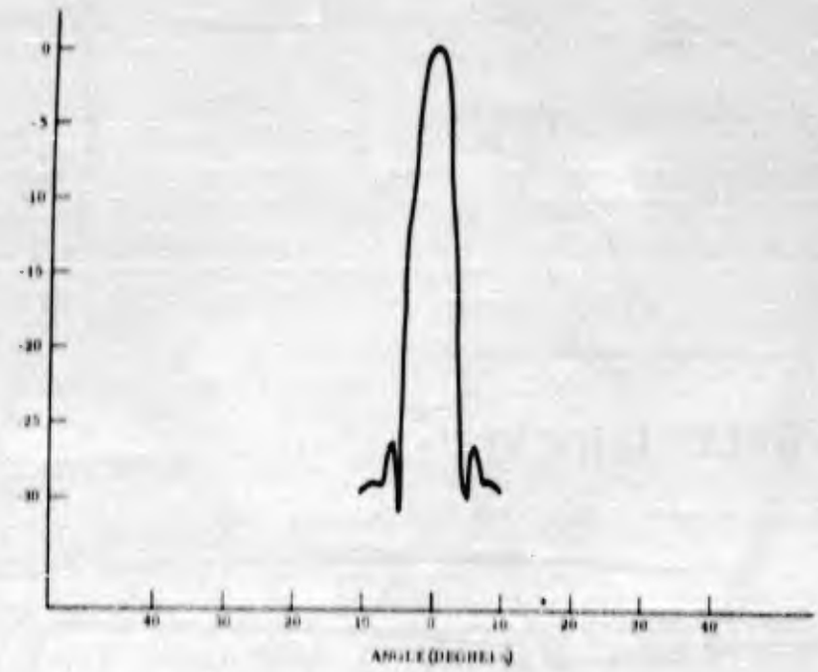

Fig. 12-2a H-Plane Antenna Pattern

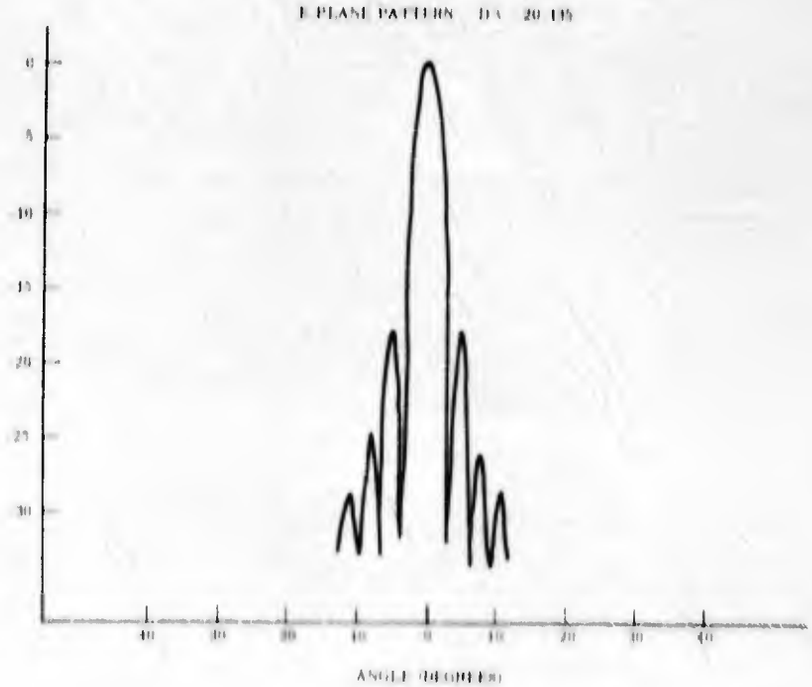

Fig. 12-2b E-Plane Antenna Pattern

first sidelobe of the antenna does reflect off the range wall. Since it is 30 db down on a two-way path, its effect could produce a small amount of interference, and such interference has been recorded. However, it is very small and disappears as the projectile approaches the radar.

The other factor which was taken into consideration in the antenna design was the near-field illumination of the target. It is important that a uniform field distribution be maintained across the target surface as it approaches the antenna. The criteria used for the uniform field distribution is that the power distribution across the target be within 1 db and the phase distribution be within $1/16\,\lambda$. For a target of the same dimension as the antenna, this distance is $\frac{2d^2}{\lambda}$, d being the antenna diameter. Since in this particular experiment the target is much smaller than the antenna, the distance was taken as $\frac{d^2}{\lambda}$ which is approximately 6 ft at 70 Gc/s and 11 ft at 35 Gc/s. With the radar antenna situated 5 ft from the reflector, the near field extends 6 ft uprange from the radar reflector at 35 Gc/s; therefore the radar cross section must be measured beyond this point to be considered accurate. This calculation assumes that the projectile is positioned directly on the center of the antenna beam. If the projectile is off-course, the minimum distance where uniform field distribution across the model occurs will be farther from the antenna.

With the model in the far field of the radar antenna, the signal received by the radar will increase as a function of the inverse of the fourth power of the model range ($\frac{1}{R^4}$), according to the radar equation in Section 7. As the model enters the near field of the antenna, a departure from this $\frac{1}{R^4}$ law can be expected due to the varying antenna gain in this region.

THE 35-Gc/s CW DOPPLER RADAR

The 35-Gc/s CW doppler radar has been designed to measure the absolute radar cross section of projectiles ranging in velocities from 3,000 – 30,000 ft/sec. The system sensitivity is such that absolute radar cross sections ranging from $1 \times 10^{-1} \lambda^2$ to $1 \times 10^{3} \lambda^2$ can be measured with an adequate signal-to-noise ratio over a distance 12 – 30 ft from the radar antenna.

A photograph of the 35-Gc/s doppler radar is shown in Fig. 12-3. The installation of the microwave head on a camera tripod, the matched dielectric window, the doppler signal simulator, and the oscilloscopes with cameras can all be seen.

Radar Alignment

To assure uniform illumination of the projectile by the antenna beam, especially when the projectile approaches the near field of the antenna, precision alignment of the radar antenna and reflector is necessary. To obtain the accuracy required, it is necessary to align the radar antenna and radar reflector with the axis of the gun barrel. The transit used to align the gun barrel was also used to align the radar system. To align the radar system, the aluminum reflector was replaced by a mirror, the dielectric window was removed, and the antenna lens was replaced by a set of orthogonal cross hairs. With a point light source at the throat of the horn, the reflector and antenna were aligned by sighting the light source from the transit. The radar tripod was then bolted to the floor to maintain the alignment. The radar reflector is of very rigid construction to assure stability at

Fig. 12-3 35-Gc/s CW Doppler Radar

projectile impact. When realignment is necessary, the reflector mount (which has both azimuth and elevation control) is adjusted for maximum-received signal transmitted from the simulator antenna (also surveyed on the flight axis).

The 35-Gc/s Microwave Head

The 35-Gc/s CW doppler radar is a monostatic radar which uses a common antenna for transmission and reception. Autodyne mixing is used in the receiver and is achieved by coupling some of the output power from the transmitter to serve as local oscillator RF bias at the receiver mixer crystals. By mixing the received signal with the local oscillator signal, the doppler frequency shift is recovered as a video signal.

A detailed block diagram of the 35-Gc/s CW doppler radar microwave head is shown in Fig. 12-4. The transmitter source is a reflex klystron set to oscillate at 35 Gc/s with a power output of approximately 100 milliwatts. A 10-db directional coupler at the output of the klystron is used to obtain both the required local oscillator bias power and a reference signal for phase-locking the klystron in the doppler signal simulator. The klystron output is then fed through an isolator and a sidewall short slot hybrid to the antenna where it is transmitted. A 10-db coupler in the antenna arm is used to measure the power transmitted at this point. Power measurements are made with a thermistor mount and a power meter. At the coupler output a waveguide switches the signal from the thermistor mount to a matched termination during radar operation.

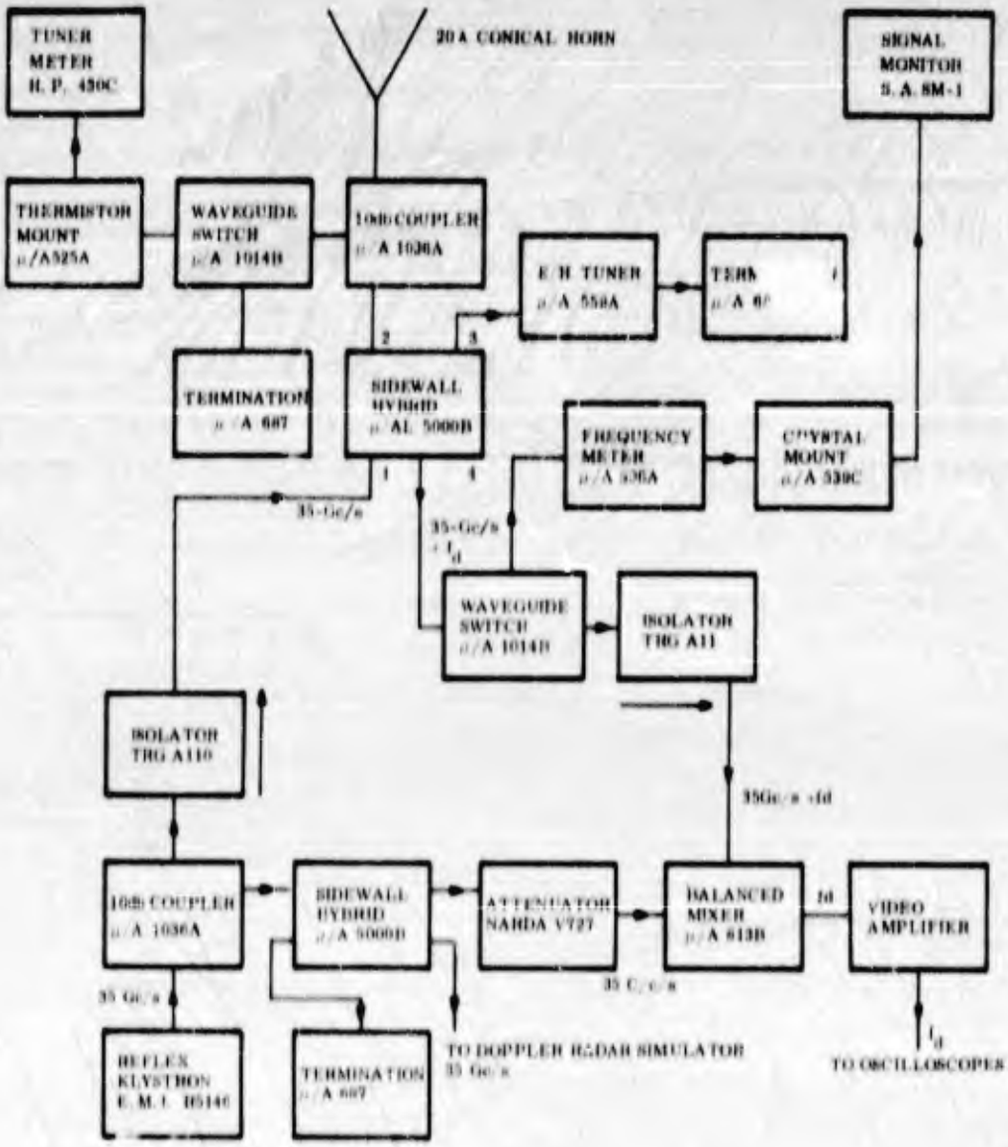

Fig. 12-4 35-Gc/s CW Doppler Radar Microwave Head

The separation between the transmitted and received signal is obtained in the sidewall short slot hybrid. The power from the transmitter klystron is divided equally into arms 2 and 3 of the hybrid, and the power received is divided equally into arms 1 and 4. Reflections of the same frequency as the transmitted frequency from the antenna and radar chamber are cancelled by tuning on arm 3, necessary because the reflections from the radar chamber could be sufficient to increase the bias on the receiver mixer crystals and increase the crystal noise. Furthermore, if the background signal is comparable to the local oscillator (LO) signal, phase interference would produce large variations in the mixer performance. A waveguide switch in the receiver arm of the hybrid is used to switch the background signal to a crystal detector where it is monitoring during background signal suppression. It is known that the transmitter and background leakage can be reduced to less than 1 microwatt.

With the waveguide switch in the receiver arm on receive position, the received signal is mixed with the LO signal in the balanced mixer, and the doppler frequency shift is recovered. An attenuator in the LO arm is set for maximum mixer conversion efficiency and minimum mixer crystal noise.

The Video Amplifier

In designing the video amplifier the following characteristics had to be maintained:

1. A wide dynamic range because the radar is used to observe an approaching target
2. Low input noise

3. A bandwidth adequate to handle the range of doppler frequencies expected. Because of the 1/f noise characteristics of mixer crystals, the low-frequency cutoff of the amplifier should be as high as possible.

The video amplifier input has been designed to match the impedance of the mixer crystals — 300 ohms. Since a single input is provided on the amplifier, a reversed pair of 1N53C crystals is used in the balanced mixer. The amplifier is mounted on the microwave head close to the balanced mixer.

A circuit diagram of the video amplifier is shown in Fig. 12-5. The unit is completely transistorized to avoid microphonic problems present when using tubes. The frequency response of the amplifier is flat within ±0.5 db from 300 kc – 3.0 Mc. Since the doppler frequency shift of 35 Gc/s is 71-kc per thousand feet per second of flight, this amplifier can be used to observe projectiles with velocities ranging from 4,000 — 40,000 ft/sec. The amplifier gain is 35 db and will provide a signal of 10 — 640mv peak-to-peak over this frequency range, resulting in a dynamic range of 36 db. Since the output impedance of the amplifier is 50 ohms, the output signal can be fed to the recording oscilloscopes over long lengths of 50-ohm coaxial cable.

THE 35-Gc/s DOPPLER SIGNAL SIMULATOR

The 35-Gc/s doppler signal simulator has been designed to calibrate the 35-Gc/s doppler radar. Calibration is necessary because absolute radar cross section measurements are being made.

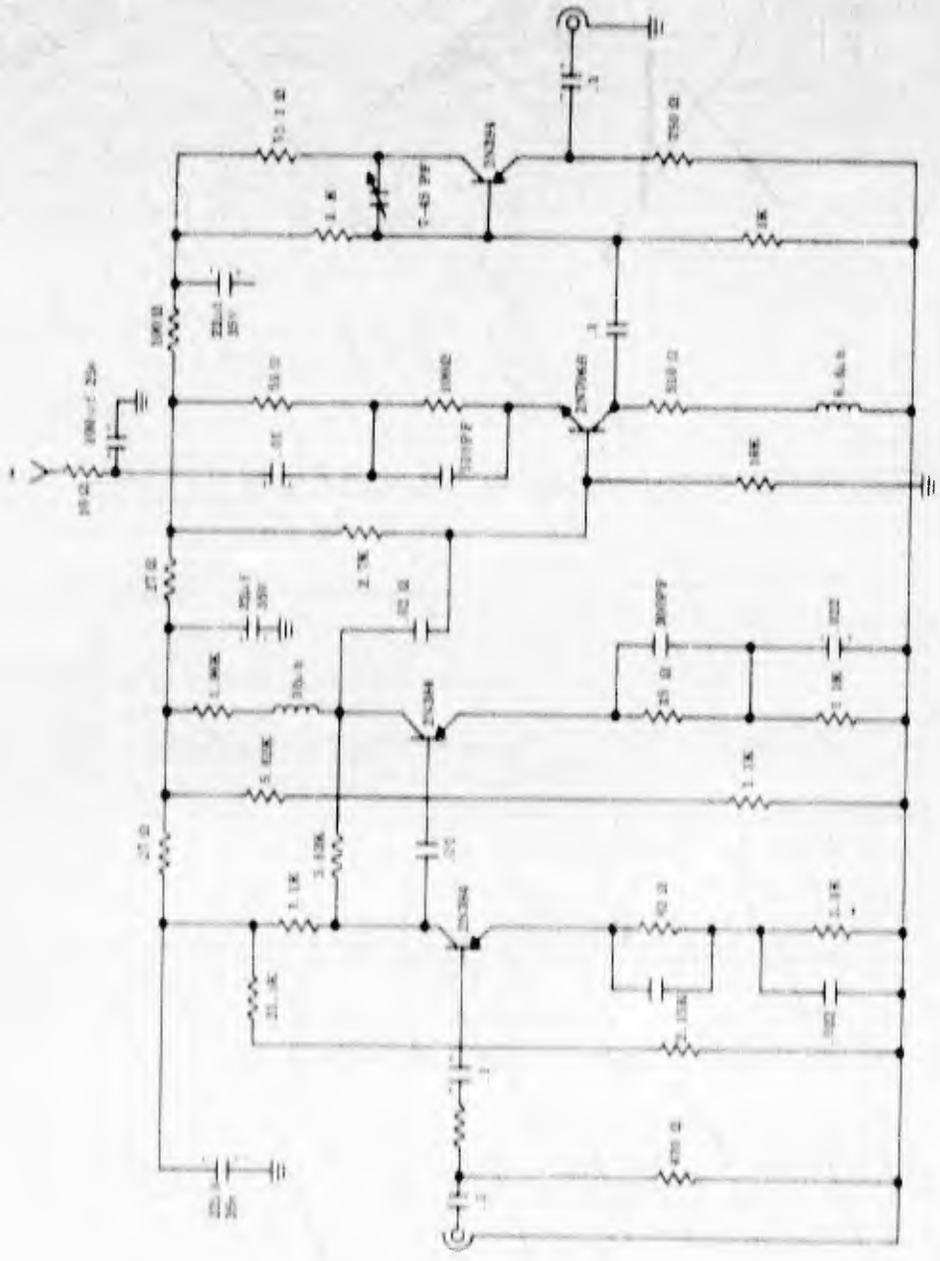

Fig. 12-5 Video Amplifier

The reflex klystron in the simulator is phase-locked to the 35-Gc/s transmitter frequency at a variable offset frequency. By setting the offset frequency equal to the expected doppler frequency, and by varying the output of the simulator to obtain a simulated power vs radar voltage output curve, a complete calibration of the doppler radar can be obtained. The simulator can also be used to measure the frequency response and sensitivity of the radar receiver and the conversion loss of the mixer crystals. With the simulator antenna on the flight axis of the projectile, measurements of free-space path loss can be made to check the radar reflector and antenna alignment.

A block diagram of the 35-Gc/s doppler simulator is shown in Fig. 12-6. A 35-Gc/s reference signal from the transmitter klystron is fed into a crystal modulator. With the modulator tuned to suppress the original carrier, the modulator output frequencies are 35,000 + (30 + f_d) Mc, where (30 + f_d) Mc is the modulator frequency and f_d is the doppler frequency. A bandpass filter at the output of the balanced modulator is set at the upper sideband (35,000 + (30 + f_d) Mc. Some of the power from the simulator signal source, a reflex klystron, is coupled to a balanced mixer and mixed with the upper sideband signal derived from the reference signal. With the simulator reflex klystron frequency set at (35,000 + f_d) Mc the difference frequency at the output of the balanced mixer is 30 Mc. This 30-Mc difference signal is amplified in a wideband 30-Mc locking amplifier. The output signal from the locking amplifier is fed into a 30-Mc phase detector where it is compared to a 30-Mc reference signal from a stable crystal oscillator. When the simulator reflex klystron is phase-locked to the reference signal, the output of the phase detector is a DC signal proportional to the relative phase between the 30-Mc

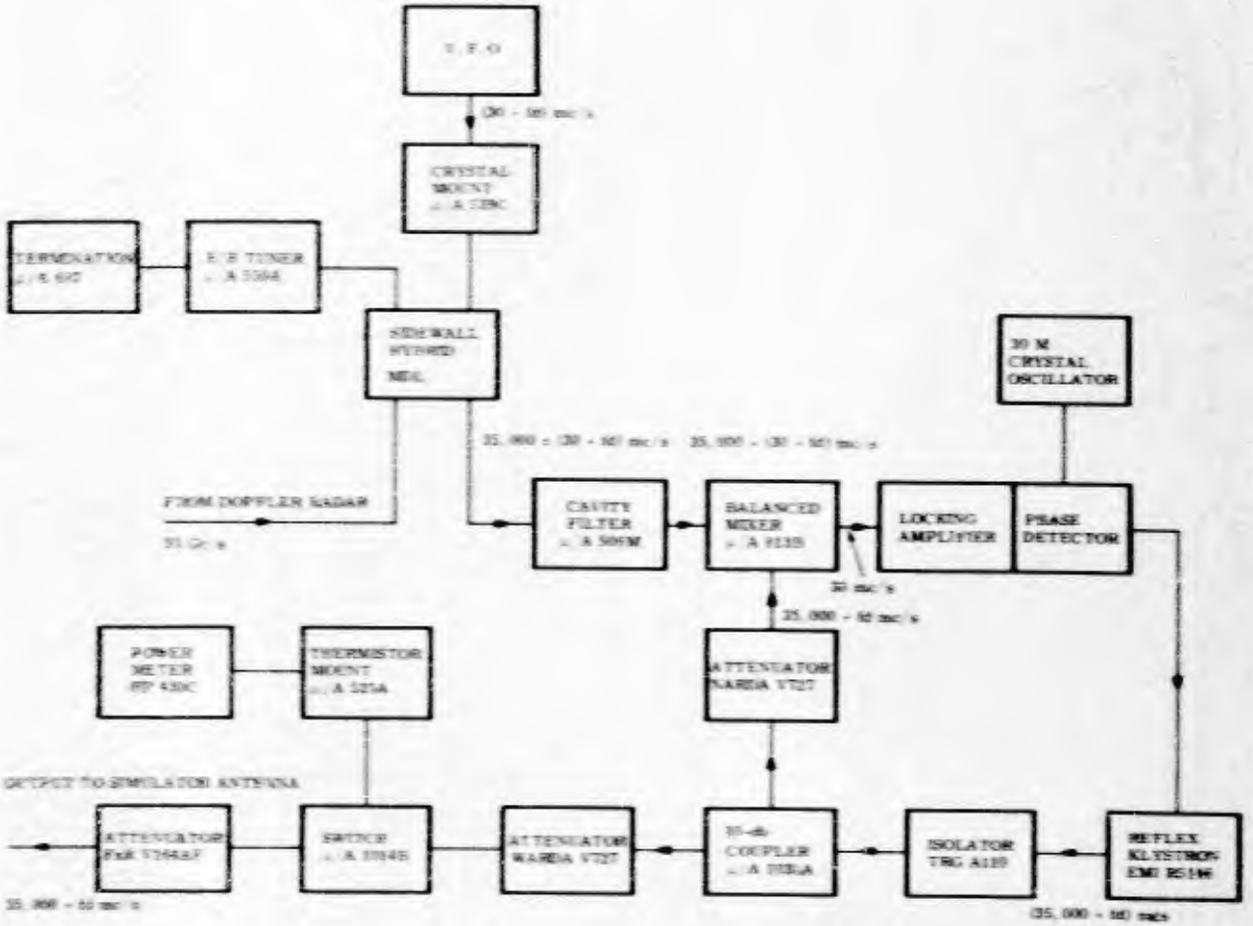

Fig. 12-6 35-Gc/s Doppler Radar Simulator

reference signal from the crystal oscillator and the 30-Mc difference frequency between the upper sideband reference signal and the klystron output signal. This DC correction signal is fed to the reflector of the reflex klystron. The simulator reflex klystron now oscillates at (35,000 + f_d) Mc, f_d Mc above the transmitted frequency. The simulated doppler frequency is set by varying the modulating frequency on the balanced modulator. The lock-in range of the phase-locking circuit is broad enough to permit variation of the simulated doppler frequency from zero to approximately 4 Mc.

The output of the simulator klystron is fed through a power-set attenuator to a waveguide switch. At this point, the power output of the simulator klystron is measured with a thermistor and can be preset to any desired level with the power-set attenuator. The simulator output is then fed to the simulator antenna. A precision attenuator at the simulator output is used for calibration of the 35-Gc/s doppler radar.

Because of the distance from the simulator output to the simulator horn, a circular waveguide is used between these two points. Propagation in this waveguide is in the low-loss TE_{01} mode.

OPERATION AND CALIBRATION OF 35-Gc/s DOPPLER RADAR

With the 35-Gc/s doppler signal simulator, the 35-Gc/s doppler radar can be calibrated both in frequency and in amplitude. The simulator can also be used to measure the path loss between the simulator antenna and the radar antenna, and to check the reflector and radar antenna alignment. Once the path loss has been determined, the sensitivity of the radar receiver can be measured.

When the simulator is transmitting towards the radar, the path loss is calculated to be

$$\frac{P_r}{P_c} = \frac{G_c G_r \lambda^2}{(4\pi)^2 R^4}$$

P_r = power received

P_c = power transmitted from the simulator

G_c = gain of the simulator antenna

λ = wavelength

R = distance between the two antennas

G = gain of radar antenna

The gains of the simulator and the radar antenna are 13.8 db and 34.8 db, respectively. The wavelength at 35-Gc/s is 0.337 in., and the distance between the two antenna is 24.4 ft (293 in.). Using the above equation, the path loss is calculated to be 32.2 db. The path loss between the two antennas has been measured to be within ±0.5 db of this figure.

Since the simulator output power is measured accurately and can be attenuated with the precision attenuator, the sensitivity of the radar receiver can be measured. This is done by attenuating the simulator output power until the received signal is attenuated into the receiver noise. This experiment has shown that with a simulator output power of -76 dbW, the signal-to-noise ratio at the receiver is unity. Taking into account the 32.2-db path loss and the 34.8-db insertion loss in the hybrid in the microwave head, the minimum detectable signal of the radar receiver is -112.0 dbW. Allowing a 10-db

signal-to-noise ratio, the minimum readable signal for radar cross section calculations is -102 dbW.

Using the above figure for a minimum detectable signal, it is possible to obtain a figure on the smallest observable target. With a monostatic radar, the signal received from a target of cross section σ at a distance D from the radar is

$$P_r = \frac{P_T G^2 \lambda^2 \sigma}{(4\pi)^3 D^4}$$

From this equation, if P_r is the minimum readable signal of -102 dbW, the minimum radar cross section that can be measured is

$$\sigma_{min} = \frac{P_{r\,min} (4\pi)^3 D^4}{P_T G^2 \lambda^2}$$

At a distance D of 10 ft, with a transmitted power P_T of 4×10^{-2} watts, the minimum radar cross section is 22.5 db below one square wavelength. Since the received signal decreases as the inverse of the fourth power of the distance, σ_{min} is 10.5 db below one square wavelength at 20 ft and 1.5 db above one square wavelength at 40 ft. The projectiles observed with this equipment have been mostly spherical nose shapes with radar cross sections of 10 db above one square wavelength or greater. The signal-to-noise ratio is adequate with these shapes for detecting any decrease in radar cross section due to the plasma.

Pre-Firing Calibration

Before radar calibration immediately preceding a firing, the radar performance must be checked out to assure accurate and consistent results.

A frequency check of the transmitter klystron is made to assure that its frequency is 35 Gc/s. To obtain maximum transmitted power and minimum receiver noise, it is important that the klystron should oscillate on the center of its reflector mode. Under optimum transmitter conditions the background leakage signal at the receiver is canceled by using the E/H tuner in the short slot hybrid.

The simulator reflex klystron is then phase-locked to the transmitter reflex klystron, and the doppler simulated frequency is adjusted to approximately the same doppler frequency shift expected from the projectile. A check on the radar alignment, with the simulator output set at a known level and noting the signal on the oscilloscopes, is now possible. In most cases, the change in signal level for the same simulated power remains within ± 1.0 db from firing to firing. To calibrate the radar, the simulator output power is preset at 1.0 mw measured with the thermistor at the simulator output. With a loss of 6.0 db in the circular waveguide path between the simulator output and the simulator antenna, the transmitted simulator power is -36.0 db W. A calibration curve of radar output voltage versus power simulated is plotted by varying the calibrated attenuator at the simulator.

The doppler signal is recorded on two dual-beam oscilloscopes. The scope sweep mode is set on single-sweep with a total sweep duration equal to or longer than the duration of flight. One scope is triggered

by a pulse from velocity Station 5 located at the end of the 2-ft section of the range. The other scope is triggered by a microwave trigger located the same distance from the reflector as the simulator antenna. To increase the effective dynamic range of the receiver, different oscilloscope amplifier gains are used on each beam of the dual-beam oscilloscopes.

THE 70-Gc/s CW DOPPLER RADAR

The 70-Gc/s CW doppler radar is located on the physics range directly opposite the 35-Gc/s CW doppler radar. Since the two systems are of the same design, it is unnecessary to describe the system thoroughly at this point. In addition, operation and calibration procedures are identical for both systems.

A photograph of the 70-Gc/s CW doppler radar system is shown in Fig. 12-7. A detailed photograph of the 70-Gc/s microwave head is shown in Fig. 12-8.

A block diagram of the 70-Gc/s radar microwave head is shown in Fig. 12-9. With the doppler frequency shift of 142.0 kc per thousand feet per second of model velocity, the high-frequency response of the video amplifier has been increased to 4.0 Mc to provide a capability of observing projectile velocities up to 28,000 ft/sec.

The sensitivity of the 70-Gc/s doppler radar receiver has been determined with the use of the 70-Gc/s doppler signal simulator. The free path loss between the simulator and radar antenna is calculated with the formula to be 38.4 db. A power output from the simulator antenna

$$\frac{P_r}{P_c} = \frac{G_c G_A^2}{(4\pi)^3 R^4}$$

$\frac{P_r}{P_c}$ = path loss

G_c = gain of simulator antenna = 13.5 db

G = gain of radar antenna = 34.8 db

λ = wavelength = 0.169 in.

R = distance = 24.1 ft

of -66.5 dbw produces unity signal-to-noise ratio at the radar receiver. Taking the 3.1-db insertion loss of the radar head, the sensitivity of the radar receiver is -108.0 dbw. Allowing a 10-db signal-to-noise ratio as a minimum acceptable ratio using the radar equation for a monostatic radar, the minimum detectable radar cross section at a distance of 10 ft from the antenna is found to be 4.75 db below one square wavelength with a transmitted power of 60 milliwatts. The minimum detectable signal decreases to 7.25 above one square wavelength at 20 ft and 19.25 above one square wavelength at 40 ft. Because of the possibility of absorption by the plasma which would result in a decrease in radar cross section, the 70-Gc/s doppler radar is suitable for observing targets with a minimum radar cross section of 10 db above one square wavelength.

THE 70-Gc/s DOPPLER SIGNAL SIMULATOR

The 70-Gc/s doppler signal simulator has been designed to calibrate the 70-Gc/s CW doppler radar. The simulator signal can also be used to investigate the performance of the radar system as indicated in the preceding section.

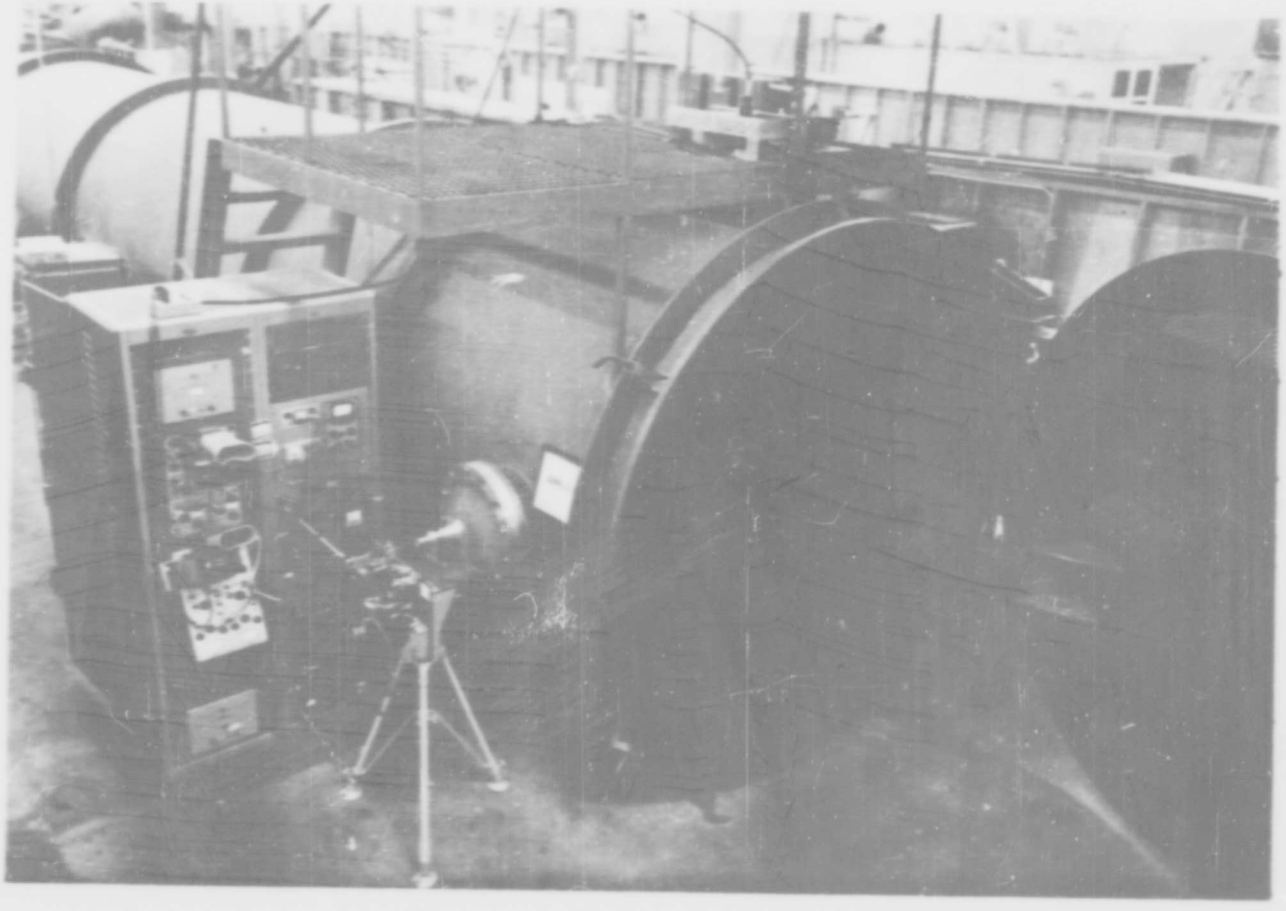

Fig. 12-7 70-Gc/s Doppler Radar System

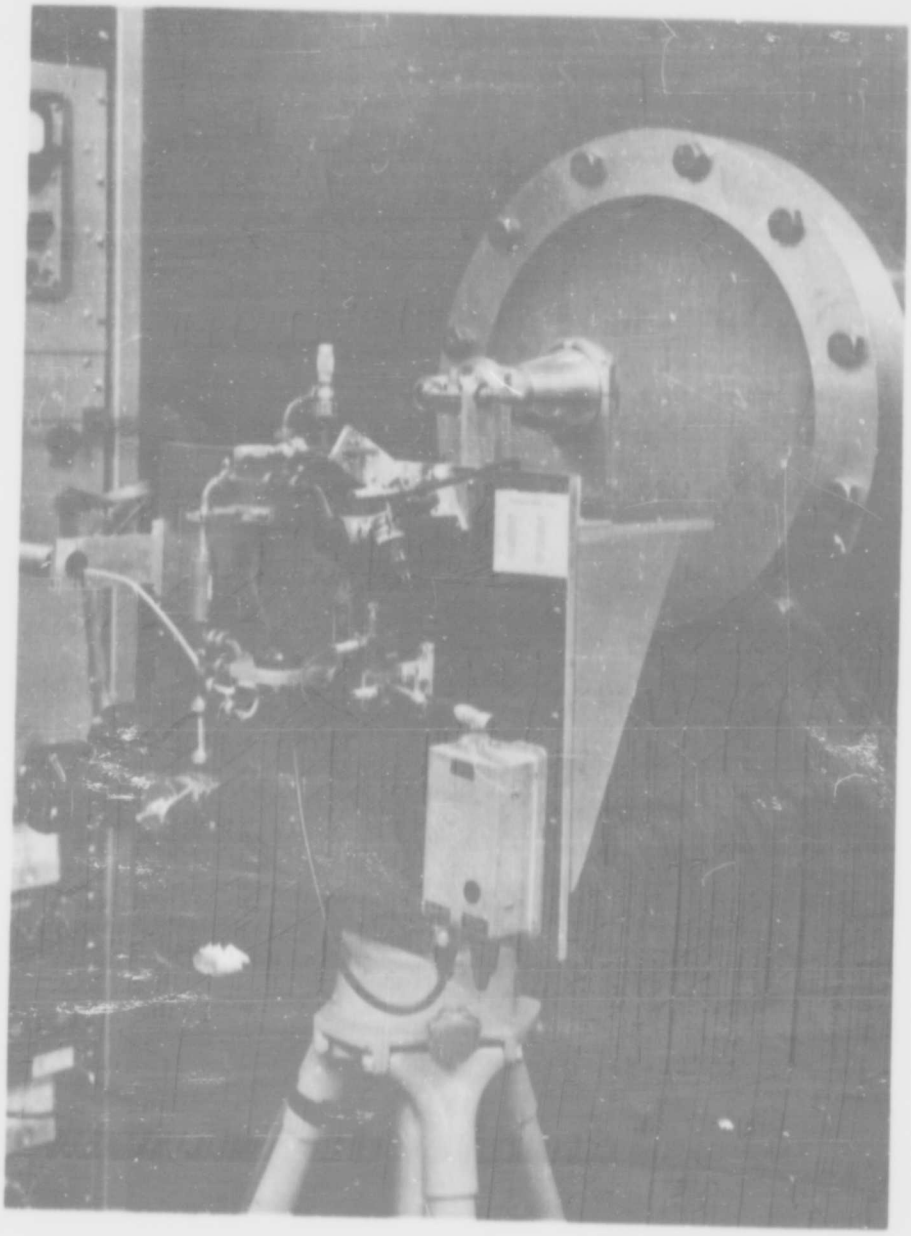

Figure 12-8 70-Gc/s Doppler Radar Microwave Head

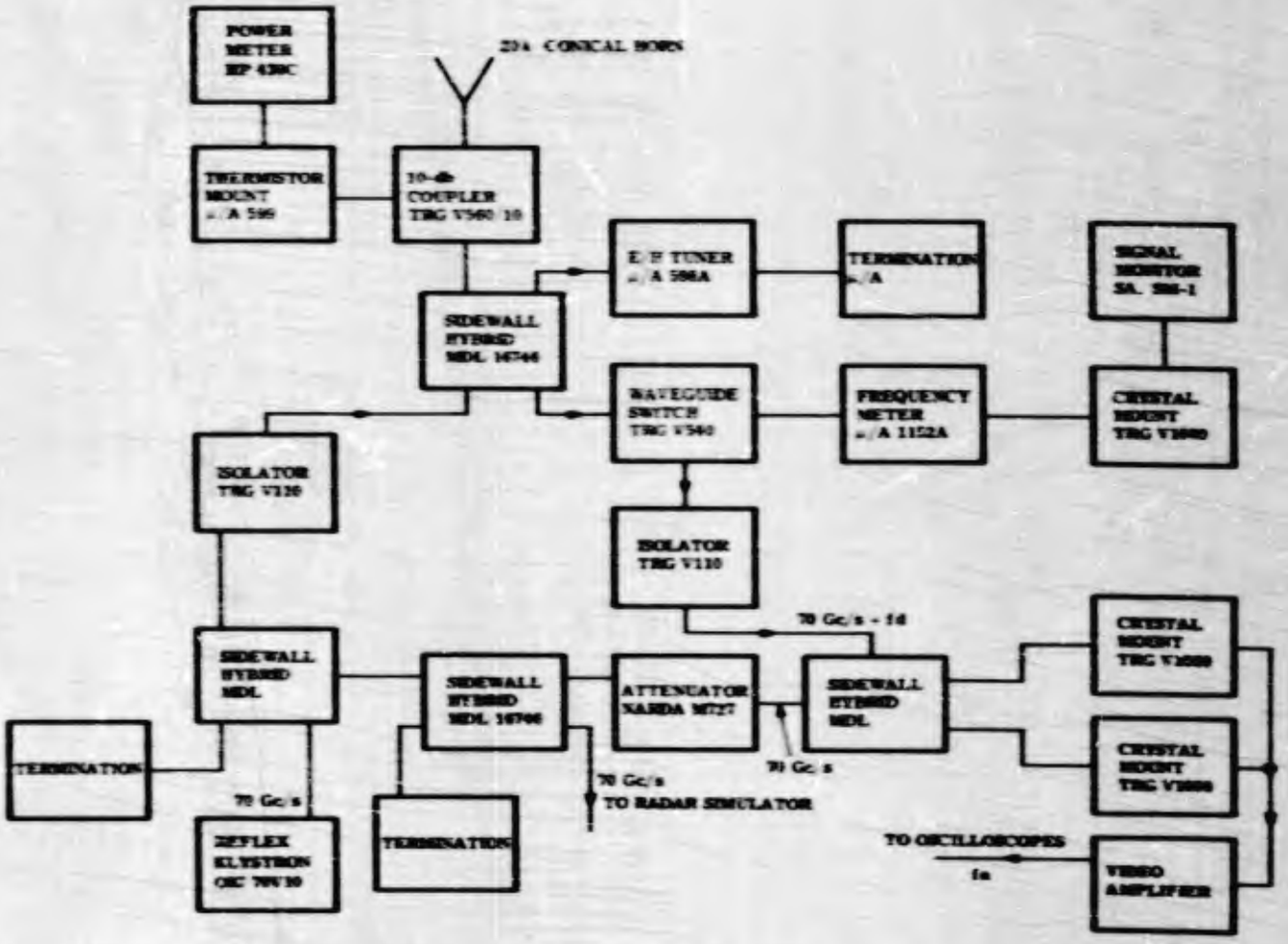

Fig. 12-9 Block Diagram of the 70-Gc/s Doppler Radar Head

A block diagram of the 70-Gc/s simulator is shown in Fig. 12-10. The balanced modulator and bandpass filter combination, as described in the 35-Gc/s doppler simulator paragraph, could not be used to produce the upper sideband at 70,000 + (30 + f_d) Mc since a suitable filter was not available. Instead, a single sideband generator has been designed for this purpose. The single sideband generator is adjusted to cancel the lower sidebands produced at the two crystal modulators. This cancellation is accomplished by shifting their relative phases so that they are in quadrature. Reduction of the lower sideband by 20 db is adequate for this application. The operation of the 70-Gc/s and 35-Gc/s doppler signal simulator is similar. The topic has been covered thoroughly in previous sections.

ANALYSIS OF A TYPICAL RESULT

The object of the 35-Gc/s and 70-Gc/s CW doppler radar systems is the measurement of the absolute radar cross section of a projectile shielded by a plasma sheath. The radar cross section of a model measured in flight is compared to the radar cross section of the same model measured in a static radar range and the change in radar cross section is attributed to the plasma sheath.

The accuracy of the experiment is attributed to the doppler signal simulator which is used to calibrate the doppler radar system over a wide dynamic range at the expected doppler frequency. During calibration, the power received by the doppler radar is equal to

$$P_r = \frac{P_s G_s G \lambda^2}{(4\pi)^2 R^2}$$

P_r = power received at radar

P_s = simulator output power

G_s = gain of simulator antenna

G = gain of radar antenna

R = distance between the two antennas

λ = radar wavelength

The calibration process consists of varying the simulated power P_s over a wide range to obtain a plot of receiver voltage output as a function of simulator power.

The data from round 148, a typical result, is shown in Fig. 12-11. Figure 12-12 shows the pre-firing calibration curve of the radar system. These results were obtained with the 70-Gc/s doppler radar. The upper photograph (Fig. 12-11) depicts the signal backscattered from a sphere as it approaches the radar. The top beam is triggered from the microwave trigger located 19.1 ft uprange from the radar reflector. The duration of the top sweep was set to last longer than the duration of model flight from the trigger position to the radar reflector. In this particular case, the reflector impact occurred 1.64 millisecs after the trigger pulse. As the projectile approaches the radar, the signal received at the radar increases inversely as the fourth power of the projectile distance. Assuming a linear sweep and a constant velocity, the distance of the projectile on the photograph can be located.

In the lower beam, the doppler signal is displayed on a faster time base to obtain a sample of the fine structure of the doppler signal. The sweep start for the bottom trace is delayed from the sweep start

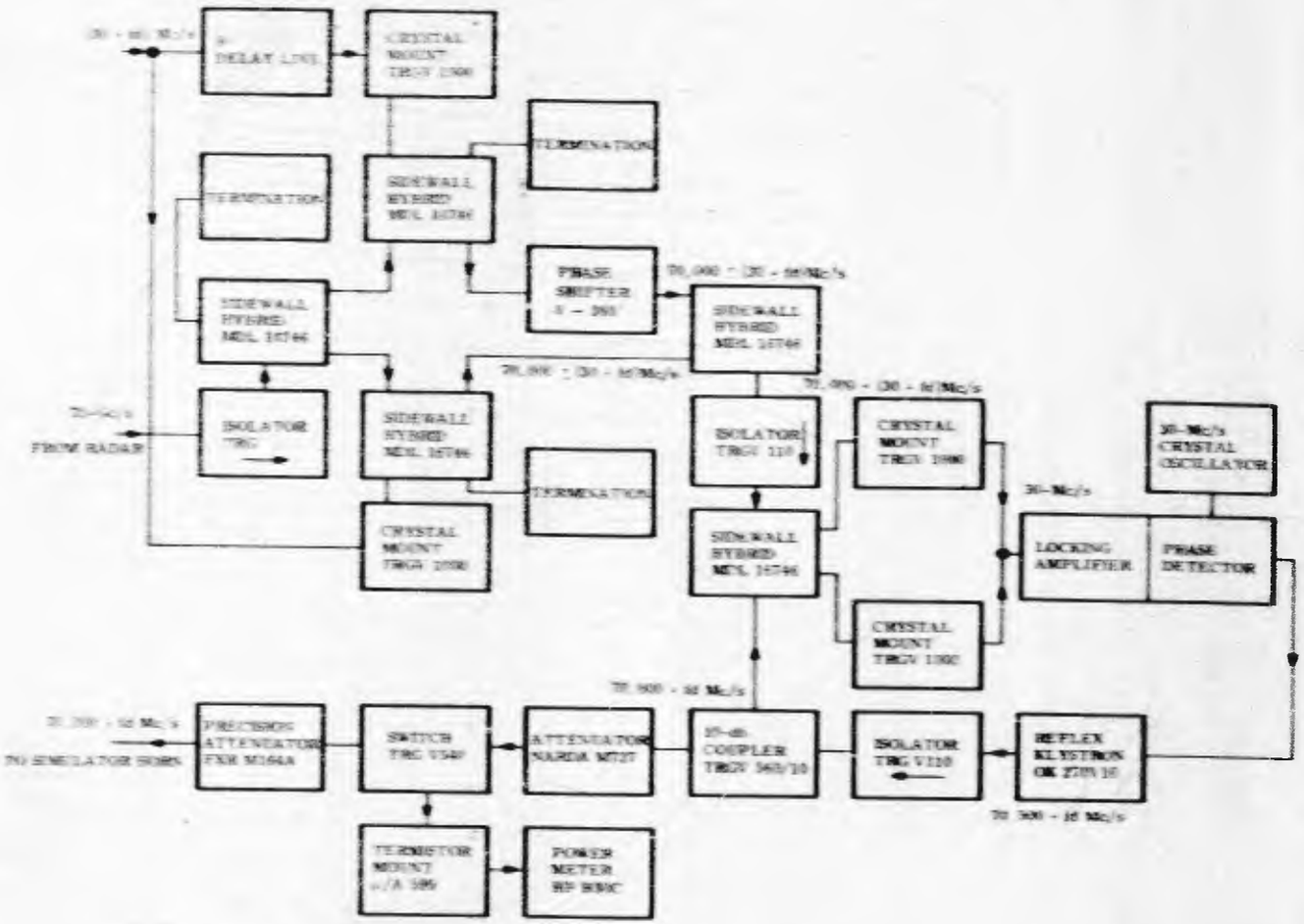

Fig. 12-10 Block Diagram of The 70-Gc/s Doppler Radar Simulator

ROUND # B-148

V_o = 11,400 ft/sec

V_2 = 11,350 ft/sec

I, I_s = (1 1/4)(-3/4)

I_c = ( )( )

P_R = 4.2 milliwatt

P = mm Hg

R = (Roll)

MODEL: Shape - Sphere
Size - 0.590
Material - Zelux/C.P.

Date: Oct. 19, 1962
70-Gc/s Data

CHANNEL NO. 1

X_A = 0.2 μsec/cm

Y_A = 20 millivolts/cm

X_B = 1.0 μsec/cm

Y_B = 20 millivolts/cm

Trigger = Microwave

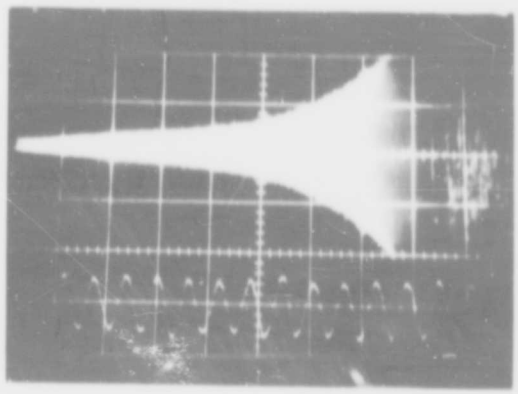

CHANNEL NO. 2

X_A = 0.5 μsec/cm

Y_A = 20 millivolts/cm

X_B = 0.5 μsec/cm

Y_B = 10 millivolts/cm

Trigger = Station 5

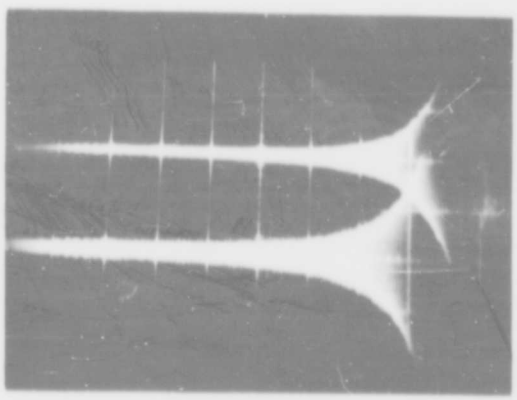

Fig. 12-11 Typical Result of Doppler Radar Measurement

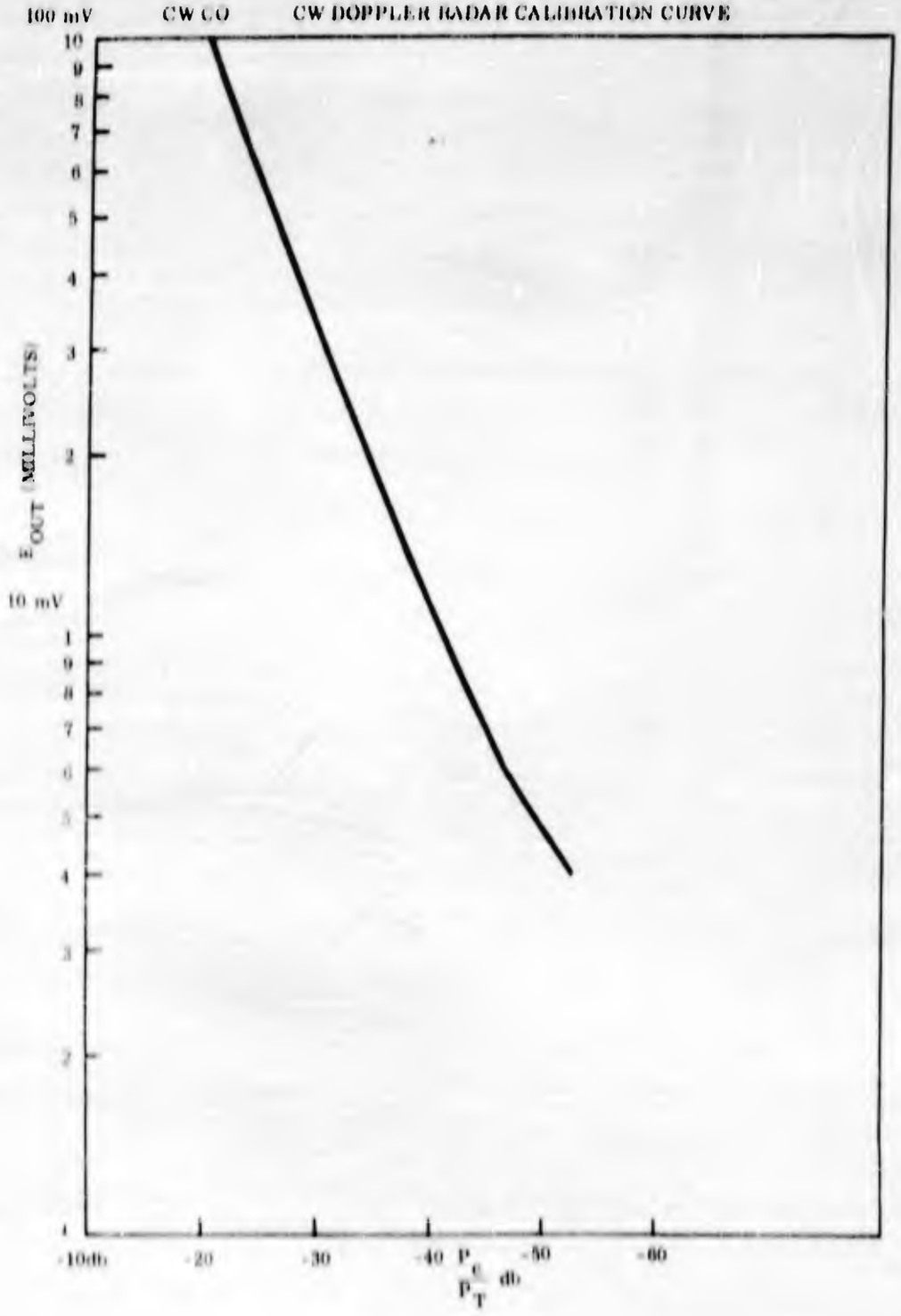

Fig. 12-12 CW Doppler Radar Calibration

of the top trace by 1.0 millisecs as shown by the brightened vertical line in the top trace.

Both sweeps in the lower photograph are triggered from velocity Station 5, located 51.1 ft uprange. The duration of model flight for this distance is 4.5 millisecs. Two oscilloscope amplifier gains are used to increase the dynamic range of the display system.

In both photographs, the erratic signal received by the radar after impact is caused by the radar reflector vibrations.

When the radar is used to observe a target at any distance D from the radar, the power received, P_r, is

$$P_r = \frac{P_T G^2 \lambda^2 \sigma}{(4\pi)^3 D^4}$$

The calibration curve is produced under the conditions given in the equation at the beginning of this paragraph. The signal that is back-scattered from the projectile and received from the radar is produced under the conditions given by the preceding equation.

To obtain a value of the radar cross section of the projectile at a distance D from the radar, E_{out} is read from the photograph at this point. This E_{out} will coincide with a value E_{out} on the calibration curve. Since both output voltages are the same, the power received at calibration and at recording are the same. It is now possible to equate the two equations in terms of Pr

$$\frac{P_s G_s G_\lambda^2}{(4\pi)^3 R^4} = \frac{P_T G^2 \lambda^2 \sigma}{(4\pi)^3 D^4}$$

and solve for the unknown radar cross section

$$\sigma = \frac{P_s G_s 4\pi D^4}{P_T G_T R^2}$$

In the above equation, $\frac{G_s 4\pi}{G_T R^2}$ is a constant, K. Since R is used as a reference distance, it is preferable to express D in terms of R. Let D equal R-d, d being the distance of the projectile from the calibration point. This can be written in simplified form

$$\sigma = \frac{P_s}{P_T} (R-d)^4 K$$

P_s is the power from the simulator determined from the calibration curve, and P_t is the power transmitted measured immediately after the firing. Therefore, σ is determined from this equation.

To date, approximately 350 firings have been observed with the CW doppler radar equipment. This large volume of results has made it necessary to use computers for data analysis.

With a data reader, a larger number of points from the photograph of voltage as a function of time can be recorded. The accuracy of the data reader (which magnifies the photograph) is definitely superior to manual scaling of the photograph. These advantages in reading have provided an accurate value of radar cross section as a function of range.

Another disadvantage of manual analysis of the results is the difficulty in obtaining a value of model range (R-d) from the photograph. This problem exists especially when the model is decelerating and the velocity during flight is not constant. From the velocity-measuring stations located in the 2-ft section of the range, the drag coefficient of the model is determined. With this information, the velocity for any model range can be calcualted. Using this information in the computer analysis, the model range on the photograph is located.

A typical output from the computer analysis is shown in Fig. 12-13. Radar cross section of the model $\frac{\sigma}{\lambda^2}$ is plotted as a function of range. The radar cross section is shown to be constant for a range of 10 – 30 ft from the radar. The decrease in radar cross section as the model approaches the radar is due to the poor near-field illumination of the model. The increase of radar cross section beyond 30 ft is a result of the low signal-to-noise ratio at extended distance. The radar cross section, as measured in the intermediate range, is considered accurate and is used in the final analysis.

Figure 12-13 also plots velocity as a function of range. The change in velocity with range is shown to be very small at the atmospheric pressure of 10 mm. Hg.

CONCLUSIONS

A 35-Gc/s and a 70-Gc/s CW doppler radar have been described. The radars were developed to measure the absolute radar cross section of model projectiles with velocities from 3,000 – 40,000 ft/sec in free flight range.

The radars have capabilities of detecting targets with a radar cross section of 10 db above one square wavelength over a range of 10 — 30 ft from the radar antenna, allowing a sufficient margin of signal-to-noise ratio for reduction of radar cross section due to the plasma sheath. As a result of the doppler signal simulators, the absolute radar cross section of a projectile is measured to ± 1.0 db. Computer analysis of the results provide a value of radar cross section as a function of range.

As a result of the heavily ionized plasma present at the stagnation region, higher frequency radars are planned. A 140-Gc/s CW doppler radar will be in operation in the near future.

The present radar systems, as described, have been adequate for observing targets with high radar cross sections. Since firings of low cross section models are planned, the sensitivity of the systems will be improved. In addition, the feasibility of diplexing the two systems for simultaneous operation is being investigated.

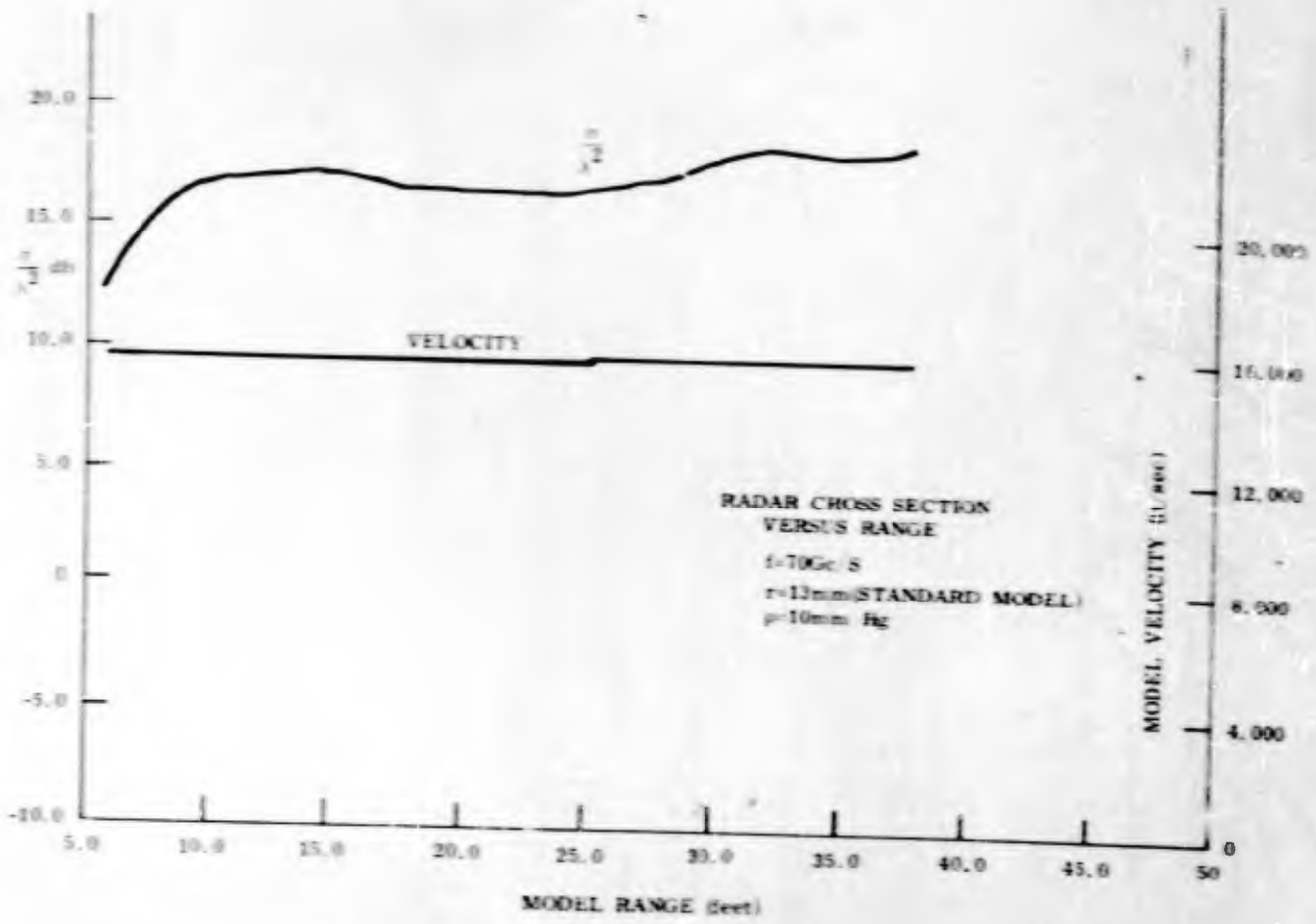

Fig. 12-13 Radar Cross Section Results

DISTRIBUTION

Recipient	Copy No.
Commander, U. S. Army Missile Command Redstone Arsenal, Alabama ATTN: ORDXM-RRX	1-12
Advanced Research Projects Agency The Pentagon Washington 25, D. C. ATTN: Lt. Col. Cooper Ballistic Missile Defense Office	13, 14
Aerojet-General Corporation Azusa, California ATTN: C. Dunning	15
Aeronutronic Division Ford Motor Company 1234 Air Way Glendale, California ATTN: Dr. John Hall	16
Aerospace Corporation P. O. Box 4007 Patrick AFB, Florida ATTN: Dr. Martin Gould Classified Documents Control	17
Aerospace Corporation Classified Information Control 2400 E. El Segundo Blvd El Segundo, California ATTN: Dr. D. Bitondo	18
Aerospace Technical Intelligence Center U. S. Air Force Wright-Patterson Air Force Base, Ohio ATTN: AFCIN-4F3B	19
Air Force Ballistic Missile Division BSRUT AF Unit Post Office Los Angeles 45, California ATTN: Major William W. Levy	20
Air Force Command and Control Dev. Div. Air Research and Development Command L. G. Hanscom Field Bedford, Massachusetts ATTN: CCO - Range Measurements Office	21
Headquarters ARDC Andrews Air Force Base Washington 25, D. C. ATTN: RDRC	22
Armed Services Tech. Infor. Agency Arlington Hall Station Arlington 12, Virginia ATTN: J. Heaton Heald	23-32
Research and Advanced Dev. Div. Avco Corporation Wilmington, Massachusetts ATTN: H. S. Flickinger Chief, Data Evaluation and Analysis	33
Avco-Everett Research Laboratory 2385 Revere Beach Parkway Everett, Massachusetts	34
Ballistics Research Laboratories Exterior Ballistics Laboratory Aberdeen, Maryland ATTN: Dr. C. Murphy	35
Barnes Engineering Company 30 Commerce Road Stamford, Connecticut	36
Batelle Memorial Institute 505 King Avenue Columbus 1, Ohio ATTN: Battelle-Defender	37
Bell Telephone Laboratories, Inc. Whippany, New Jersey ATTN: Mr. C. W. Hoover, Rm 2B-105	38
The Bendix Corporation Bendix Systems Division 3300 Plymouth Road Ann Arbor, Michigan ATTN: Systems Analysis and Mathematics Dept.	39
Commanding Officer Bureau of Naval Weapons Washington, D. C. ATTN: FASE, Dept. of the Navy	40

Recipient	Copy No.
Chief, Bureau of Naval Weapons Navy Department Washington 25, D.C. ATTN: RMWC-322	41
Brown Engineering Company Custodian, Central Security Files P.O. Drawer 917 Huntsville, Alabama ATTN: H. Crews	42
Cornell Aeronautical Laboratory, Inc. 4455 Genesee Street Buffalo 21, N.Y. ATTN: J. Lotsof W. Wurster	43, 44
Electro-Optical Systems, Inc. 125 N. Vinedo Avenue Pasadena, California ATTN: Mr. Denison	45
General Dynamics/Astronautics San Diego, California ATTN: Mr. K.G. Blair Chief Librarian Mail Zone 6-157 for W. Hooker 6-172	46
General Electric Company - MSVD Space Sciences Laboratory 3750 D Street Philadelphia, Pa. ATTN: Re-Entry Physics Library	47
Technical Information Center General Electric Company, MSVD Room 3446, 3198 Chestnut Street Philadelphia 4, Pa. ATTN: Mr. Lawrence I. Chasen Manager, Tech Info Center	48
Geophysics Corporation of America Burlington Road Bedford, Massachusetts ATTN: John W. Bond, Jr.	49
Hellodyne Corporation 2365 Westwood Blvd. Los Angeles, California	50
Jet Propulsion Laboratory 4800 Oak Grove Drive Pasadena, California ATTN: Hunston Denslow Library Supervisor	51
Applied Physics Laboratory The John Hopkins University 8621 Georgia Avenue Silver Spring, Maryland ATTN: Mr. George L. Seielstad	52
Kaman Nuclear Division Colorado Springs, Colorado ATTN: Dr. A. P. Bridges	53
Instrument Research Division Langley Research Center Langley Field, Virginia ATTN: Howard B. Edwards	54
Lincoln Laboratory, MIT P.O. Box 73 Lexington 73, Massachusetts ATTN: Library, D-224 G. Pippert	55
Lockheed Missiles and Space Division Sunnyvale, California ATTN: Ray Munson	56
Melpar Inc. Applied Science Division 11 Galen Street Watertown 72, Massachusetts ATTN: M.J. Cryer	57
The MITRE Corporation Bedford, Massachusetts ATTN: Supervisor Library Services	58
Office of the Director Technical Analysis and Advisory Group (OP-07T3E) Deputy Chief of Naval Operations (Development) The Pentagon Washington 25, D.C.	59
Chief of Naval Operations Navy Department Washington 25, D.C. ATTN: OP732	60
Chief of Ordnance Hdqt. Dept. of the Army Washington 25, D.C. ATTN: ORDTU	61

Recipient	Copy No.
RAND Corporation 1700 Main Street Santa Monica, California ATTN: Library (M. H. Davis)	62
Raytheon Company Missile Systems Division Bedford Res. and Dev. Center Bedford, Massachusetts ATTN: Mrs. I. Britton, Librarian	63
Stanford Research Institute Documents Center Menlo Park, California ATTN: Acquisitions	64
Space Technology Laboratories P.O. Box 95001 Los Angeles 45, California ATTN: Mr. L. McFadden	65
Space Technology Laboratories Titan Program Director P.O. Box 95001 Los Angeles, California ATTN: A. C. Anchordough	66
Special Projects Office Department of the Navy Washington 25, D.C. ATTN: SP-2721	67
The Radiation Laboratory Department of Electrical Eng. University of Michigan 201 E. Catherine Ann Arbor, Michigan ATTN: Dr. Richard J. Leite	68
University of Michigan Willow Run Laboratories Technical Document Service P.O. Box 2008 Ann Arbor, Michigan ATTN: Bamirac Library/B. R. George	69
Command and Control Systems Division Directorate of Systems Development Headquarters, Room 4D324 The Pentagon Washington 25, D.C. ATTN: Major R. J. Kaminski U.S. Air Force	70

Recipient	Copy No.
Commanding General U.S. Army Air Defense Command Ent Air Force Base Colorado Springs, Colorado ATTN: Advanced Projects Division	71
Commander U.S. Army Ordnance Missile Command Redstone Arsenal, Alabama ATTN: Technical Library	72
U.S. Army Liaison Office Canadian Armament Res and Dev Establishment P.O. Box 1427 Quebec, P.Q., Canada ATTN: Lt. Col. E. W. Kreischer	73
Director U.S. Naval Research Laboratory Washington 25, D.C. ATTN: Code 2027	74
Director Weapons Systems Evaluation Grp Pentagon, Room 1E800 Washington 25, D.C.	75
Defense Research Laboratories	76 and above

UNCLASSIFIED